ACS 10,417

DEVELOPMENT OF A MAGNETICALLY SUSPENDED MOMENTUM WHEEL

CONTRACT NO. NAS5-11440

APRIL 1973

PREPARED FOR:

NATIONAL AERONAUTICS AND SPACE ADMINISTRATION
GODDARD SPACE FLIGHT CENTER
GREENBELT, MARYLAND 20771

PREPARED BY:

GENERAL ELECTRIC COMPANY
AEROSPACE CONTROLS AND
ELECTRICAL SYSTEMS DEPARTMENT
BINGHAMTON, NEW YORK 13902

(NASA-CR-144693) DEVELOPMENT OF A MAGNETICALLY SUSPENDED MOMENTUM WHEEL Final Report (General Electric Co.) 107 p HC $5.50 CSCL 22E

Unclas G3/17 05092

GENERAL ELECTRIC

AIRCRAFT EQUIPMENT DIVISION BINGHAMTON, NEW YORK

1. Report No.	2. Government Accession No.	3. Recipient's Catalog No.

4. Title and Subtitle	5. Report Date
DEVELOPMENT OF A MAGNETICALLY SUSPENDED MOMENTUM WHEEL	April 1973
	6. Performing Organization Code
7. Author(s) S. B. Hamilton	8. Performing Organization Report No. ACS 10,417
9. Performing Organization Name and Address General Electric Company Binghamton, New York, 13902	10. Work Unit No.
	11. Contract or Grant No. NAS5-11440
12. Sponsoring Agency Name and Address National Aeronautics and Space Administration Goddard Space Flight Center Greenbelt, Maryland Technical Monitor: L.J.Veillette	13. Type of Report and Period Covered Final Report
	14. Sponsoring Agency Code

15. Supplementary Notes

16. Abstract

An engineering model of a magnetically suspended momentum wheel was designed, fabricated, and tested under laboratory conditions. The basic unit consisted of two magnet bearings, a sculptured aluminum rotor, brushless dc spin motor, and electronics. The magnet bearings, utilizing rare-earth cobalt-samarium magnets were active radially and passive axially.

The results of the program showed that momentum wheels with magnetic bearings are feasible and operable, and that magnetic bearings of this type are capable of being used for applications where high capacity, high stiffness, and low power consumption are required. The tests performed developed criteria for improved performance for future designs.

17. Key Words (Selected by Author(s))	18. Distribution Statement
Magnetic suspension Magnetic bearing Momentum wheel	

19. Security Classif. (of this report)	20. Security Classif. (of this page)	21. No of Pages	22. Price*
Unclassified	Unclassified	106	

*For sale by the Clearinghouse for Federal Scientific and Technical Information, Springfield, Virginia 22151.

PREFACE

An engineering model of a magnetically suspended momentum wheel was designed, fabricated, and tested under laboratory conditions. The basic unit consisted of two magnet bearings, a sculptured aluminum rotor, brushless dc spin motor, and electronics. The magnet bearings, utilizing rare-earth cobalt-samarium magnets were active radially and passive axially.

The results of the program showed that momentum wheels with magnetic bearings are feasible and operable, and that magnetic bearings of this type are capable of being used for applications where high capacity, high stiffness, and low power consumption are required. The tests performed developed criteria for improved performance for future designs.

TABLE OF CONTENTS

LIST OF ILLUSTRATIONS

LIST OF ILLUSTRATIONS (cont'd)

LIST OF TABLES

Section 1
INTRODUCTION AND SUMMARY

An engineering model of a magnetically suspended momentum wheel was designed, fabricated and tested by the General Electric Company under contract from the NASA Goddard Space Flight Center. The program resulted in demonstrating that high capacity, high stiffness bearings were practical and applicable to momentum wheels, and resulted in uncovering some of the technical design problems associated with this type of bearing. Because of their potential long-life and low drag torque, bearings using electric and magnetic fields have been under study and predevelopment for some time. In the early 1960's, the Air Force (through Wright-Patterson Air Force Base) funded significant efforts in electric, magnetic and superconducting bearings for gyroscopes and mass supporting applications. The General Electric Company participated heavily in these developments (References 1, 2, 3), particularly in the area of electrostatic and superconducting gyros. The University of Virginia did considerable development of magnetic bearing suspension (Reference 4), again particularly for gyroscopes. These programs enjoyed various degrees of success but were severely cut back in the mid-to-late sixties due to funding limitations, some technical difficulties, and because there appeared to be less need for these devices (conventional gyros were achieving large performance improvements, as were ball bearings).

Of the various methods of using electric and magnetic fields for providing non-contacting bearings, the magnetic bearing operating in the attractive mode holds the greatest potential because of its relatively high force capability. In the past 15 years, several magnetic bearings of various designs have been fabricated (References 3, 4, 5). These generally have been of experimental nature and have not had practical application, although demonstrating general principles and indicating possible potential. Recent advances in magnetic materials and microelectronics now allow the design of practical magnetic bearings that could have wide application in long-life aerospace missions.

Magnetic suspension can be achieved in three basic ways:

1. Permanent Magnetic Repulsion - the repulsion force between like poles of permanent magnets can be utilized to achieve a simple magnetic bearing. However, even with the best presently available magnets, the achievable force and force gradient per unit weight is generally too low for practical consideration.

2. Reluctance (Passive) - the self-restoring magnetic reluctance force can be used to achieve simple passive suspension. Moderate forces and force gradients in a reasonable bearing weight can be achieved.

3. Magnetic Attraction (Active - servo controlled) - the use of the attractive magnetic force between pole faces can be effectively utilized by employing servo-controlled electromagnets. High forces and force gradients, with low bearing weight, can be achieved

It should be noted that completely passive magnetic suspension cannot be achieved (Earnshaws theorem). At least one axis must be actively controlled (with a servo-loop).

For the magnetically suspended momentum wheel (MSMW), the active-radial, passive-axial bearing was selected because of its high stiffness capability, high reliability, and low power. A picture of the engineering model is shown in Figure 1-1 and shows the momentum wheel, the magnetic bearings, the support structure, and the electronics used for the bearings and the spin motor. The bearings utilized rare-earth cobalt-samarium permanent magnets of high coersive force to minimize weight and maximize bearing stiffness.

The testing of the engineering model, conducted for the past year, has demonstrated that this bearing design is functionally superior to past designs and has indicated the problem areas that must be addressed in future designs. Probably the key area to be investigated is the relationship between bearing servo bandwidth, maximum possible rotor speed, and the structural resonances in the rotor/shaft/bearing combination. For the active radial bearing, the bandwidth of the bearing servos is limited principally

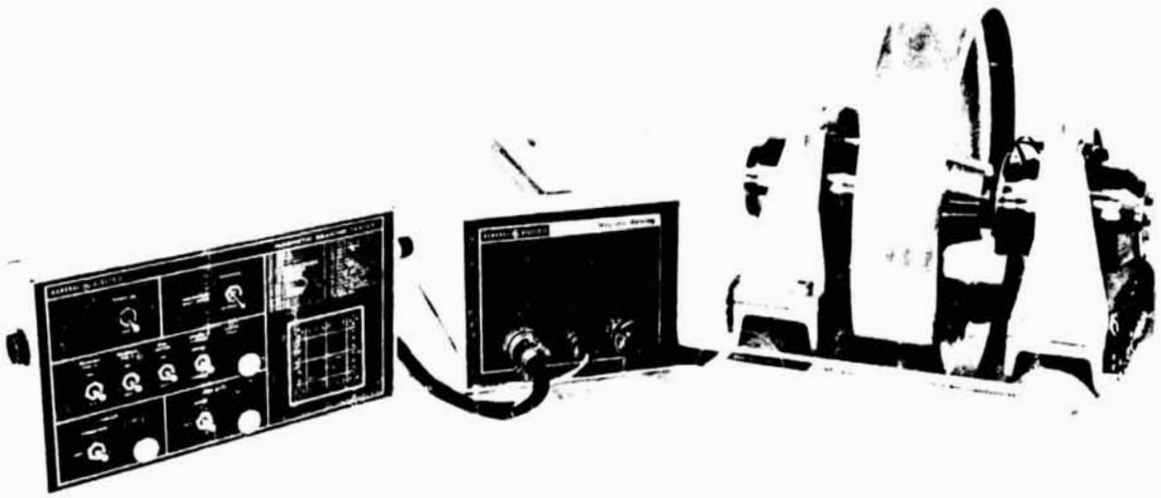

Figure 1-1. Magnetically Suspended Momentum Wheel, Engineering Model

by the bending resonance of the shaft. With this limitation, the maximum rotor speed is determined by the magnitude of the rotor "wobble" at the spin frequency due to imbalance and mechanical misalignments. The engineering model had a maximum spin speed of approximately 5000 RPM due to the above causes. Future designs, utilizing either larger diameter magnets with a larger shaft or a different design approach to achieve structural stiffness, should be able to spin at any desired speed.

Section 2

MAGNETICALLY SUSPENDED MOMENTUM WHEEL EQUIPMENT DESCRIPTION

The magnetically suspended momentum wheel, which is shown again ... the picture of Figure 2-1, with its electronics has the following features:

- Two radially active magnet bearing systems which provide high stiffness and good damping.
- A sculptured momentum rotor.
- A highly efficient brushless dc spin motor system.
- Servo and control electronics utilized micro circuits.

The physical and electrical characteristics of the various subassemblies of the engineering model are given in Table 2-1.

TABLE 2-1

DESCRIPTION OF PHYSICAL AND ELECTRICAL CHARACTERISTICS

Magnetically Suspended Momentum Wheel, Engineering Model

Angular Momentum - actual	74.57 N-m-s	(55 ft-lb-sec)
- design	101.69 N-m-s	(75 ft-lb-sec)
Maximum Speed - actual	523 rad/sec	(5000 RPM)
- design	712 rad/sec	(6800 RPM)
Size - diameter	0.3556 meters	(14 inches)
- Length	0.3493 meters	(13.75 inches)
Weight	14.97 kilograms	(33 pounds)
Power - zero disturbance	10 watts	
- spin-up	32 watts	
- Full bearing load	18.5 watts	
Spin-up Time	1.1 hours	

Magnetic Bearing (per pair)

Load capability	34.02 kilograms	(75 pounds)
Stiffness - radial	3,572,000 kg/m	(200,000 lb/in)
- axial	30,358 kg/m	(1700 lb/in)
Weight (each)	2.812 kilograms	(6.2 pounds)
Position Sensor - type	magneto-resistor	
- gain	1378 V/m	(35 mv/mil)

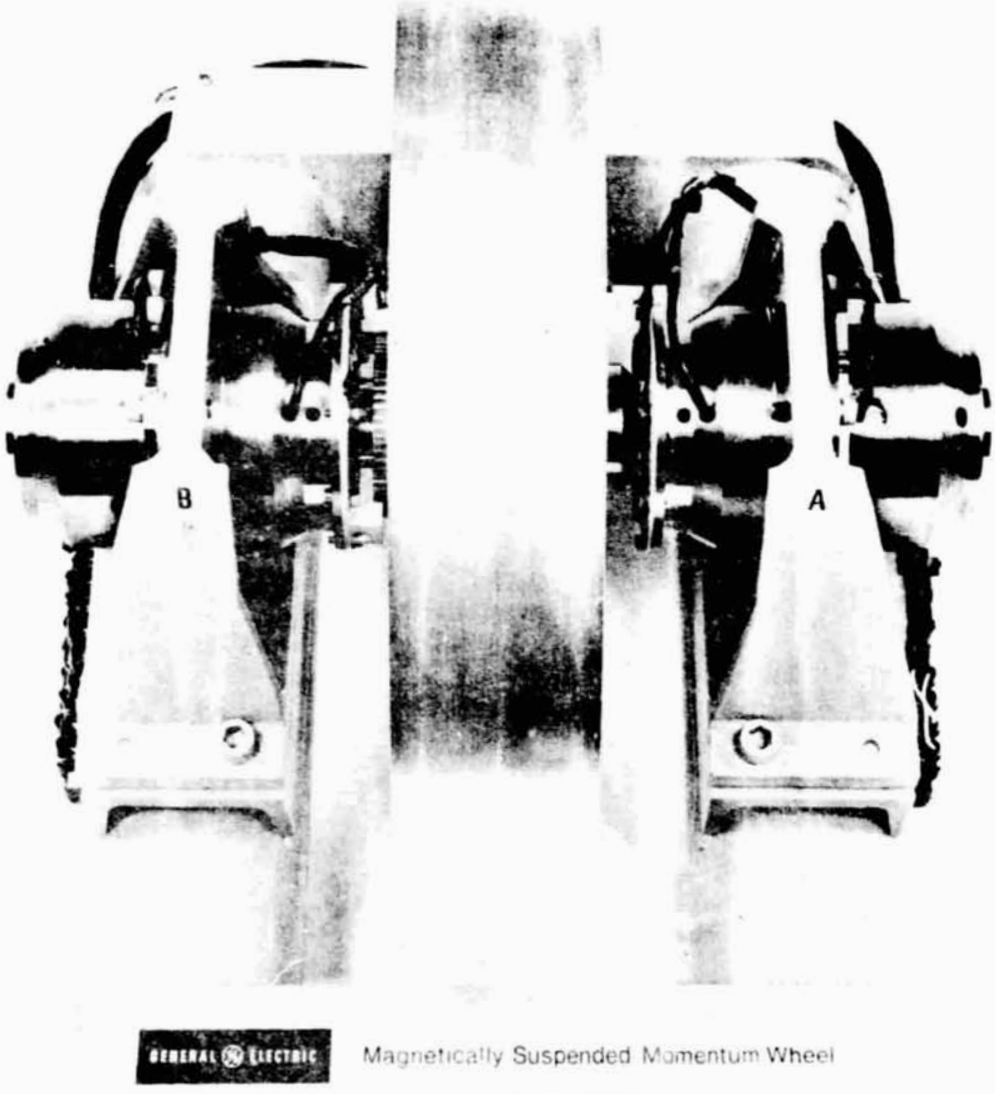

Figure 2-1. Rotor and Magnetic Bearing Assembly

Section 3
MAGNETIC BEARING DESIGN

The structural configuration of the magnetic bearing design is shown in Figure 3-1. The stator of the bearing consists of a stack of 4-pole punchings and two shell type flux return sections. Each pole piece is equippped with a control winding and diametrically opposite windings are connected in series, thus forming two separate control circuits. The punchings may be made of 3.5% Si-Fe, 50% Ni-Fe or Vanadium Permendur. The shell-type sections enclose the punchings as shown and they may be provided with a flange for purposes of mounting. The design of the magnetic bearing structure used in the engineering model is shown in Appendix B.

The rotor consists of alternately stacked rings of iron and ring-shaped permanent magnets which are axially magnetized. The magnets are polarized such that their flux enters from both sides into the central ring-section which is also preferably composed of a stack of punchings and located directly underneath the four pole pieces of the stator. The solid soft iron rings at the left and right end of the bearing provide, in combination with the shell-type structure of the stator, a return path for the fluxes of the two permanent magnets and, at the same time, serve to furnish passive axial support of the bearing. In order to achieve a satisfactory degree of axial stiffness, part of the surface of these iron rings as well as the inner surface of the circular end-opening of the shells are recessed by machining one or several grooves into their surfaces. In this manner a high flux density level in the airgap around these narrow ring sections is obtained. Since the force which is required to displace the shaft axially is proportional to B^2 and the number of ring-sections, a high degree of stiffness can be achieved. The magnet material to be used should belong to the family of rare-earth-Cobalt magnets which exhibit a very large coercive force and, therefore, can be designed to have a short axial length and relatively large cross-section which contribute to a compact design of the bearing.

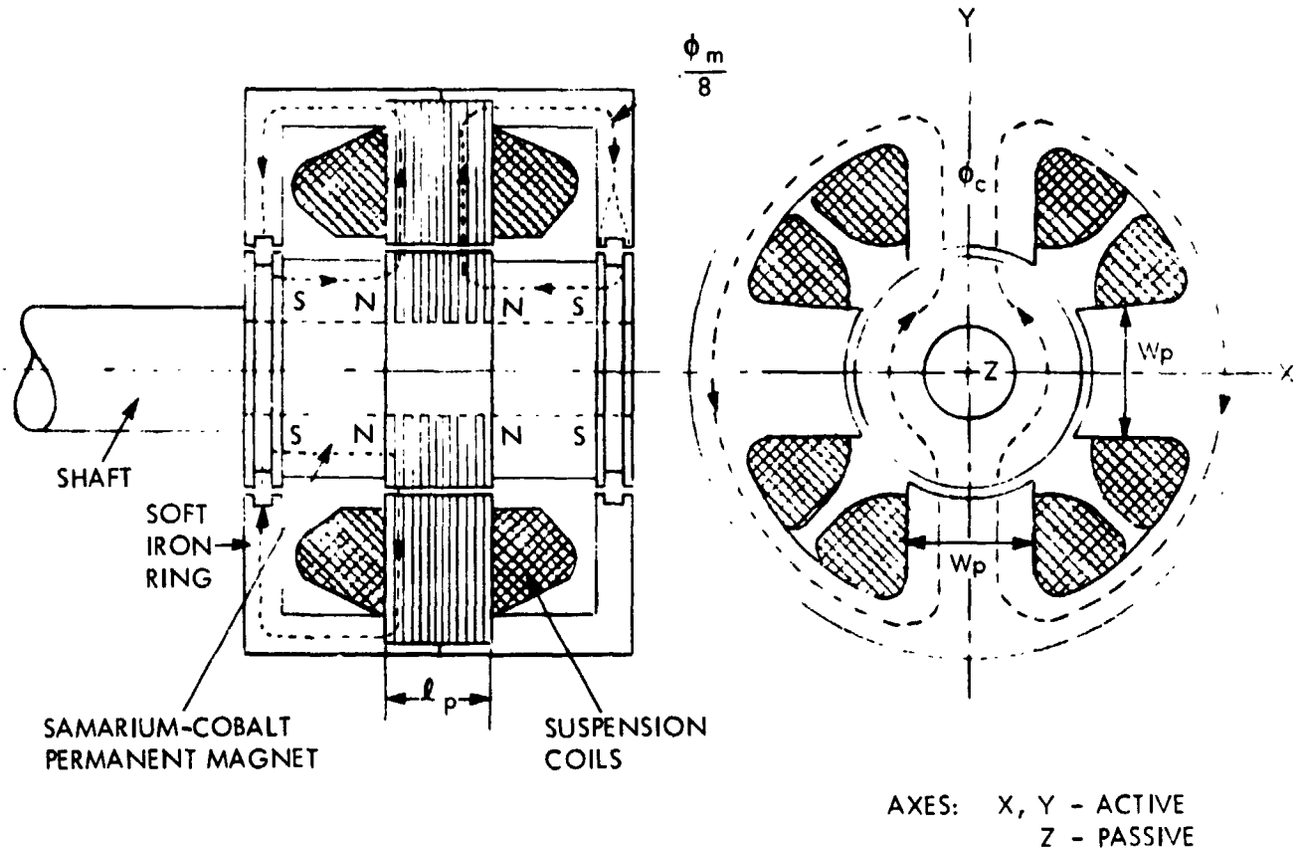

Figure 3-1. Active Radial and Passive Axial Magnetic Journal Bearing

The total flux of the permanent magnets enters and leaves the stator in the radial direction in eight distinguishable flux paths which converge through the cylindrical housing towards the circular airgaps of the axial support ring sections. One of these flux paths is shown as a dotted line in the drawing. There are four such flux paths in each, the vertical and horizontal plane.

It is easily understood that the flux ϕ_m of the permanent magnets cannot provide a stable support of the rotor, and, therefore, the shaft, since an infinitely small radial displacement from its theoretical zero position will cause it to be attracted to any one of the four pole pieces. Stability can be achieved by provision of control ampere turns in each axis via the control windings. The flux path of the controlling flux ϕ_c is shown as dashed lines in Figure 3-1 for the case of the vertical axis and one may observe that as indicated it causes a decrease in flux density in the airgap of the lower pole while, at the same time, the flux density in the upper gap will be increased resulting in an upward directed total force. Reversal of this flux results in a reversal of the direction of this force. Thus, any radial load exerted upon the shaft can be supported by suitable control of the control winding currents.

In order to arrive at a stable support, these currents must, in both axes, be proportional to the radial displacement components. To achieve this, position detectors are required in both axes which convert the magnitudes of displacement into electrical signals. These signals are then amplified by electronic amplifiers, containing suitable networks for dynamic stabilization, and thus converted into currents within the control windings. Capacititive, inductive, Hall-Effect, magneto-resistive or photo-electrical position sensors can be employed.

Let B_o = Bias flux density in the airgaps resulting from the permanent magnets (Gauss)

$\triangle B$ = Change of gap flux density due to control ampere turns (Gauss)

w_p = Width of pole piece (cm)

ℓ_p = Axial length of pole piece (cm)

The force of attraction between two iron surfaces of area A (cm^2) separated by a gap in which a flux density B (Gauss) (1 Gauss = 10^4 Tesla) exists is given by the following generally known formula:

$$F = \frac{A}{8\pi} \cdot B^2 \cdot 10^{-5} \quad \text{(Newtons)} \tag{3-1}$$

It was concluded before that for the direction of fluxes as indicated in Figure 3-1 an upward directed force exists. The value of this force can then be expressed by the following equation:

$$F = \frac{A}{8\pi} \left[(B_o + \Delta B)^2 - (B_o - \Delta B^2) \right] \cdot 10^{-5} = \frac{A}{2\pi} B_o \cdot \Delta B \cdot 10^{-5} \tag{3-2}$$

Since $A = \ell_p \cdot w_p \ (cm^2)$,

$$F = \frac{\ell_p \cdot w_p \cdot B_o \cdot \Delta B}{2\pi} \cdot 10^{-5} \quad \text{(Newtons)} \tag{3-3}$$

Expressing B_o and ΔB in Kilo-Gauss, ℓ_p and w_p in inches and the force F in pounds, equation (3-3) can be converted into the following form:

$$F = 2.30834 \ \ell_p \cdot w_p \cdot B_o \cdot \Delta B \quad \text{(lbs)} \tag{3-4}$$

3.1 DETAILED STUDY OF FORCES FOR THE CASE OF A RADIALLY DISPLACED ROTOR

In the case that the rotor is radially displaced by a certain fraction of the airgap, the above simple relationships do not hold true any more and, therefore, must be modified in order to obtain better information about the actual performance characteristics of the bearing.

First, considering Figure 3-2, which shows a cross-sectional view of the bearing with the rotor displaced by an amount

$$\delta = \epsilon \cdot g_o$$

where g_o = airgap at $\delta = 0$, relationships between airgap permeances and flux distributions will be derived.

Let P_1 and P_2 = permeances of upper and lower gap, respectively, and P_h = permeances of left and right gap.

Let AT_m = Magnetomotive Force of permanent magnet across gaps and AT_c = Magnetomotive Force furnished from a single control winding.

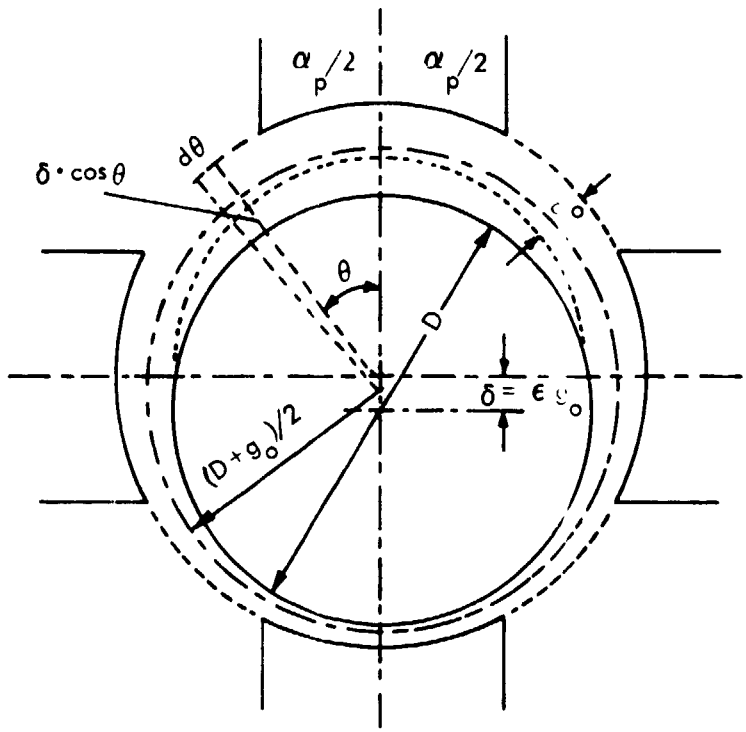

Figure 3-2. Cross-Sectional View of Bearing

The fluxes caused by the permanent magnets are then simply determined by the following relationships:

$$\varphi_{m_1} = AT_m \cdot P_1 \tag{3-5a}$$

$$\varphi_{m_2} = AT_m \cdot P_2 \tag{3-5b}$$

$$\varphi_{m_h} = AT_m \cdot P_h \tag{3-5c}$$

Total flux of both magnets:

$$\phi_{m_{tot}} = \phi_{m_1} + \phi_{m_2} + 2\phi_{m_h}$$

The fluxes resulting from the magnetomotive forces of the windings on the upper and lower pole pieces can be derived from a simple equivalent circuit diagram as shown in Figure 3-3. (For an assumed vertical displacement the ampere-turns on the horizontal poles are zero.)

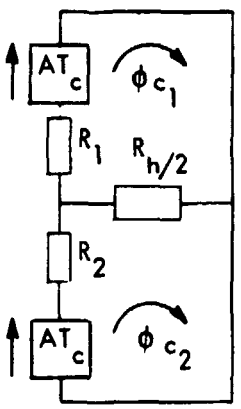

Figure 3-3. Equivalent Circuit Diagram

For convenience, the permeances are here replaced by their corresponding reluctances

$$R_1 = \frac{1}{P_1}; \quad R_2 = \frac{1}{P_2}; \quad R_h = \frac{1}{P_h}$$

The following relationships exist:

$$\phi_{c_1} R_1 + R_h/2 \quad - \phi_{c_2} R_h/2 = AT_c \tag{3-6}$$

$$\phi_{c_1} R_1 + \phi_{c_2} R_2 = 2 \cdot AT_c \tag{3-7}$$

Solving equations (3-6) and (3-7) for φ_1 and φ_2 yields:

$$\varphi_{c_1} = \frac{R_h + R_2}{R_1 \cdot R_2 + \frac{R_h}{2}(R_1 + R_2)} \cdot AT_c \tag{3-8}$$

$$\varphi_{c_2} = \frac{R_h + R_1}{R_1 \cdot R_2 + \frac{R_h}{2}(R_1 + R_2)} \cdot AT_c \tag{3-9}$$

Converting back to expressions in terms of permeances, one obtains:

$$\varphi_{c_1} = 2 \cdot AT_c \frac{P_h + P_2}{P_{tot}} \cdot P_1 \tag{3-10}$$

$$\varphi_{c_2} = 2 \cdot AT_c \frac{P_h + P_1}{P_{tot}} \cdot P_2 \tag{3-11}$$

and $$2\varphi_{c_h} = 2 \cdot AT_c \frac{P_2 - P_1}{P_{tot}} \cdot P_h \tag{3-12}$$

where $P_{tot} = P_1 + P_2 + 2P_h$

The following identities exist:

$$\frac{2(P_h + P_2)}{P_{tot}} = 1 + \frac{P_2 - P_1}{P_{tot}}$$

$$\frac{2(P_h + P_1)}{P_{tot}} = 1 - \frac{P_2 - P_1}{P_{tot}}$$

Taking into account the expressions of equations (3-6) and (3-7), the various airgap fluxes are then given by the following equations:

$$\varphi_1 = \varphi_{m_1} + \varphi_{c_1} = \left[AT_m + AT_c \left(1 + \frac{P_2 - P_1}{P_{tot}} \right) \right] P_1 \tag{3-13}$$

$$\phi_2 = \phi_{m_2} - \phi_{c_2} = \left[AT_m - AT_c \left(1 - \frac{P_2 - P_1}{P_{tot}} \right) \right] P_2 \qquad (3\text{-}14)$$

$$2\phi_h = 2 (\phi_{m_h} + \phi_{c_h}) = \left[AT_m + AT_c \frac{P_2 - P_1}{P_{tot}} \right] \cdot 2 P_h \qquad (3\text{-}15)$$

The total ampere turns acting upon airgap permeances P_1, P_2, and P_h, respectively, may thus be defined as AT_1, AT_2, and AT_h and are expressed by the bracketed terms of these equations.

It is generally known that the force existing between two magnetized bodies separated by a gap is proportional to the rate of change of permeance of the space between these bodies as a function of displacement and the square of the magnetomotive force across that gap. This force is, in general terms, defined by the following equation:

$$F = 1/2 \frac{dP}{d\delta} \cdot (MMF)^2 \cdot 4\pi \cdot 10^{-7} \quad \text{(Newtons)} \qquad (3\text{-}16)$$

The total force acting upon the bearing rotor is then the sum of three forces $F_1 + F_2 + F_h$, namely

$$F = 2\pi \cdot 10^{-7} \left[\frac{d P_1}{d\delta} (AT_1)^2 + \frac{d P_2}{d\delta} (AT_2)^2 + 2 \frac{d P_h}{2\delta} (AT_h)^2 \right] \qquad (3\text{-}17)$$

Equations for the various permeances and their derivatives must now be derived. Since, for all practical considerations, the fringe permeances along the pole edges contribute very little to the total force and in order to avoid over-complication of the problem, the influence of these permeances will here be neglected.

Using definitions given in Figure 3-2, one derives that the incremental permeance value of a small element of the gap having an angular width $d\theta$ and axial length ℓ_p is defined by

$$dP = \frac{D + g_o}{2} \cdot d\theta \cdot \frac{\ell_p}{g_p + \delta \cdot \cos \theta}$$

or $$dP = \frac{D + g_o}{2} \cdot \ell_p \frac{d\theta}{1 + \epsilon \cos \theta} \qquad \text{where } \epsilon = \frac{\delta}{g_o}$$

The permeance of an airgap section of angular extension $\theta_2 - \theta_1$ is then expressed by the integral

$$P = \frac{D + g_o}{2g_o} \ell_p \int_{\theta_1}^{\theta_2} \frac{d\theta}{1 + \epsilon \cos \theta} \quad \text{(cm)} \tag{3-18}$$

The solution of this integral is

$$P = \frac{D + g_o}{g_o} \cdot \ell_p \frac{1}{(1 - \epsilon^2)^{1/2}} \left[\tan^{-1}\left(\sqrt{\frac{1 - \epsilon}{1 + \epsilon}} \tan \frac{\theta}{2} \right) \right]_{\theta_1}^{\theta_2} \tag{3-19}$$

The limits of integration for P_1 are 0 to $\frac{\alpha_p}{2}$ and the value of the integral must be doubled.

Similarly, for P_2, the limits are $(\pi - \frac{\alpha_p}{2})$ to π and again the value of the integral must be multiplied by 2.

The limits for P_h are $(\pi/2 - \alpha_p/2)$ to $(\pi/2 + \alpha_p/2)$.

Inserting these limits into equation (3-19) yields:

$$P_1 = \frac{D + g_o}{g_o} \frac{2\ell_p}{(1 - \epsilon^2)^{1/2}} \tan^{-1}\left(\sqrt{\frac{1 - \epsilon}{1 + \epsilon}} \tan \frac{\alpha_p}{4} \right) \tag{3-20}$$

$$P_2 = \frac{D + g_o}{g_o} \frac{2\ell_p}{(1 - \epsilon^2)^{1/2}} \tan^{-1}\left(\sqrt{\frac{1 + \epsilon}{1 - \epsilon}} \tan \frac{\alpha_p}{4} \right) \tag{3-21}$$

Derivation of the expression for P_h, or better $2 \cdot P_h$, (see equation (3-17)) will be presented since the result is not as obvious as that of equations (3-20) and (3-21). Letting temporarily

$$\frac{D + g_o}{g_o} \frac{\ell_p}{(1 - \epsilon^2)^{1/2}} = C$$

and $$\sqrt{\frac{1 - \epsilon}{1 + \epsilon}} = E$$

one finds from equation (3-19) for the previously given limits:

$$P_h = C \left[\tan^{-1} \left(E \tan \left(\frac{\pi}{4} + \frac{\alpha_p}{4} \right) \right) - \tan^{-1} \left(E \tan \left(\frac{\pi}{4} - \frac{\alpha_p}{4} \right) \right) \right]$$

$$P_h = C \cdot \tan^{-1} \frac{E \left[\tan \left(\frac{\pi}{4} + \frac{\alpha_p}{4} \right) - \tan \left(\frac{\pi}{4} - \frac{\alpha_p}{4} \right) \right]}{1 + E^2 \tan \left(\frac{\pi}{4} + \frac{\alpha_p}{4} \right) \tan \left(\frac{\pi}{4} - \frac{\alpha_p}{4} \right)}$$

$$\tan \left(\frac{\pi}{4} + \frac{\alpha_p}{4} \right) = \frac{1 + \tan \frac{\alpha_p}{4}}{1 - \tan \frac{\alpha_p}{4}}$$

$$\tan \left(\frac{\pi}{4} - \frac{\alpha_p}{4} \right) = \frac{1 - \tan \frac{\alpha_p}{4}}{1 + \tan \frac{\alpha_p}{4}}$$

$$P_h = C \cdot \tan^{-1} \frac{4 \cdot E \tan \frac{\alpha_p}{4}}{(1 + E^2)\left(1 - \tan^2 \frac{\alpha_p}{4}\right)}$$

since $$\frac{2 \tan \frac{\alpha_p}{4}}{1 - \tan^2 \frac{\alpha_p}{4}} = \tan \frac{\alpha_p}{2}$$

$$P_h = C \tan^{-1}\left(\frac{2E}{1+E^2}\tan\frac{\alpha_p}{2}\right)$$

but $$\frac{2E}{1+E^2} = \sqrt{1-\epsilon^2}$$

This yields finally:

$$2P_h = \frac{D+g_o}{g_o}\;\frac{2\ell_p}{(1-\epsilon^2)^{1/2}}\;\tan^{-1}\left(\sqrt{1-\epsilon^2}\tan\frac{\alpha_p}{2}\right) \qquad (3\text{-}22)$$

The total gap-permeance of the flux path of both permanent magnets is then given as the sum of equations (3-20), (3-21) and (3-22). The result amounts to:

$$P_{tot} = \frac{D+g_o}{g_o}\;\frac{2\ell_p}{(1-\epsilon^2)^{1/2}}\;\tan^{-1}\left[\frac{1-\epsilon^2/2}{(1-\epsilon^2)^{1/2}}\tan\alpha_p\right] \qquad (3\text{-}23)$$

In the region $\epsilon = 0$ to 0.5, the term $(1-\epsilon^2/2)(1-\epsilon^2)^{1/2}$ is very close to unity. At, e.g., $\epsilon = 0.25$, it amounts to only 1.0005.

Therefore, the total permeance as a function of per unit displacement "ϵ" is expressed by:

$$P_{tot} \cong \frac{(D+g_o)\,2\ell_p\,\alpha_p}{g_o\sqrt{1-\epsilon^2}} \qquad (3\text{-}24)$$

For the case of zero displacement, this equation reduces to

$$P_{tot_o} = \frac{2(D+g_o)\,\ell_p\,\alpha_p}{g_o} \qquad (3\text{-}25)$$

which is exactly that value of permeance one would have found in simply dividing the total gap area under the poles by the airgap g_o.

In equations (3-13) to (3-15), the term $(P_2 - P_1)/P_{tot}$ occurs, which also must be given in terms of "ϵ" and "α_p". In deriving the equation, let temporarily in equations (3-20), (3-21) and (3-24)

$$\frac{2\,(D + g_o) \cdot \ell_p}{g_o \sqrt{1 - \epsilon^2}} = K$$

Then one finds:

$$P_2 - P_1 = K \left[\tan^{-1}\left(\sqrt{\frac{1+\epsilon}{1-\epsilon}} \tan\frac{\alpha_p}{4}\right) - \tan^{-1}\left(\sqrt{\frac{1-\epsilon}{1+\epsilon}} \tan\frac{\alpha_p}{4}\right)\right]$$

$$P_2 - P_1 = K \tan^{-1} \frac{\sqrt{\frac{1+\epsilon}{1-\epsilon}} - \sqrt{\frac{1-\epsilon}{1+\epsilon}} \tan\frac{\alpha_p}{4}}{1 - \tan^2\frac{\alpha_p}{4}}$$

$$P_2 - P_1 = K \tan^{-1}\left(\frac{\epsilon}{\sqrt{1-\epsilon^2}} \cdot \sin\frac{\alpha_p}{2}\right); \text{ since } \frac{2 \cdot \tan\frac{\alpha_p}{4}}{1 + \tan^2\frac{\alpha_p}{4}} = \sin\frac{\alpha_p}{2}$$

$$\frac{P_2 - P_1}{P_{tot}} = \frac{1}{\alpha_p} \tan^{-1}\left[\frac{\epsilon}{\sqrt{1-\epsilon^2}} \cdot \sin\frac{\alpha_p}{2}\right] \qquad (3\text{-}26)$$

The effective magnetomotive forces at the different pole gaps are then given by the following expressions:

$$AT_1 = AT_m + AT_c \left[1 + \frac{1}{\alpha_p} \tan^{-1}\left(\frac{\epsilon}{\sqrt{1-\epsilon^2}} \sin\frac{\alpha_p}{2}\right)\right] \qquad (3\text{-}27)$$

$$AT_2 = AT_m - AT_c \left[1 - \frac{1}{\alpha_p} \tan^{-1}\left(\frac{\epsilon}{\sqrt{1-\epsilon^2}} \sin\frac{\alpha_p}{2}\right)\right] \qquad (3\text{-}28)$$

$$AT_h = AT_m + AT_c \frac{1}{\alpha_p} \tan^{-1}\left[\frac{\epsilon}{\sqrt{1-\epsilon^2}} \sin\frac{\alpha_p}{2}\right] \qquad (3\text{-}29)$$

It remains now to determine the rate of change of permeance $dP_1/d\delta$, $dP_2/d\delta$, and $dP_h/d\delta$ to find an equation for the combined force acting upon the bearing according to equations (3-6) and (3-7). Finding the derivatives of equations (3-20), (3-21) and (3-22) with respect to ϵ is straightforward but quite laborious. These expressions must then be multiplied by $d\epsilon/d\delta = 1/g_o$. Without going into details, the following results are obtained for the derivatives:

$$\frac{dP_1}{d\delta} = -\frac{(D + g_o) \cdot \ell_p}{g_o^2} \left[\frac{1}{1 - \epsilon^2} \frac{\sin \frac{\alpha_p}{2}}{1 + \epsilon \cos \frac{\alpha_p}{2}} \right.$$

$$\left. - 2\epsilon (1 - \epsilon^2)^{-3/2} \tan^{-1}\left(\sqrt{\frac{1 - \epsilon}{1 + \epsilon}} \tan \frac{\alpha_p}{4}\right)\right] \qquad (3\text{-}30)$$

$$\frac{dP_2}{d\delta} = +\frac{(D + g_o) \cdot \ell_p}{g_o^2} \left[\frac{1}{1 - \epsilon^2} \frac{\sin \frac{\alpha_p}{2}}{1 - \epsilon \cos \frac{\alpha_p}{2}} \right.$$

$$\left. + 2\epsilon (1 - \epsilon^2)^{-3/2} \tan^{-1}\left(\sqrt{\frac{1 + \epsilon}{1 - \epsilon}} \tan \frac{\alpha_p}{4}\right)\right] \qquad (3\text{-}31)$$

$$2 \cdot \frac{dP_h}{d\delta} = \epsilon \frac{(D + g_o) \cdot \ell_p}{g_o^2} \left[- \frac{1}{1 - \epsilon^2} \frac{\sin \alpha_p}{1 - \epsilon^2 \cdot \sin^2 \frac{\alpha_p}{2}} \right.$$

$$\left. + 2 (1 - \epsilon^2)^{-3/2} \tan^{-1}\left(\sqrt{1 - \epsilon^2} \tan \frac{\alpha_p}{2}\right)\right] \qquad (3\text{-}32)$$

Combining now, equations (3-30), (3-27); (3-31), (3-28) and (3-32), (3-29) with the three succeeding terms of equation (3-17), respectively, yields three force components F_1, F_2 and F_h, the sum of each represents the force exerted upon the active portion of the bearing, namely:

$$F_1 = \frac{2\pi (D+g_o)\, \ell_p}{10^7 (1-\epsilon^2) g_o^2} \left[AT_m + AT_c \left[1 + \frac{1}{\alpha_p} \tan^{-1} \left(\frac{\epsilon}{\sqrt{1-\epsilon^2}} \sin \frac{\alpha_p}{2} \right) \right] \right]^2 \cdot \left[\frac{\sin \frac{\alpha_p}{2}}{1 + \epsilon \cos \frac{\alpha_p}{2}} - \frac{2\epsilon}{\sqrt{1-\epsilon^2}} \tan^{-1} \left(\sqrt{\frac{1-\epsilon}{1+\epsilon}} \tan \frac{\alpha_p}{4} \right) \right] \quad (3\text{-}33)$$

$$F_2 = + \frac{2\pi (D+g_o)\, \ell_p}{10^7 (1-\epsilon^2) g_o^2} \left[AT_m - AT_c \left[1 - \frac{1}{\alpha_p} \tan^{-1} \left(\frac{\epsilon}{\sqrt{1-\epsilon^2}} \sin \frac{\alpha_p}{2} \right) \right] \right]^2 \cdot \left[\frac{\sin \frac{\alpha_p}{2}}{1 - \epsilon \cos \frac{\alpha_p}{2}} + \frac{2\epsilon}{\sqrt{1-\epsilon^2}} \tan^{-1} \left(\frac{1+\epsilon}{1-\epsilon} \tan \frac{\alpha_p}{4} \right) \right] \quad (3\text{-}34)$$

$$F_h = + \frac{2\pi (D+g_o)\, \ell_p}{10^7 (1-\epsilon^2) g_o^2} \left[AT_m + AT_c \cdot \frac{1}{\alpha_p} \tan^{-1} \left(\frac{\epsilon}{\sqrt{1-\epsilon^2}} \sin \frac{\alpha_p}{d} \right) \right]^2 \cdot \left[- \frac{\epsilon \sin \alpha_p}{1 - \epsilon^2 \sin^2 \frac{\alpha_p}{2}} + \frac{2\epsilon}{\sqrt{1-\epsilon^2}} \tan^{-1} \left(\sqrt{1-\epsilon^2} \tan \frac{\alpha_p}{2} \right) \right] \quad (3\text{-}35)$$

$$F = F_1 + F_2 + F_h \quad (3\text{-}36)$$

These forces are given in Newtons. Conversion into pounds changes factor "2π" into 1.41251 which differs from $\sqrt{2}$ only by 0.1 percent. Thus one can replace "2π" by "$\sqrt{2}$". The equations permit one to calculate "F" as functions of displacement and control ampere turns. A program for the Time Sharing Computer, named "MAGBR", was written for this purpose during an Independent Research and Development program. For the case of zero control ampere turns, these equations furnish the destabilizing force which, as mentioned in the introduction, is caused by the bias-flux of the permanent magnets. This force can also be calculated with sufficient

accuracy by taking the derivative of equation (3-24) with respect to δ and inserting it into equation (3-16). This yields:

$$F_{Bias} \cong \frac{4\pi\ (D + g_o)\ \ell_p}{10^7\ \ g_o^{\ 2}}\ \alpha_p\ \epsilon\ (1 - \epsilon^2)^{-3/2}\ \ (AT_m)^2 \quad \text{(Newtons)} \qquad (3\text{-}37)$$

The bias force can be expressed in terms of B_o remembering that

$$AT_m = \frac{10}{4\pi} \cdot B_o\, g_o$$

which yields

$$F_{Bias} = \frac{(D + g_o) \cdot \ell_p \cdot \alpha_p}{4\pi} \cdot 10^{-5} \cdot \epsilon\ (1 - \epsilon^2)^{-3/2}\ B_o^{\ 2} \quad \text{(Newtons)} \qquad (3\text{-}38)$$

Equation (3-38) can be converted to a form which permits one to determine the destabilizing force caused from the axial support ring sections of the bearing in case of an existing radial displacement "δ".

Letting $\alpha_p = \pi/2$ which defines the case of a continuous cylindrical gap and replacing ℓ_p by $n \cdot \lambda$, where n represents the number of axial support ring sections and λ is the axial length of each section, one arrives at the following formula for the destabilizing force which, in essence, represents an undesirable external load on the shaft:

$$F_{A_{radial}} = \frac{(D + g_o) \cdot n \cdot \lambda}{8} \cdot B_{AS}^{\ 2} \cdot 10^{-5} \cdot \epsilon\ (1 - \epsilon^2)^{-3/2} \quad \text{(Newtons)} \quad (3\text{-}39)$$

where B_{AS} = flux density within the gap of these ring sections.

Section 4

SUSPENSION CONTROL LOOP DESIGN AND SIMULATION

4.1 CALCULATED GAIN/PHASE FOR MAGNETIC BEARING

4.1.1 BASIC LOOP

Figure 4-1 shows the basic loop for translation. Note that two "open loop" responses, useful in computing closed loop performance, can be defined:

$$\text{Open Loop 1} = G_1 = \frac{\Delta x_o}{\Delta x_e}$$

$$\text{Open Loop 2} = G_2 = \frac{x_o}{\Delta x_o}$$

For translation these responses are

$$G_1 = \frac{K_n}{K_p} \quad \frac{1}{\frac{m}{2K_p} S^2 - 1}$$

$$G_2 = \frac{2K_n - 2K_p}{mS^2} = \left(\frac{K_n}{K_p} - 1\right) \frac{2K_p}{mS^2}$$

For torsion, the gains are different than translation because the position sensor location is different than the bearing force location (see Figure 4-2). For torsion, the responses are:

$$G_{1T} = \frac{K_n}{K_p} \frac{d}{d'} \quad \frac{1}{\frac{I_r S^2}{K_p (d')^2/2} - 1}$$

$$G_{2T} = \frac{K_n \frac{dd'}{2} - K_p \frac{(d')^2}{2}}{J_r S^2} = \left(\frac{K_n}{K_p} \frac{d}{d'} - 1\right) \frac{K_p \frac{(d')^2}{2}}{J_r S^2}$$

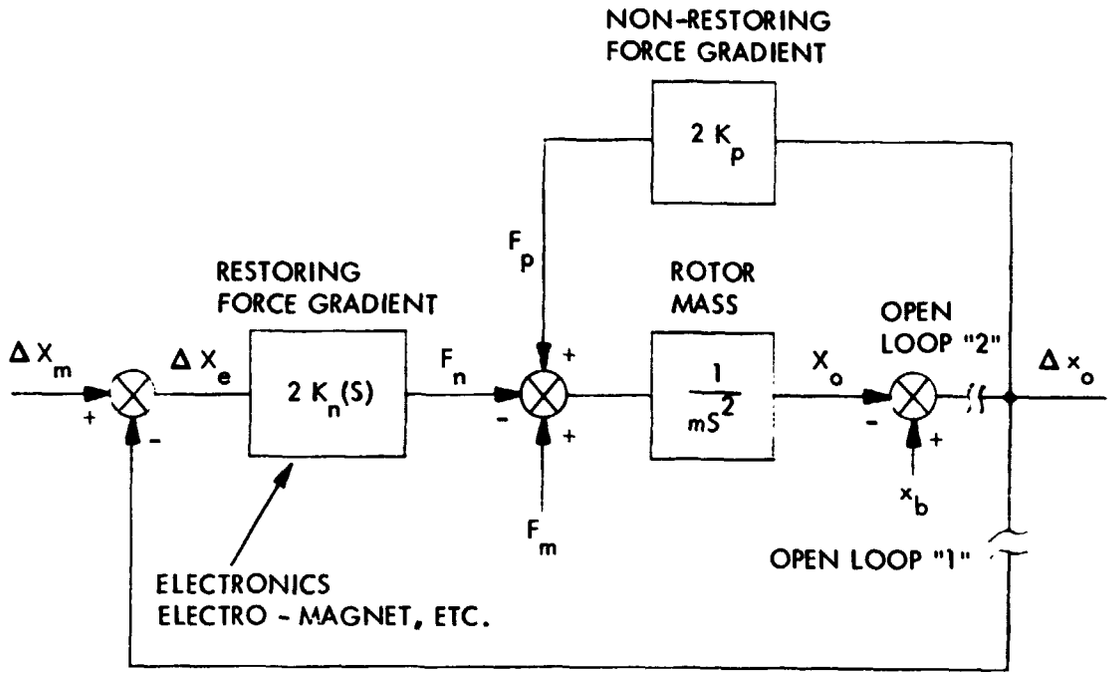

x_b = BASE MOTION DISPLACEMENT } REFERENCED TO
x_o = SUSPENDED ROTOR DISPLACEMENT } INERTIAL SPACE

Δx_o = ROTOR MOTION WITH RESPECT TO BASE (I.E., GAP DISPLACEMENT)

F_m = EXTERNAL FORCE APPLIED TO ROTOR

Δx_m = EXTERNAL SIGNAL INSERTED IN K_n LOOP (I.E., SUMMED INTO ELECTRONICS)

K_n, K_p = RESTORING AND NON-RESTORING FORCE GRADIENTS (PER BEARING)

OPEN LOOP "1" $\quad G_1 = \dfrac{\Delta x_o}{\Delta x_e}$

OPEN LOOP "2" $\quad G_2 = \dfrac{x_o}{\Delta x_o}$

Figure 4-1. Magnetic Bearing System - Linear Response for Translation

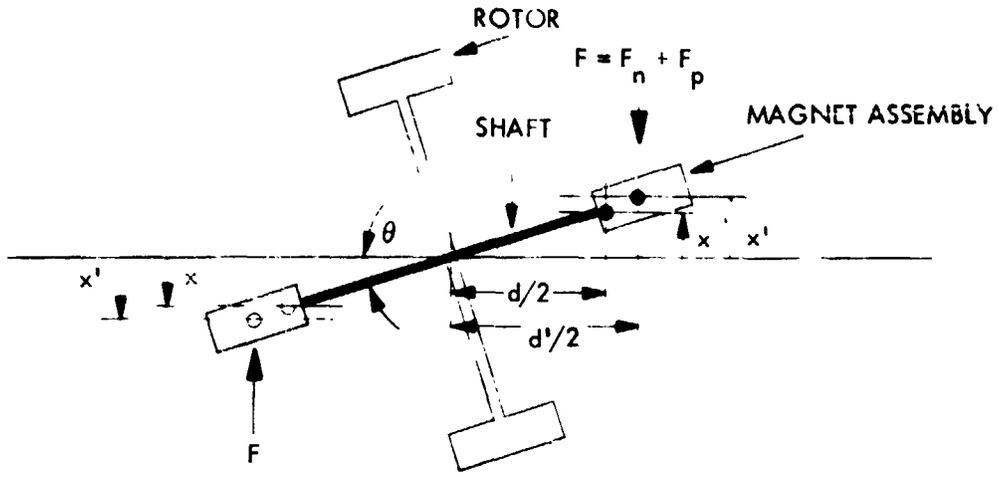

F = FORCE FROM MAGNETIC BEARING - BOTH F_n AND F_p ACT THROUGH CENTER OF BEARING (ON AVERAGE)

x' = DISPLACEMENT OF CENTER OF BEARING

x = DISPLACEMENT AT INNER POSITION SENSOR LOCATION

J = POLAR MOMENT OF INERTIA ABOUT cg

FOR TORSION

$$\text{TORQUE} = T = (F_n - F_p)\, d' = (K_n x - K_p x')\, d'$$

$$= \left(K_n \frac{d}{2}\theta - K_p \frac{d'}{2}\theta\right) d'$$

SO

$$\frac{T}{\theta} = K_n \frac{d\,d'}{2} - K_p \frac{(d')^2}{2}$$

$$K_{nT} = K_n \frac{d\,d'}{2}$$

$$K_{pT} = K_p \frac{(d')^2}{2}$$

$$\frac{K_{nT}}{K_{pT}} = \frac{K_n}{K_p}\frac{d}{d'}$$

Figure 4-2. Magnetic Bearing - Geometry for Torsional Response

Now, referring to Figure 4-1, the following give the closed loop responses:

Base Motion

$$\frac{x_o}{x_b} = \frac{G_2}{1 + G_2}$$

$$\frac{\Delta x_o}{x_b} = \frac{1}{1 + G_2}$$

Response to signal inserted in electronics

$$\frac{\Delta x_o}{\Delta x_m} = \frac{G_1}{1 + G_1}$$

At DC: $$\left(\frac{\Delta x_o}{\Delta x_m}\right)_{DC} = \frac{K_n/K_p}{K_n/K_p - 1}$$

Response to force at rotor (i.e., balance)

$$\frac{F_n}{F_m} = \frac{G_1}{1 + G_1}$$

The above apply for translational motions; for torsion substitute G_{1T} and G_{2T}.

4.1.2 ELECTRONICS CHANNEL

Figure 4-3 illustrates the electronics implementation with present values. For linear (small-signal) inputs, the compensation consists of:

a. Notch filter

b. Integrator

c. Lead-lag (combines lead-lag and lag-lead of Figure 4-3)

d. Power amplifier

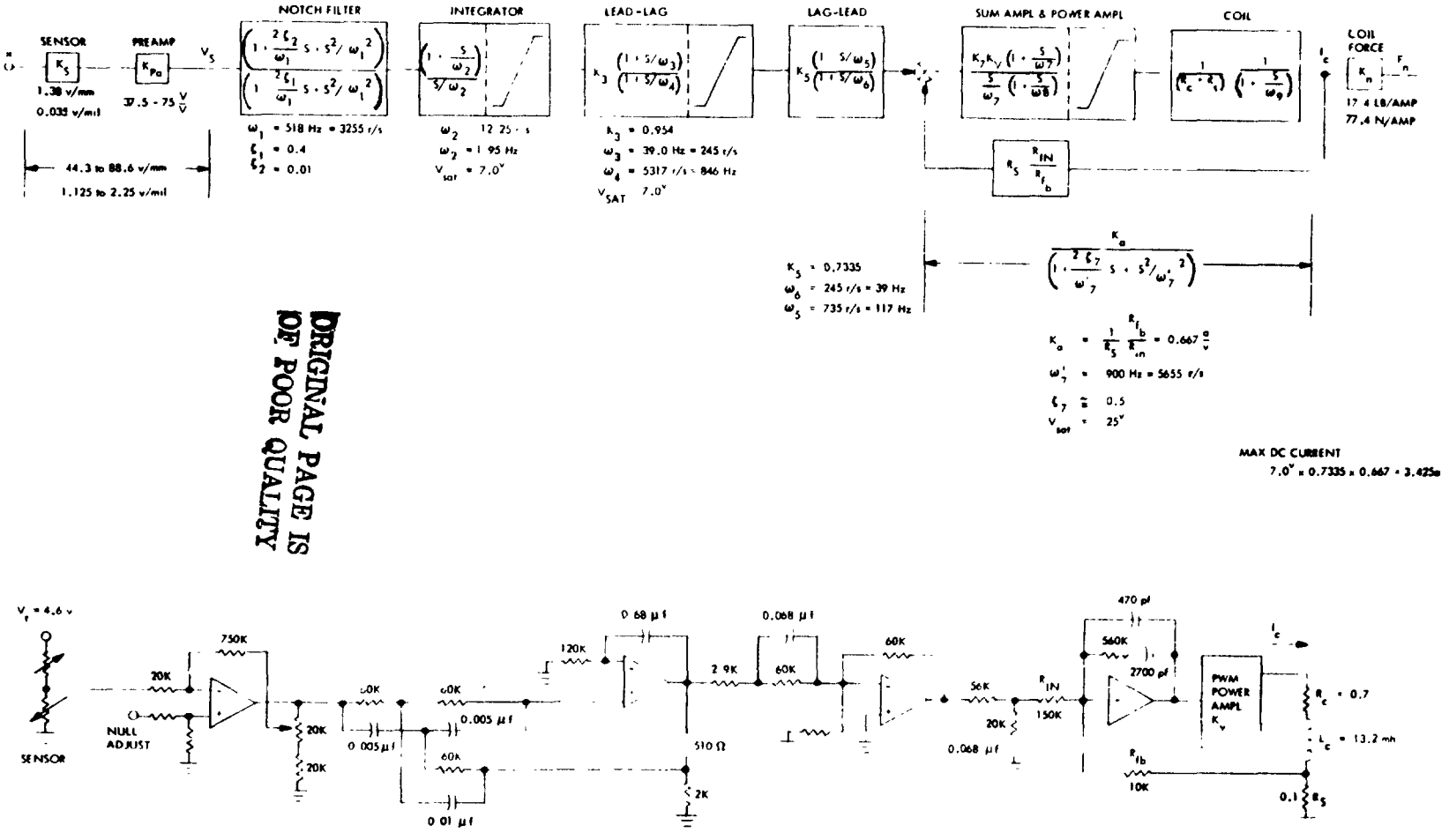

ORIGINAL PAGE IS
OF POOR QUALITY

Figure 4-3. Magnetic Bearing Electronics

4.1.3 PHASE/GAIN RESPONSE PROGRAM

Appendix A lists a special computer program to compute the basic open loop responses of the servo. The electronics values are those of Figure 4-3. The response ratios calculated, with K_n being a function of frequency, are:

a. K_n/K_p

b. $K_n/K_p - 1$

c. $\frac{K_n}{K_p}\frac{d}{d'} - 1$

These responses can then be combined with the mass and inertia characteristics to obtain the desired open loop response of the complete servo.

4.1.4 EXAMPLE RUNS

Example runs were made for these values:

a. Notch filter $\omega_1 = 3250$ r/s
$\zeta_1 = 0.40$
$\zeta_2 = 0.01$

b. Integrator - either none $\omega_2 = 0.00001$ r/s
or $\omega_2 = 15$ r/s

c. Lead-Lag $\omega_5 = 735$ r/s
$\omega_4 = 5880$ r/s

d. Power Ampl. $\omega'_7 = 6280$ r/s
$\zeta_7 = \zeta = 0.5$

The following values of $(K_n/K_n)_{midband}$ were used:

$$\left(\frac{K_n}{K_p}\right)_{mid} = 2,\ 2.5,\ 3$$

Table 4-1 gives the computer printout for four conditions. The inputs, as defined in Figure 4-3, are listed for each case.

Figures 4-4, 4-5 and 4-6 give gain plots, both open and closed loop. Figure 4-7 shows the Nichols chart used to obtain the closed loop response from the open loop values.

4.2 MAGNETIC BEARING SIMULATION STUDIES

In parallel with development tests of the magnetically suspended momentum wheel, an analytical simulation of the magnetic bearing system, using a digital computer, was prepared and limited test runs made. The simulation was limited to a rigid body model with the main objective of investigating:

a. Limit cycle (stop-to-stop) conditions

b. High-speed stability conditions (nutation damping)

Some minor variations exist between the characteristics of the bearing and electronics employed for the model and the actual values of the engineering model hardware, but they are not of a nature to change the basic simulation results.

The basic bearing simulation used is shown in Figure 4-8. The dynamics are simulated in terms of the translation and rotation of the center of mass of the suspended parts. The displacements at three locations along each end of the shaft are calculated: the center of the bearing, the position sensor location, and the stops location. Base motion is introduced as a rate at the center of mass. The behavior of the stops was simulated by re-defining the velocity at the stop and reflecting this back as a re-definition of the motion of the center of mass. The velocity leaving the stop was made a percentage of the velocity entering the stop, thus representing the loss of energy in rebounding. The passive non-restoring force of the magnetic bearing is represented as a positive feedback force.

TABLE 4-1

EXAMPLE RUNS

NOTCH FILTER - WITHOUT INTEGRATOR

$\frac{K_n}{K_p}$ ω_1 ζ_1 ζ_2 ω_2 ω_5 ω_4 $\zeta_7 = 0.5$ ω'_7

2.00 3250.00 0.40 0.01 0.00001 735.00 5880.00 628.00

Freq. R/S	K_n/K_p Gain	K_n/K_p ϕ	$K_n/K_p - 1$ Gain	$K_n/K_p - 1$ ϕ	$\frac{K_n d}{K_p d'} - 1$ Gain	$\frac{K_n d}{K_p d'} - 1$ ϕ
1.0	2.000	0.04	1.000	0.09	0.310	0.19
1.5	2.000	0.06	1.000	0.13	0.310	0.28
2.0	2.000	0.09	1.000	0.18	0.310	0.38
3.0	2.000	0.13	1.000	0.27	0.310	0.57
4.5	2.000	0.20	1.000	0.40	0.310	0.86
7.0	2.000	0.31	1.000	0.63	0.310	1.33
10.0	2.000	0.45	1.000	0.90	0.310	1.91
15.0	2.000	0.67	1.000	1.35	0.310	2.86
20.0	2.000	0.90	1.000	1.81	0.310	3.82
30.0	2.001	1.35	1.002	2.71	0.312	5.73
45.0	2.003	2.03	1.004	4.06	0.315	8.59
70.0	2.008	3.15	1.011	6.27	0.321	13.00
100.0	2.017	4.48	1.023	8.96	0.333	18.02
150.0	2.039	6.63	1.052	12.94	0.361	25.27
200.0	2.070	8.68	1.092	16.64	0.397	31.04
300.0	2.153	12.38	1.196	22.71	0.484	38.68
450.0	2.329	16.69	1.401	28.53	0.636	43.53
700.0	2.715	20.39	1.812	31.47	0.910	42.86
1000.0	3.253	19.93	2.338	28.31	1.238	35.90
1500.0	4.099	10.90	3.123	14.38	1.713	17.24
2000.0	4.513	-5.73	3.520	-7.36	1.964	-8.65
3000.0	1.632	-54.11	1.323	-91.85	0.943	-113.29
4500.0	7.258	36.11	6.477	41.34	3.990	44.61
7000.0	9.760	-43.57	9.062	-47.93	5.710	-50.53
10000.0	6.003	-91.91	6.118	-101.31	4.089	-106.06
15000.0	2.780	-124.43	3.446	-138.28	2.525	-143.49
20000.0	1.572	-139.10	2.412	-154.80	1.902	-159.23
30000.0	0.700	-153.07	1.655	-168.95	1.424	-171.6
45000.0	0.311	-162.15	1.300	-175.78	1.195	-177.00
70000.0	0.128	-168.55	1.126	-178.70	1.082	-179.11
100000.0	0.063	-171.99	1.062	-179.52	1.040	-179.65
2975.0	2.066	-51.10	1.635	-79.50	1.064	-98.09
3087.5	1.096	-55.71	0.983	-112.66	0.840	-135.09
3250.0	0.221	13.07	0.786	176.34	0.859	177.81
3412.5	1.141	81.54	1.402	126.39	1.157	140.27
3575.0	2.241	77.57	2.249	103.31	1.588	115.51

TABLE 4-1 (cont'd)

EXAMPLE RUNS

INTEGRATOR

$\zeta_7 = 0.5$

$\frac{K_n}{K_p}$	ω_1	ζ_1	ζ_2	ω_2	ω_5	ω_4	ω'_7
2.00	3250.00	0.40	0.01	15.00	735.00	5880.00	62[illegible]

Freq.	K_n/K_p		$K_n/K_p - 1$		$\frac{K_n}{K_p}\frac{d}{d'} - 1$	
R/S	Gain	ϕ	Gain	ϕ	Gain	ϕ
1.0	20.066	-26.14	30.015	-88.04	19.651	-89.[illegible]5
1.5	20.099	-84.22	20.023	-87.06	13.102	-[illegible]5.57
2.0	15.132	-82.31	15.031	-86.09	9.828	-86.10
3.0	10.198	-76.55	10.047	-84.15	6.555	-87.[illegible]5
4.5	6.960	-73.09	6.737	-81.26	4.374	-85.73
7.0	4.729	-64.66	4.395	-76.53	2.818	-83.36
10.0	3.605	-55.85	3.155	-71.06	1.981	-80.[illegible]4
15.0	2.828	-44.32	2.226	-62.61	1.334	-75.87
20.0	2.500	-35.96	1.790	-55.11	1.015	-71.28
30.0	2.237	-25.20	1.399	-42.92	0.704	-62.[illegible]0
45.0	2.111	-16.39	1.186	-30.16	0.509	-50.[illegible]5
70.0	2.054	-8.93	1.077	-17.22	0.390	-32.[illegible]1
100.0	2.040	-4.04	1.045	-7.91	0.346	-15.[illegible]0
150.0	2.049	0.92	1.050	1.81	0.343	3.[illegible]3
200.0	2.075	4.40	1.081	8.46	0.370	16.[illegible]4
300.0	2.156	9.52	1.181	17.57	0.457	30.[illegible]4
450.0	2.330	14.78	1.387	25.39	0.615	39.[illegible]0
700.0	2.716	19.16	1.801	29.66	0.896	40.63
1000.0	3.253	19.07	2.331	27.12	1.230	34.47
1500.0	4.099	10.33	3.120	13.62	1.710	16.35
2000.0	4.513	-6.16	3.521	-7.91	1.965	-9.29
3000.0	1.632	-54.39	1.328	-92.13	0.947	-113.46
4500.0	7.258	35.92	6.475	41.12	3.987	44.38
7000.0	9.760	-43.69	9.064	-48.06	5.712	-50.64
10000.0	6.003	-92.00	6.120	-101.39	4.091	-106.14
15000.0	2.780	-124.49	3.447	-136.32	2.526	-143.53
20000.0	1.572	-139.14	2.419	-154.83	1.902	-159.25
30000.0	0.700	-153.10	1.655	-168.96	1.424	-171.62
45000.0	0.311	-162.16	1.300	-175.79	1.195	-177.[illegible]0
70000.0	0.128	-168.56	1.126	-178.70	1.082	-179.11
100000.0	0.063	-172.00	1.062	-179.52	1.040	-179.68
2925.0	2.066	-51.39	1.641	-79.83	1.069	-98.35
3087.5	1.096	-55.99	0.988	-113.32	0.844	-135.12
3250.0	0.221	12.80	0.785	176.42	0.559	177.85
3412.5	1.141	81.29	1.309	126.24	1.154	140.19
3575.0	2.241	77.33	2.245	103.09	1.584	115.33
50.0	2.092	-14.43	1.151	-26.94	0.473	-46.22
500.0	2.399	16.06	1.465	26.94	0.670	40.42
5000.0	8.886	16.49	7.932	18.54	4.869	19.83

TABLE 4-1 (cont'd)

EXAMPLE RUNS

LEAD-LAG - WITHOUT INTEGRATOR

$\frac{K_n}{K_p}$	ω_1	ζ_1	ζ_2	ω_2	ω_5	ω_4	$\zeta_7 = 0.5$ ω'_7
2.50	3250.00	0.40	0.01	0.00001	735.00	5880.00	628...

Freq.	K_n/K_p		$K_n/K_p - 1$		$\frac{K_{n\,d}}{K_p d'} - 1$	
R/S	Gain	ϕ	Gain	ϕ	Gain	ϕ
1.0	2.500	0.04	1.500	0.07	0.637	0.11
1.5	2.500	0.06	1.500	0.11	0.637	0.17
2.0	2.500	0.09	1.500	0.15	0.637	0.23
3.0	2.500	0.13	1.500	0.22	0.637	0.34
4.5	2.500	0.20	1.500	0.33	0.637	0.52
7.0	2.500	0.31	1.500	0.52	0.637	0.81
10.0	2.500	0.45	1.500	0.75	0.637	1.16
15.0	2.500	0.67	1.500	1.13	0.638	1.74
20.0	2.500	0.90	1.501	1.50	0.638	2.32
30.0	2.502	1.35	1.502	2.26	0.639	3.48
45.0	2.504	2.03	1.505	3.38	0.642	5.20
70.0	2.510	3.15	1.513	5.24	0.648	8.02
100.0	2.522	4.48	1.527	7.41	0.659	11.29
150.0	2.549	6.63	1.560	10.88	0.686	16.35
200.0	2.587	8.68	1.606	14.08	0.722	20.76
300.0	2.692	12.38	1.725	19.51	0.815	27.64
450.0	2.911	16.69	1.974	25.06	0.991	33.53
700.0	3.394	20.39	2.481	28.46	1.322	35.54
1000.0	4.066	19.93	3.144	26.15	1.756	31.12
1500.0	5.124	10.90	4.146	13.52	2.381	15.46
2000.0	5.642	-5.73	4.648	-6.96	2.702	-7.85
3000.0	2.040	-54.11	1.664	-83.22	1.104	-101.30
4500.0	9.072	36.11	8.285	40.19	5.168	42.66
7000.0	12.201	-43.57	11.497	-47.01	7.299	-48.99
10000.0	7.504	-91.91	7.603	-99.46	5.048	-103.33
15000.0	3.476	-124.43	4.124	-135.97	2.959	-140.61
20000.0	1.965	-139.10	2.799	-152.62	2.145	-156.86
30000.0	0.875	-153.07	1.824	-167.44	1.533	-170.25
45000.0	0.389	-162.15	1.375	-175.02	1.245	-176.40
70000.0	0.160	-168.55	1.158	-178.41	1.103	-178.91
100000.0	0.078	-171.99	1.078	-179.41	1.051	-179.60
2925.0	2.583	-51.10	2.104	-72.80	1.318	-87.27
3087.5	1.371	-55.71	1.155	-101.36	0.891	-123.68
3250.0	0.276	13.07	0.733	175.10	0.824	177.15
3412.5	1.428	81.54	1.617	119.24	1.264	133.01
3575.0	2.801	77.57	2.764	98.26	1.891	108.66

TABLE 4-1 (cont'd)

EXAMPLE RUNS

POWER AMPLIFIER - WITHOUT INTEGRATOR

$\zeta_7 = 0.5$

$\frac{K_n}{K_p}$	ω_1	ζ_1	ζ_2	ω_2	ω_5	ω_4	ω'_7
3.00	3250.00	0.40	0.01	0.00001	725.00	5850.00	2[illegible]

Freq.	K_n/K_p		$K_n/K_p - 1$		$\frac{K_n d}{K_p d'} - 1$	
R/S	Gain	ϕ	Gain	ϕ	Gain	ϕ
1.0	3.000	0.04	2.000	0.06	0.965	0.09
1.5	3.000	0.06	2.000	0.10	0.965	0.13
2.0	3.000	0.09	2.000	0.13	0.965	0.17
3.0	3.000	0.13	2.000	0.20	0.965	0.27
4.5	3.000	0.20	2.000	0.30	0.965	0.41
7.0	3.000	0.31	2.000	0.47	0.965	0.64
10.0	3.000	0.45	2.000	0.67	0.965	0.92
15.0	3.000	0.67	2.000	1.01	0.965	1.39
20.0	3.001	0.90	2.001	1.35	0.965	1.84
30.0	3.002	1.35	2.002	2.03	0.967	2.75
45.0	3.005	2.02	2.006	3.04	0.969	4.13
70.0	3.013	3.15	2.015	4.72	0.976	6.38
100.0	3.026	4.48	2.031	6.69	0.988	9.02
150.0	3.059	6.63	2.069	9.83	1.017	13.16
200.0	3.105	8.68	2.121	12.77	1.056	16.91
300.0	3.230	12.58	2.264	17.82	1.159	23.05
450.0	3.494	16.69	2.552	23.16	1.361	28.88
700.0	4.073	20.39	3.155	26.73	1.765	31.77
1000.0	4.979	19.93	3.954	24.87	2.281	28.52
1500.0	6.148	10.90	5.170	13.00	3.051	14.[illegible]
2000.0	6.770	-5.73	5.776	-6.72	3.441	-7.46
3000.0	2.448	-54.11	2.031	-77.61	1.300	-92.62
4500.0	10.[illegible]	36.11	10.096	39.46	6.350	41.44
7000.0	14.641	-43.57	13.933	-46.41	8.592	-48.02
10000.0	9.004	-91.91	9.093	-98.22	6.015	-102.[illegible]
15000.0	4.171	-124.43	4.808	-134.31	3.399	-138.47
20000.0	2.359	-139.10	3.192	-150.97	2.392	-154.95
30000.0	1.050	-153.07	1.994	-166.20	1.643	-169.07
45000.0	0.467	-162.15	1.451	-174.33	1.294	-175.84
70000.0	0.193	-169.55	1.189	-178.15	1.124	-176.72
100000.0	0.094	-171.99	1.093	-179.30	1.061	-179.52
2925.0	3.100	-51.10	2.592	-68.57	1.604	-80.12
3037.5	1.645	-85.71	1.341	-93.08	0.973	-113.21
3250.0	0.331	13.07	0.680	173.67	0.729	176.43
3412.5	1.712	81.54	1.851	113.83	1.388	126.97
3575.0	3.361	77.67	3.294	94.81	2.213	1[illegible]

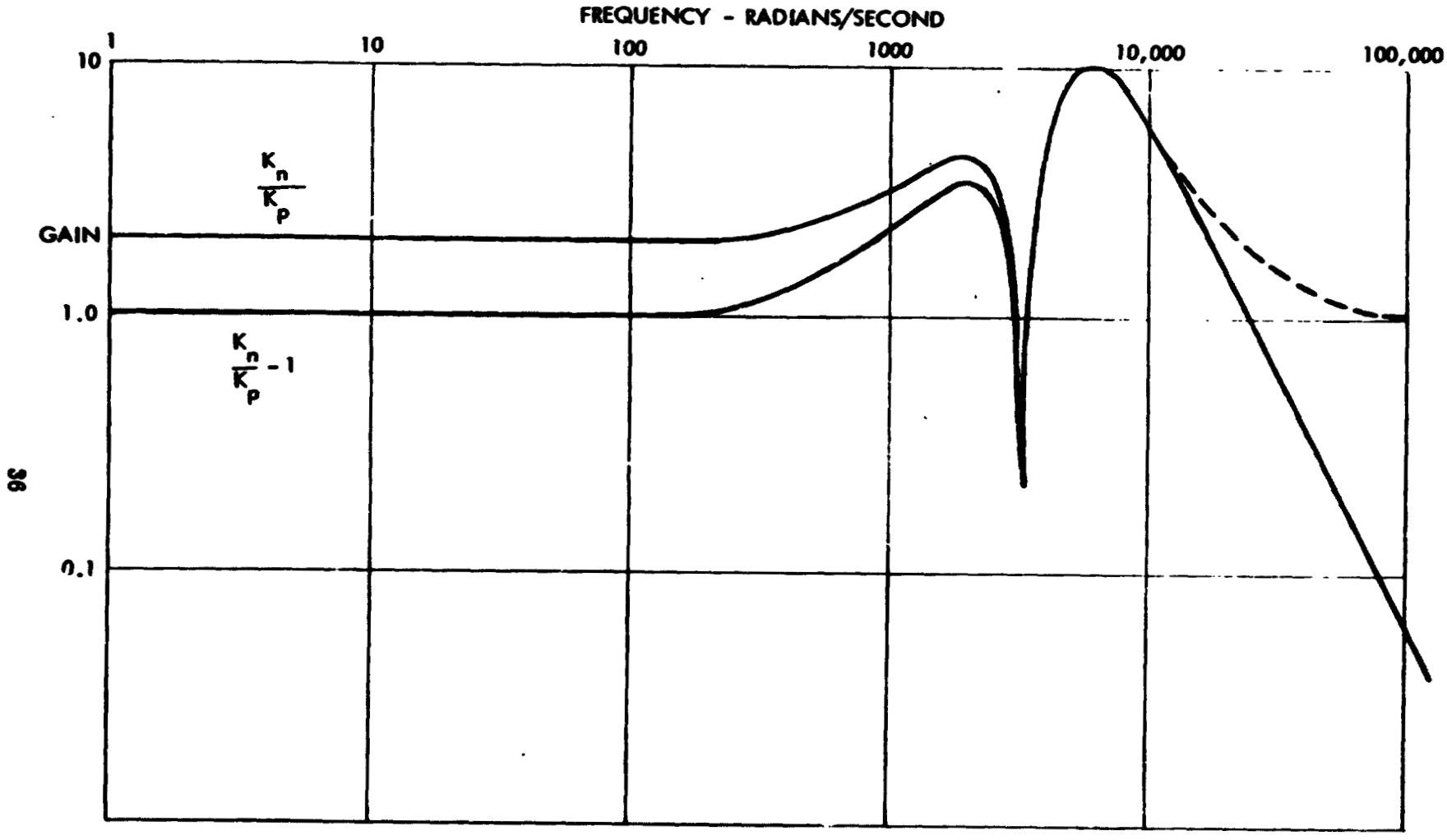

Figure 4-4. $\frac{K_n}{K_p}$ and $\frac{K_n}{K_p} - 1$ for Gain = 2

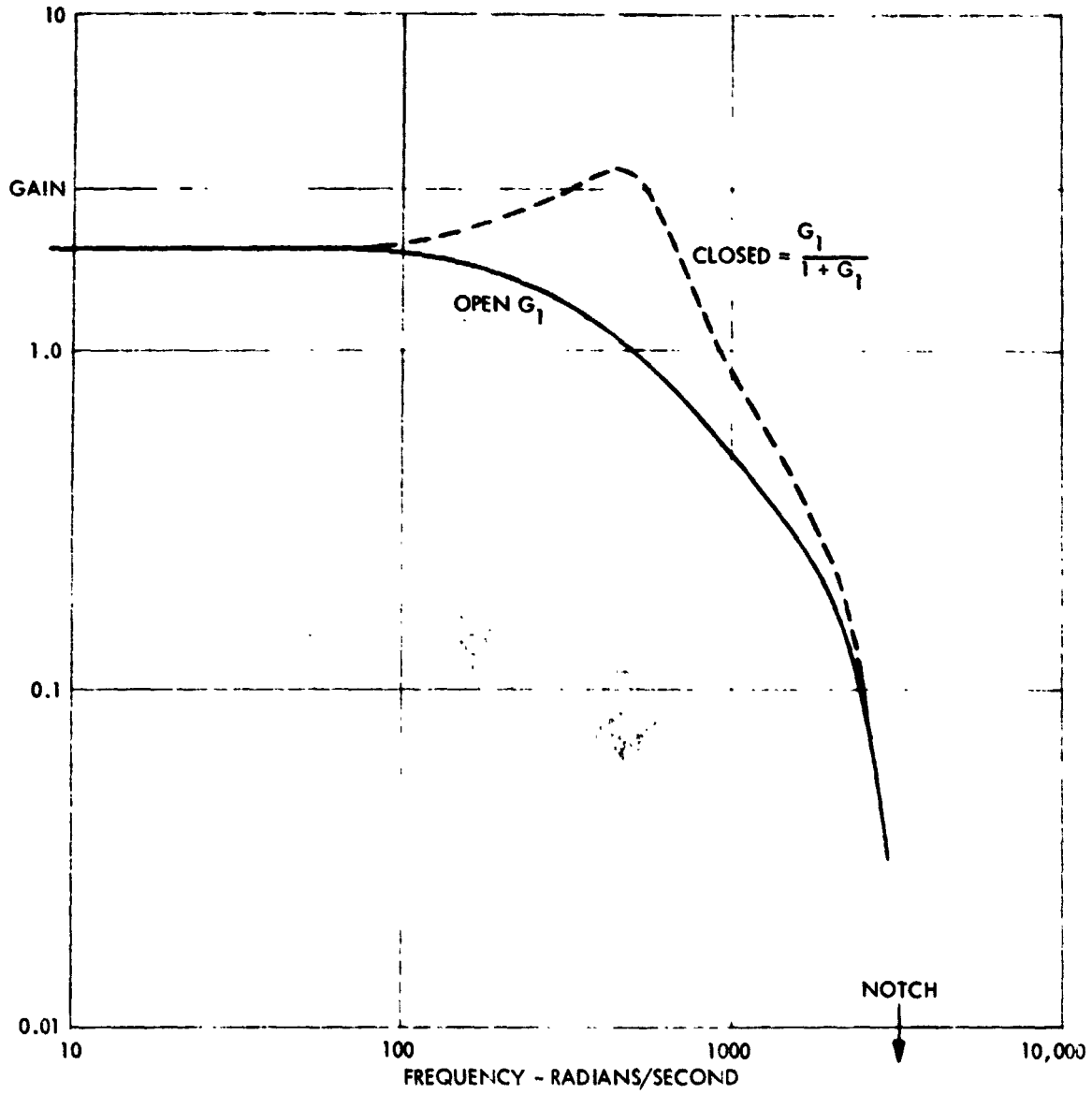

Figure 4-5. G_1 and $\frac{G_1}{1+G_1}$ Gains

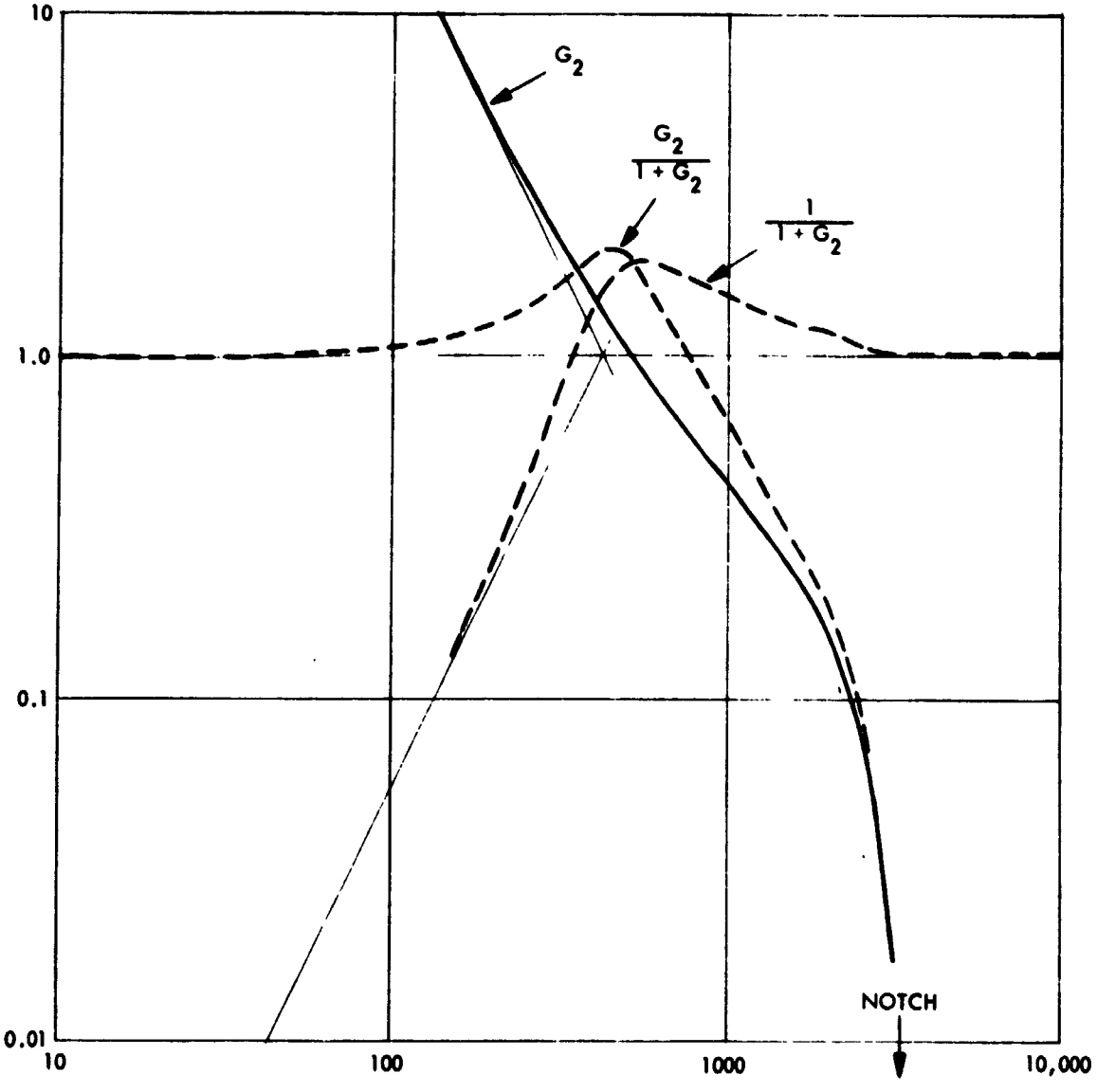

Figure 4-6. G_2 and $\frac{G_2}{1+G_2}$ and $\frac{1}{1+G_2}$ Gains

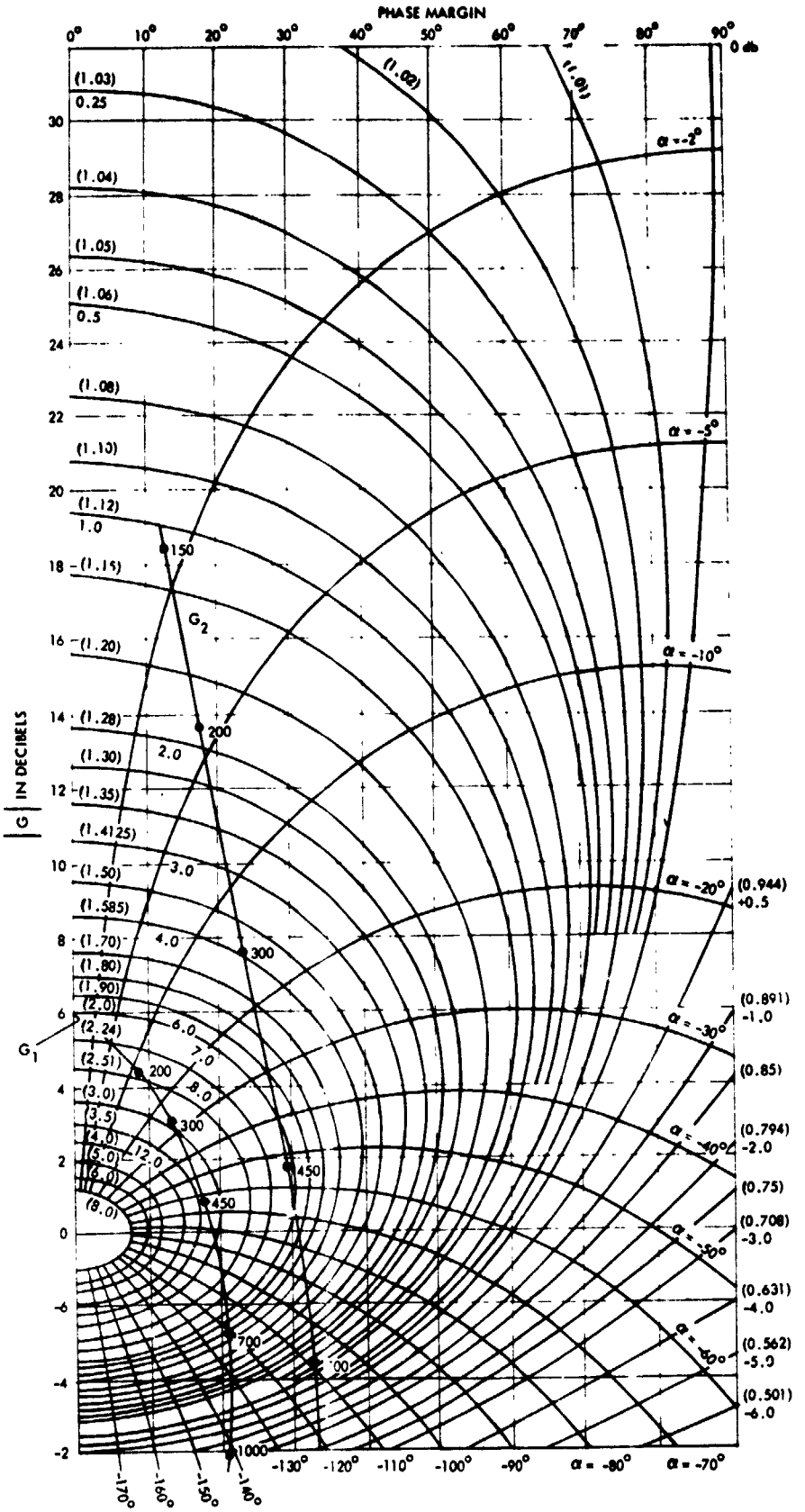

Figure 4-7. G_1 and G_2 (Translation) Open and Closed Loop for $\frac{K_n}{K_p} = 2$

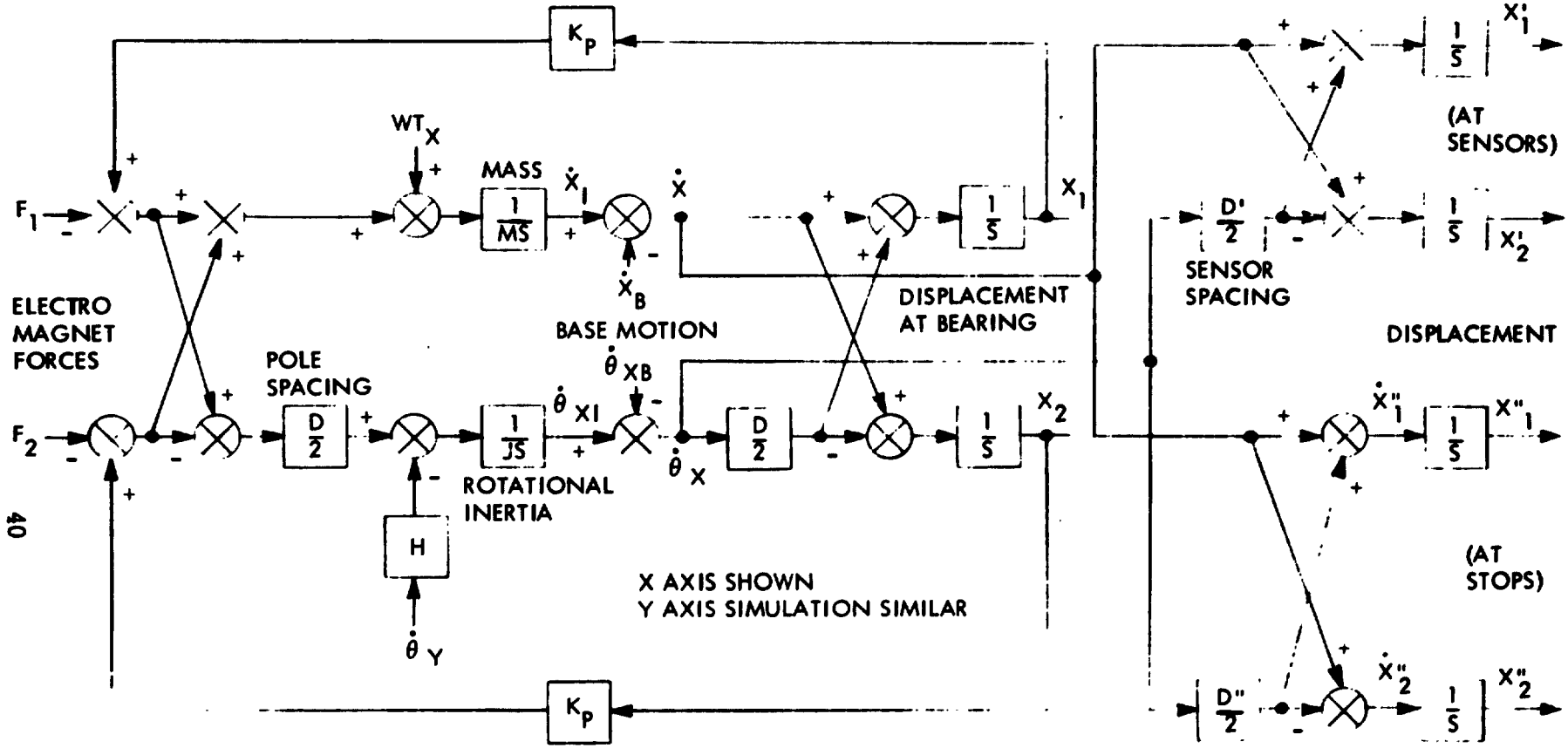

K_P	=	700,507	N/m	48,000 LB/FT	NON-REST. FORCE GRADIENT
D/2	=	0.1143	m	= 4.5/12 FT	LOCATION OF BEARING/cg
D'/2	=	0.07366	m	= 2.9/12 FT	LOCATION OF SENSOR/cg
D"/2	=	0.16256	m	= 6.4/4 FT	LOCATION OF STOPS/cg
M	=	8.173	kg	= 0.56 LB-SEC^2/FT	SUSPENDED MASS
J	=	0.08135	N-m-s^2	= 0.06 FT-LB-SEC^2	POLAR MOMENT OF INERTIA
H	=	101.69	N-m-s	= 75 FT-LB-SEC	ANGULAR MOMENTUM

WHEN IN STOPS, REDEFINE: $\dot{X}_1 = \frac{\dot{X}''_1 + \dot{X}''_2}{2} + \dot{X}_B$

$$\dot{\theta}_{X_1} = \frac{\dot{X}''_1 - \dot{X}''_2}{D''} + \dot{\theta}_{X_B}$$

Figure 4-8. Magnetic Bearing Simulation

The position sensor, electronics, and electromagnetic simulation is shown in Figure 4-9. The top of the figure is a block diagram while the bottom represents the layout of the simulation. Note that the diagram describes one axis of one bearing and three other similar channels were used to complete the simulation. The loop gain was set by the preamplifier to give a dc gain of 1.75×10^6 N/m (10 pounds/mil) of displacement for each bearing if the integrators were disabled.

The notch filter simulation required that the damping of the numerator be finite for numerical stability reasons. The actual filter does have a finite depth to the notch also, due to component tolerances. The integrator saturation requires care in its simulation since the actual circuit does not charge the capacitor to higher values than the amplifier maximum value, yet a straightforward simulation would permit the storage element to take on very high values. The simulation diagram shows the technique used.

The current command limit limits the voltage command to the current control loop. The lag lead network following the limiter was a late addition to the simulation to duplicate the changes being tried in the development model. When it is used the lead lag is changed to increase the high frequency gain to compensate for the loss in the lag lead network. Thus the linear response remains the same while the behavior with limiting is improved.

The current control loop was simulated with gains and lags to give a quadratic response of 1000 Hz bandwidth. The voltage saturation of the power amplifier is simulated with a value typical of the bench test conditions. The electromagnet gain is represented as a conversion of current to pounds force per bearing.

The digital simulation program was of the CSMP-360 general type but was extensively modified for each of the runs of each of the various investigations. Many of the program elements were unique to the facility and the subprogram library used, and required engineering judgment during their use. For these reasons program details have not been included in this report.

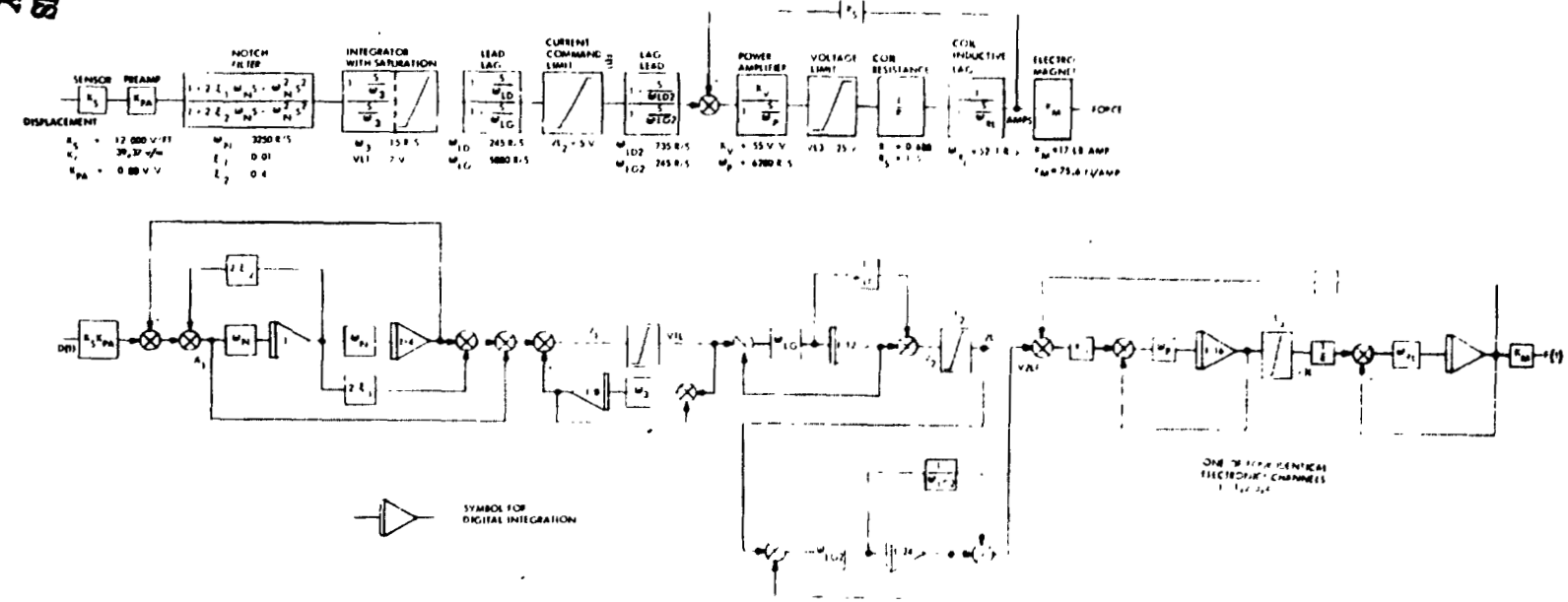

Figure 4-9. Magnetic Bearing Electronics Simulation

Figure 4-10 illustrates the response during the pickup period when the shaft is initially setting on the lower stops. The response is roughly quadratic, with a frequency of about 400 rad/sec and 0.25 damping. Figure 4-11 shows that 20 percent variations of gain affect frequency but not the damping of the response.

The response during pickup from the stops when one end of the shaft is up and the other is down is shown in Figure 4-12. Linear displacement at one stop is plotted as an indication of the angular motion which occurs. The angular response is of about the same frequency as the linear response but demonstrates about 0.4 damping.

The ability of the system to damp angular disturbances when the momentum wheel is spinning is shown in Figures 4-13 through 4-16. In each case the shaft was given an initial angular disturbance of 0.5 rad/sec in the X plane and the settling response plotted. The damping of the two nutation frequencies are shown to vary as a function of angular momentum of the wheel. For the nominal momentum value of 101.69 N-m-sec (75 ft-lb-sec) the approximate nutation frequencies were 94.25 and 1571 rad/sec (15 Hz and 250 Hz). Thus while the response is relatively lightly damped the settling time is short. Note that for values of H greater than about 122 N-m-sec (90 ft-lb-sec) the behavior becomes unstable.

Modeling the behavior of the system in the event the shaft should hit the stops while spinning is difficult. The friction of the stop would impart a side velocity in addition to its rebound velocity. No simulation of this effect was attempted. Figure 4-17 represents the response of angular pickup from the stops with an H of 101.69 N-m-sec (75 ft-lb-sec). Although it is doubtful if operation at that speed could be achieved while resting in the stops, it is somewhat indicative of the pickup behavior.

During early bench tests the bearing system exhibited a limit cycle of the order of 682 rad/sec (100 Hz) when the rotor was shocked into hitting the stops. Simulation runs were made in an attempt to duplicate the experimental results and test proposed modifications. It was found that the elasticity or energy absorption of the stops was a critical factor in the damping of the limit cycle as is, of course, the nonlinearity and frequency response of the servoloop.

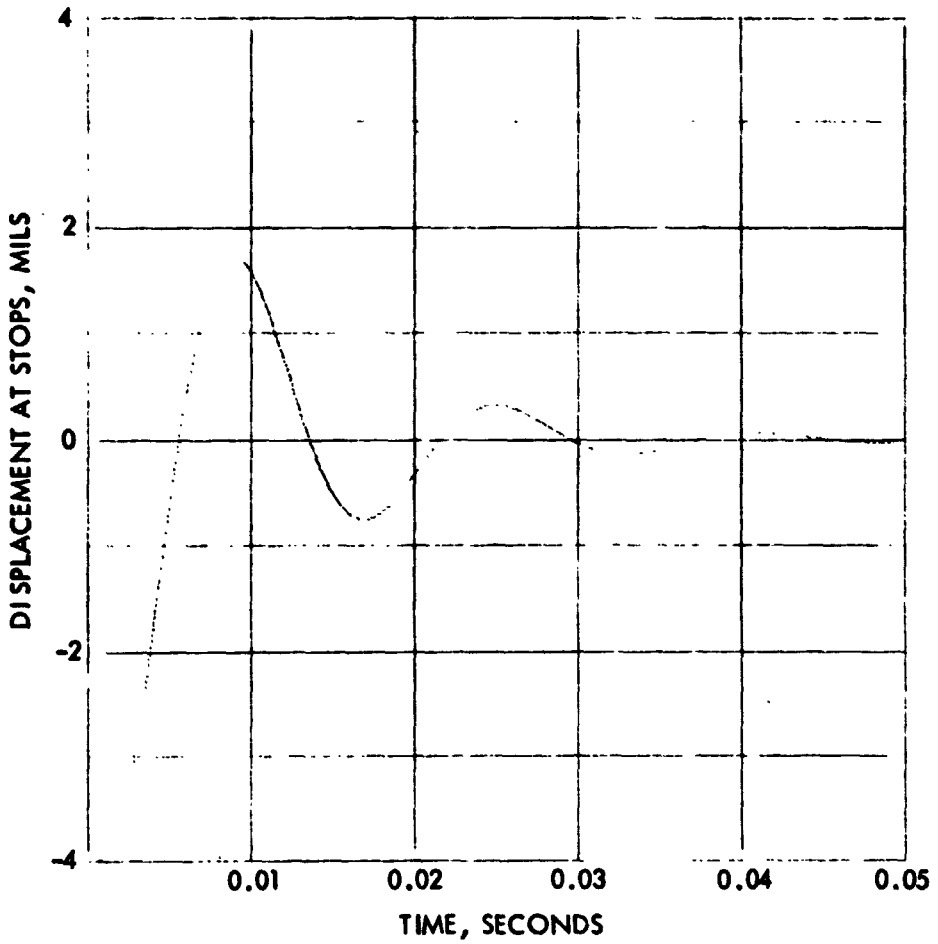

Figure 4-10. Translational Displacement During Pickup

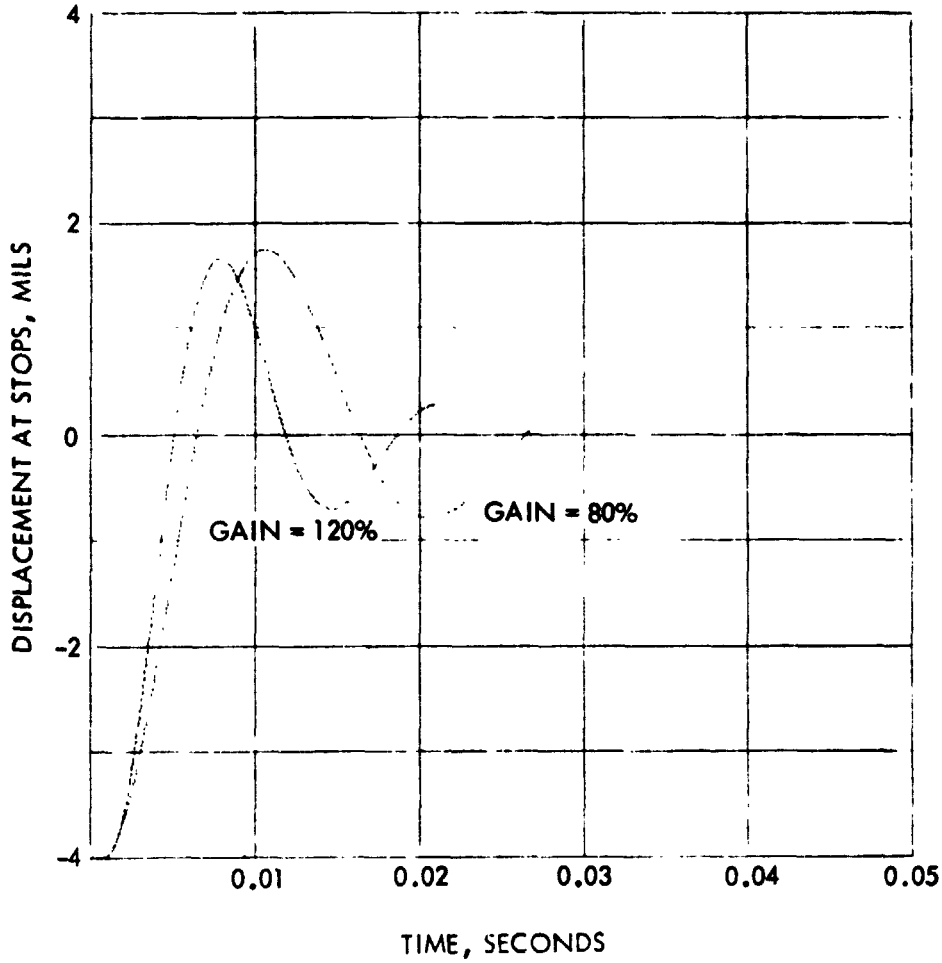

Figure 4-11. Translational Displacement with Gain Variations

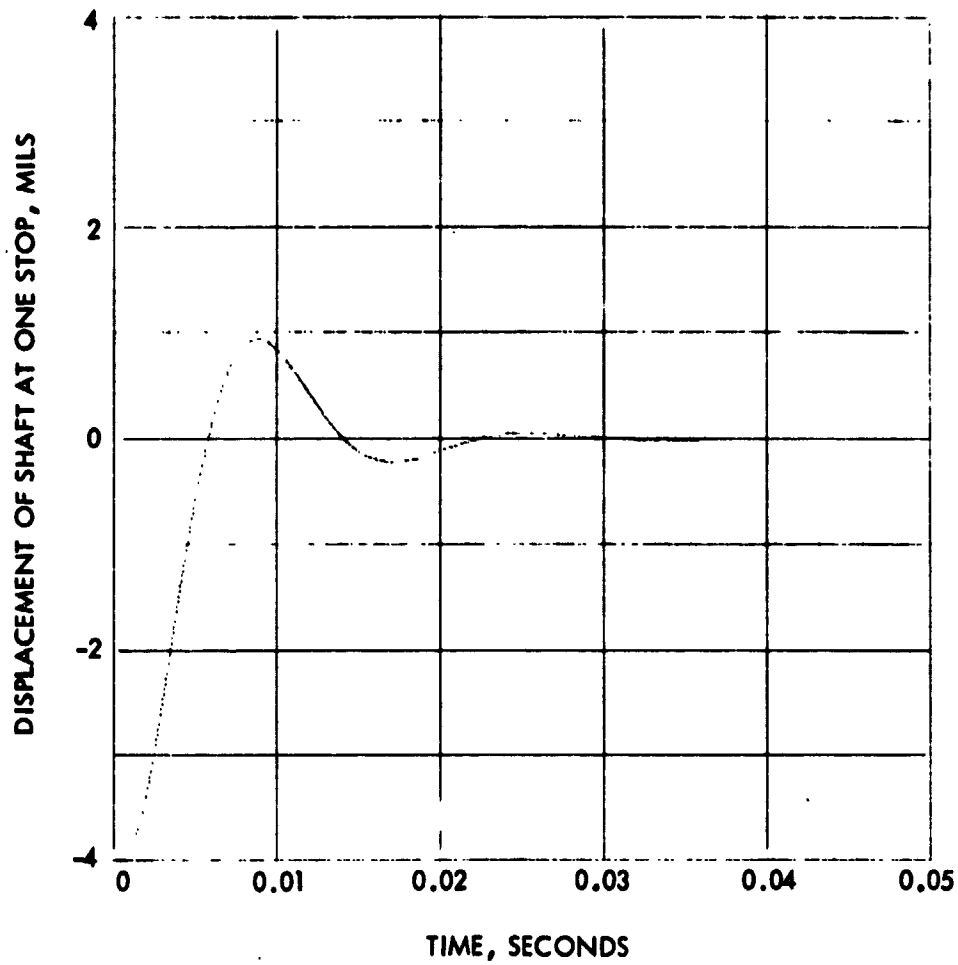

Figure 4-12. Angular Displacement During Pickup

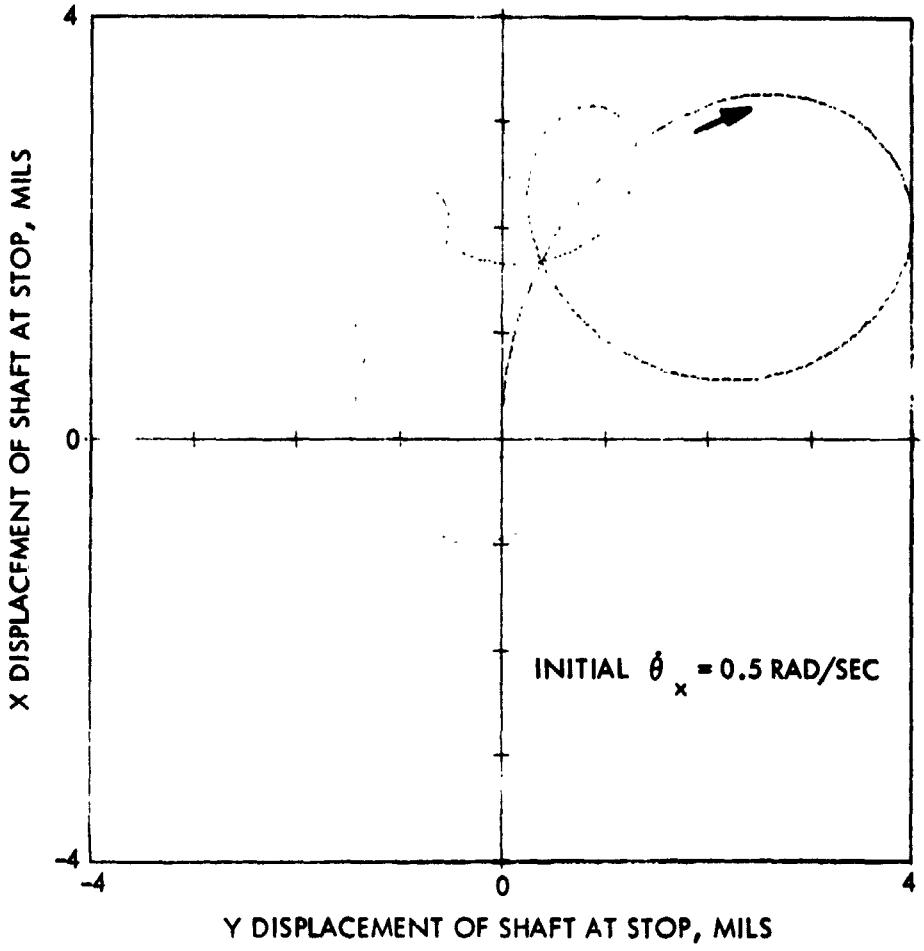

Figure 4-13. Polar Response, H = 67.79 N-m-sec (50 ft-lb-sec)

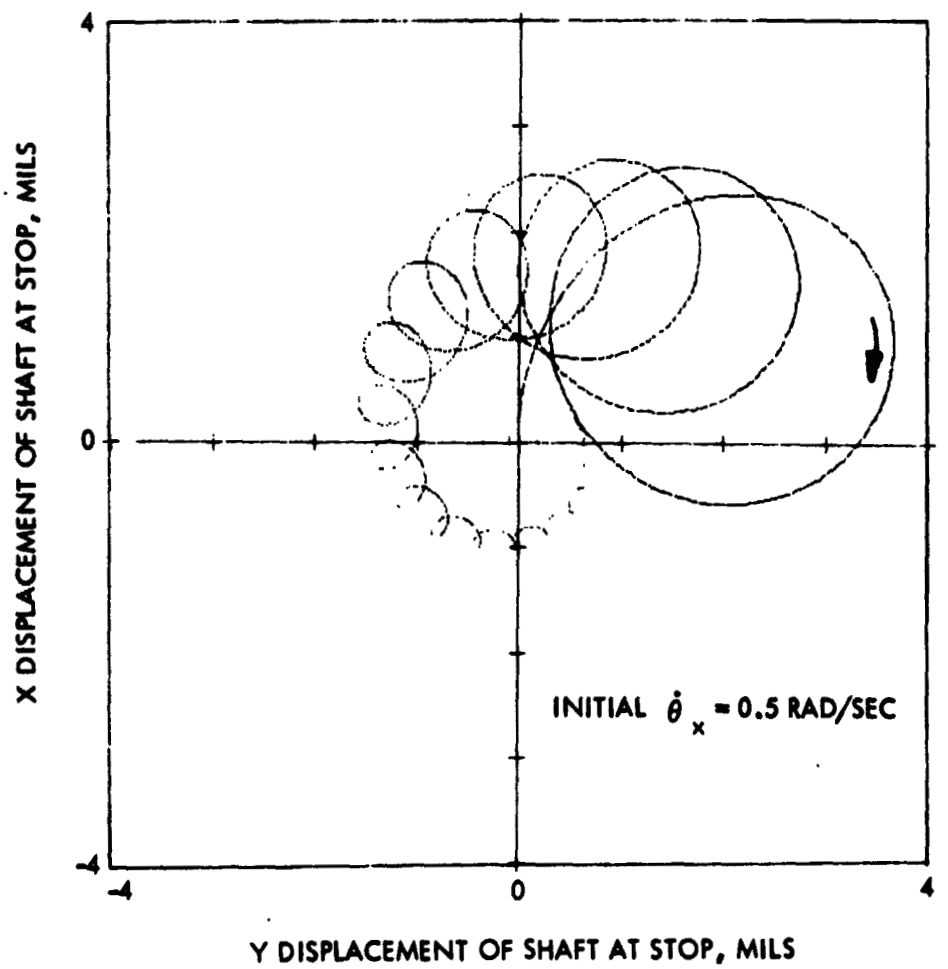

Figure 4-14. Polar Response, H = 10.169 N-m-sec (75 ft-lb-sec)

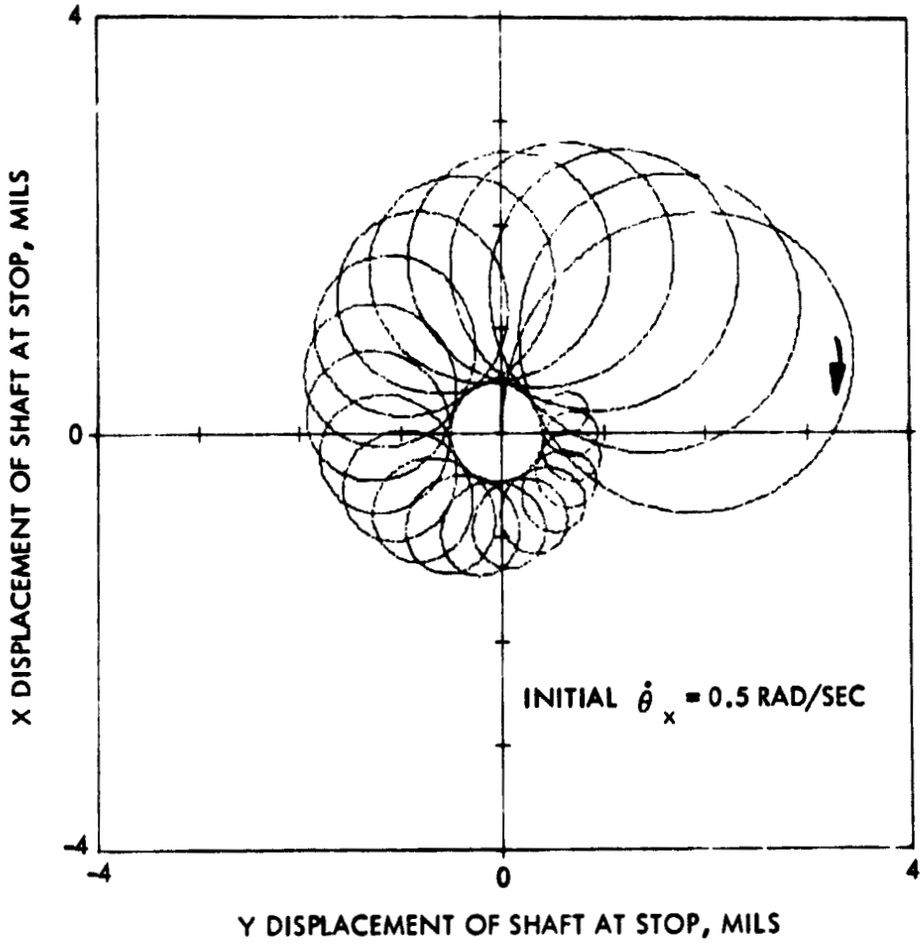

Figure 4-15. Polar Response, H = 115.24 N-m-sec (85 ft-lb-sec)

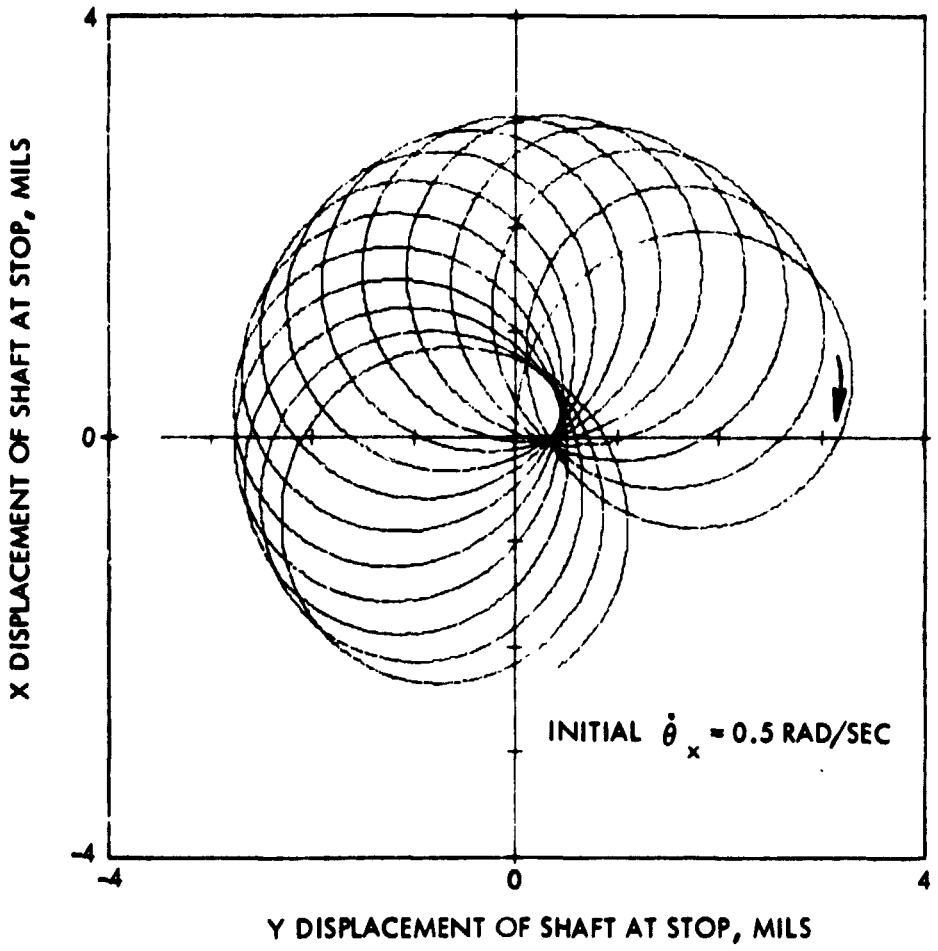

Figure 4-16. Polar Response, H = 125.4 N-m-sec (92.5 ft-lb-sec)

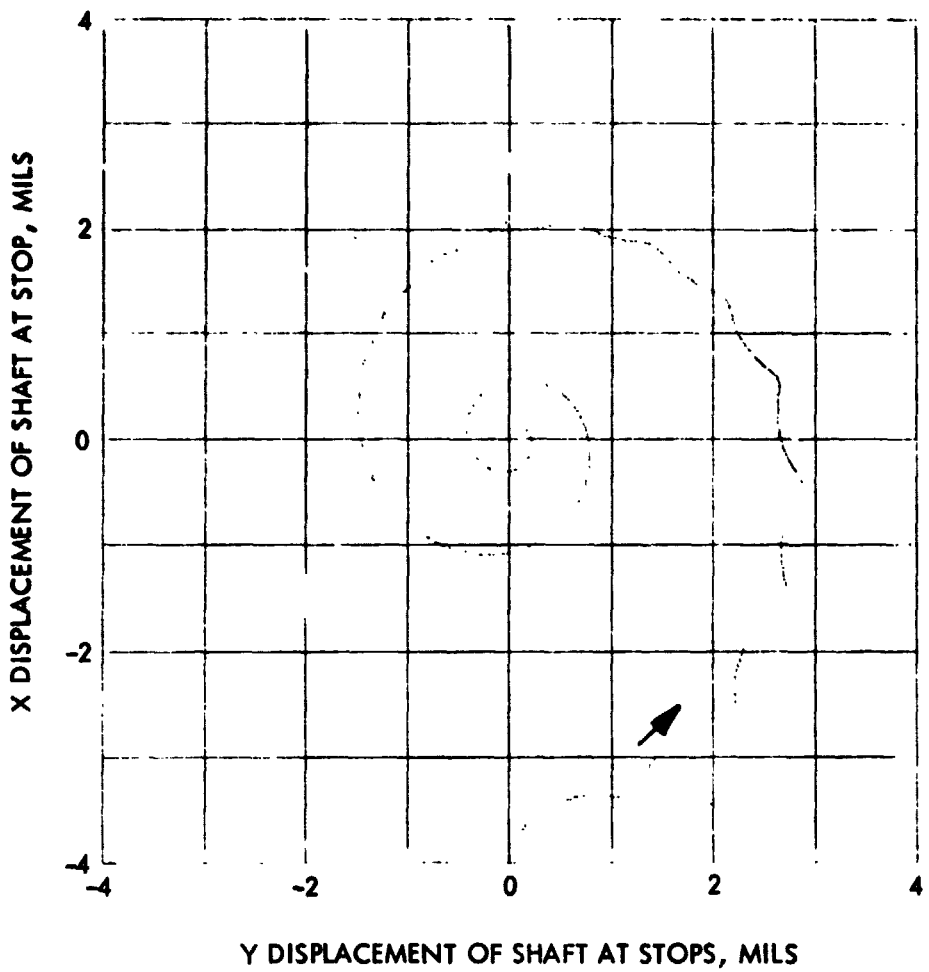

Figure 4-17. Angular Pickup from Stops, H = 101.69 N-m-sec (75 ft-lb-sec)

In each simulation test the suspended mass was given an initial velocity of 0.6096 m/sec (2 ft/sec). In the absence of any dissipation in the stops or bearing forces this would result in a 9425 rad/sec (1500 Hz) limit cycle which should be high enough to excite any possible control limit cycle. Figure 4-18 illustrates how the initial high frequency limit cycle slows down to a frequency at which the servo system can gain control. The less the dissipation in the stops the longer it seems to take to gain control. Figures 4-18 and 4-19 represent stops of 80 and 85 percent elasticity. While the 85 percent case may be slowly damping,a 90 percent case seemed to establish a stable limit cycle.

The ability of the servo system to regain control is a function of the linear range of the elements. For example, the current buildup in the electromagnet is limited by the available drive voltage. Figure 4-20 demonstrates the improved control possible if the drive voltage limit were raised to 75 volts. But Figure 4-21 shows that even the higher voltage limit will not stabilize the system with stop elasticities of 90 percent.

Figures 4-18 through 4-20 represent the responses of systems without the lag lead network previously described. By adding the lag lead network after the current command limiter the relation of gains and saturations was improved with the results shown in Figures 4-22, 4-23 and 4-24. Note that with the voltage limit at its normal 25 volts and the stop elasticity of 90 percent the system damps. With 95 percent stops the system still limit cycles.

In the absence of experimental evidence as to the dissipation characteristics of the stops the correlation of the simulation and the hardware cannot be verified, but the possibility of a limit cycle is confirmed.

Figure 4-25 is a run with the integrator active in the loop during an initial pickup from the stops. Since the first stages of the electronics are active prior to connecting the output circuits the integrator is fully saturated. This results in a signal wnich drives the bearing into its opposite limit stop and maintains it there until the integrator discharges at its relatively slow rate.

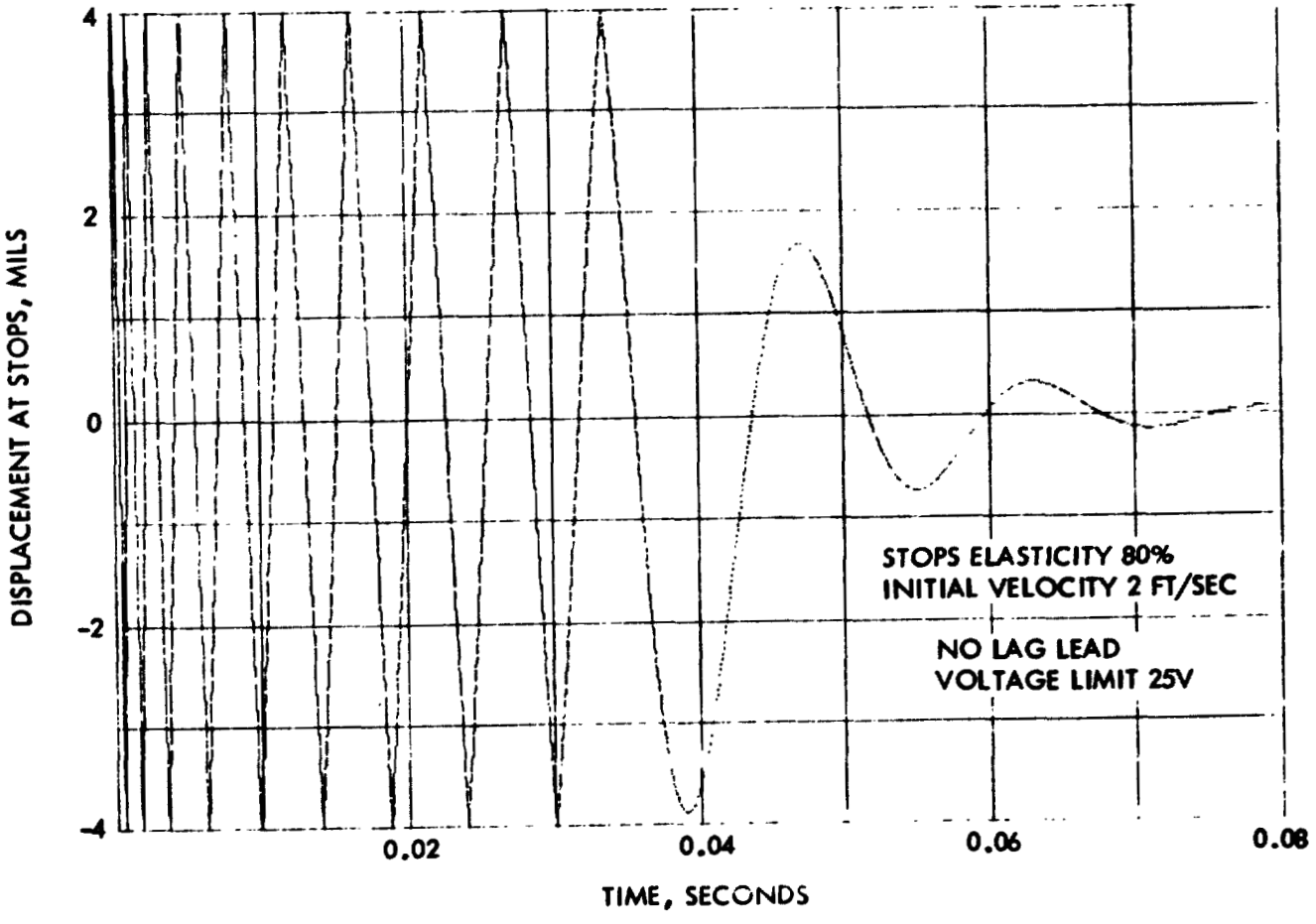

Figure 4-18. Limit Cycle Damping, 80 Percent Stops, No Lag Lead

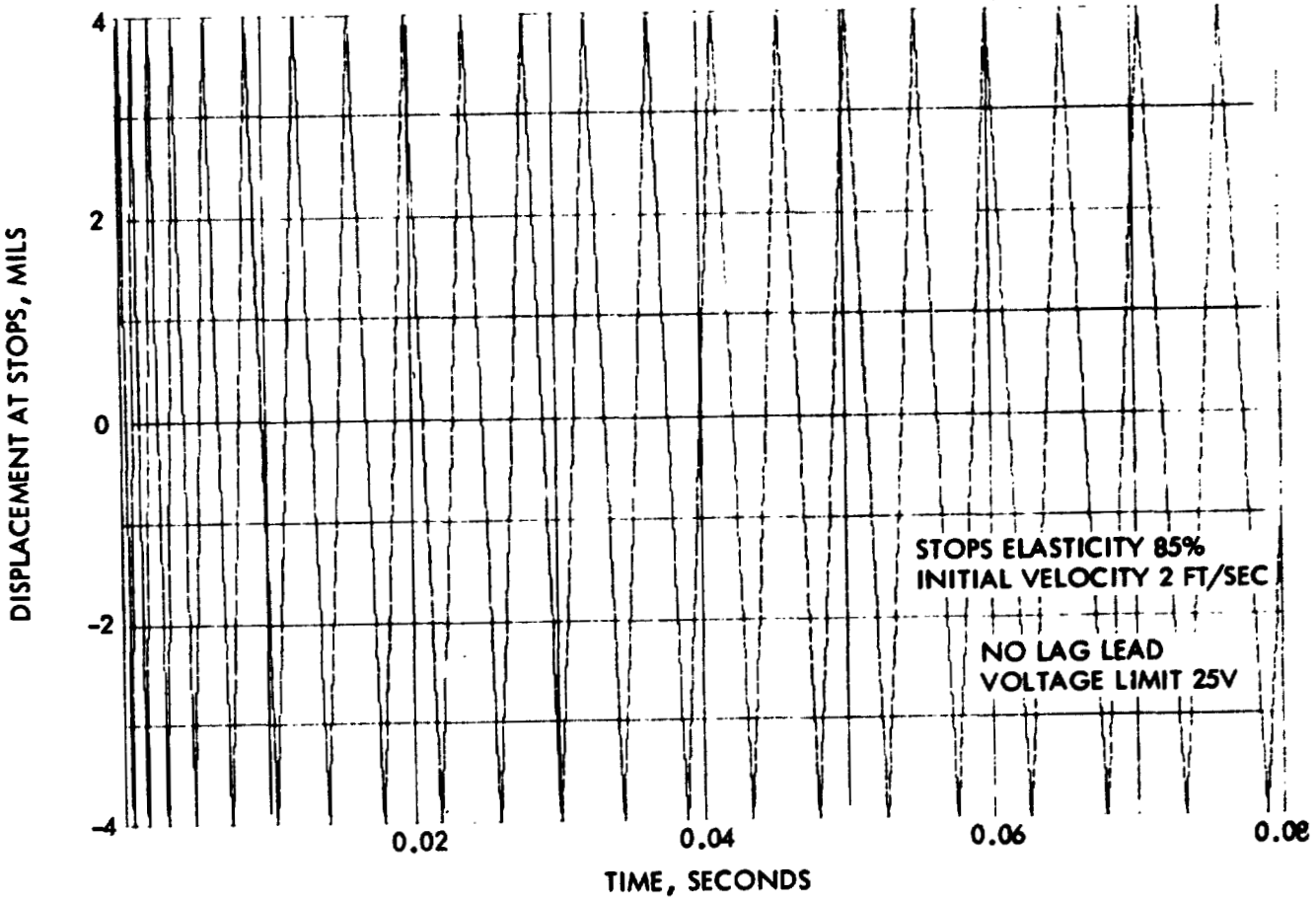

Figure 4-19. Limit Cycle Damping, 85 Percent Stops, No Lag Lead

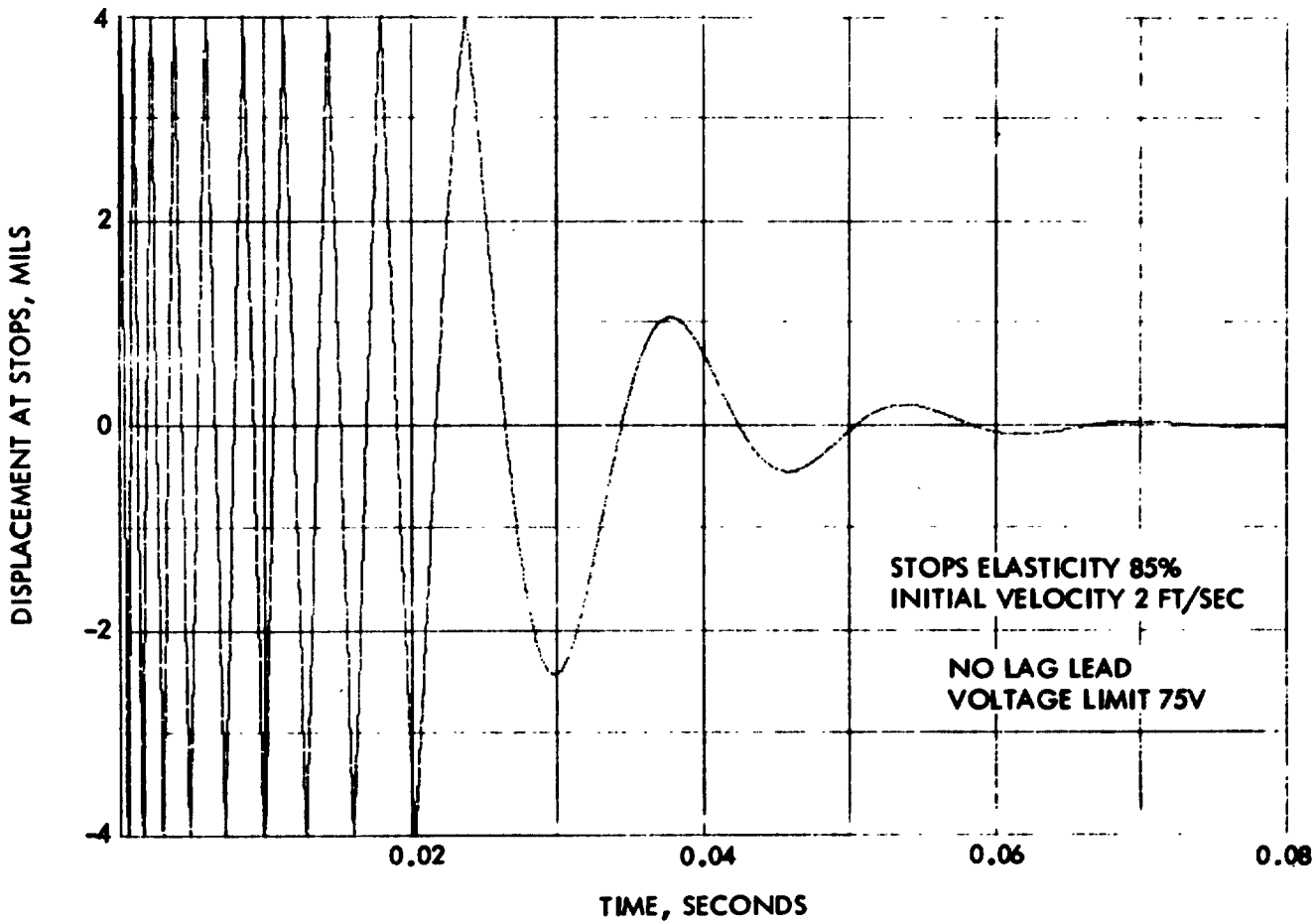

Figure 4-20. Limit Cycle Damping, 85 Percent Stops, No Lag Lead, 75 V Limit

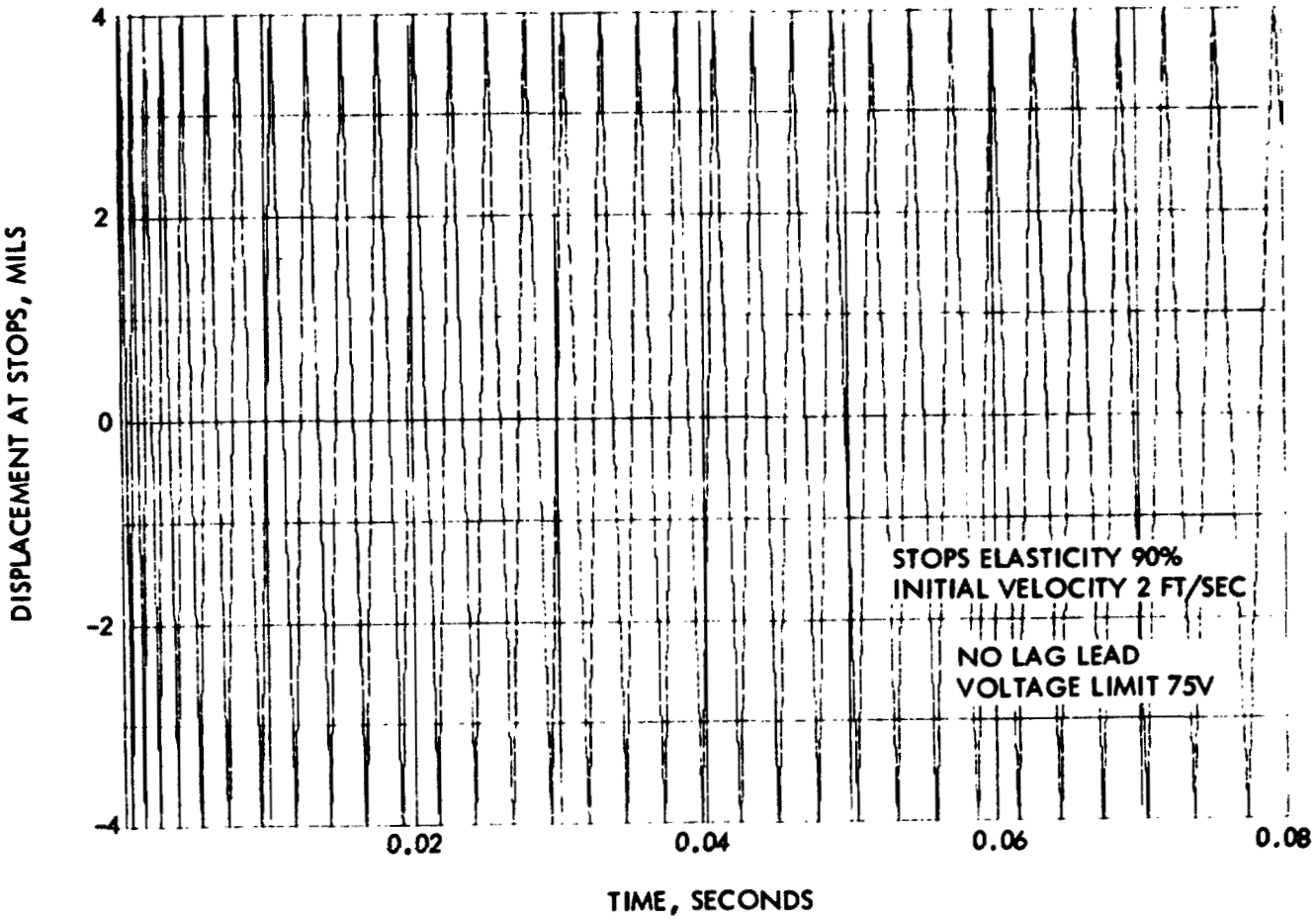

Figure 4-21. Limit Cycle Damping, 90 Percent Stops, No Lag Lead, 75 V Limit

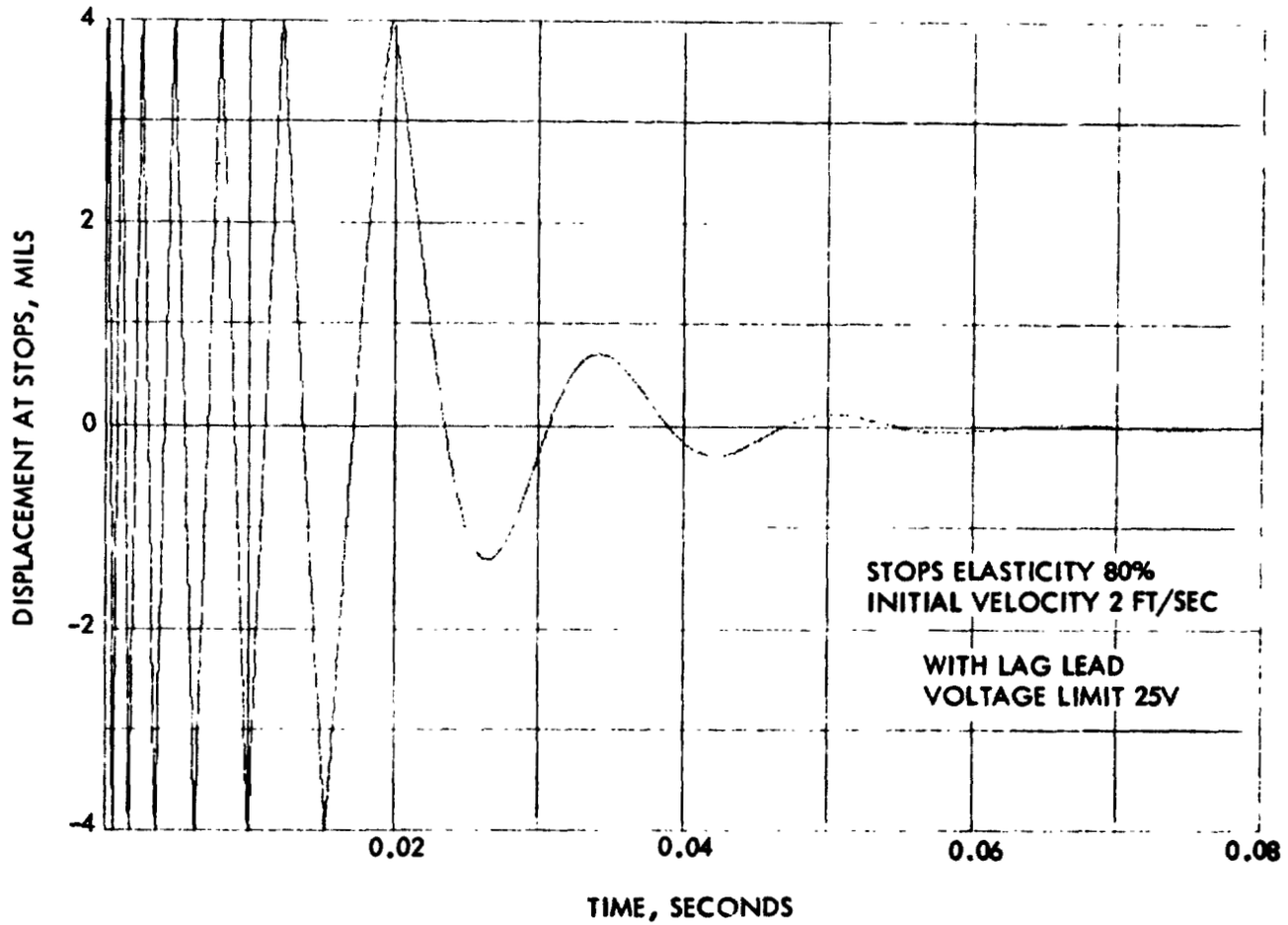

Figure 4-22. Limit Cycle Damping, 80 Percent Stops

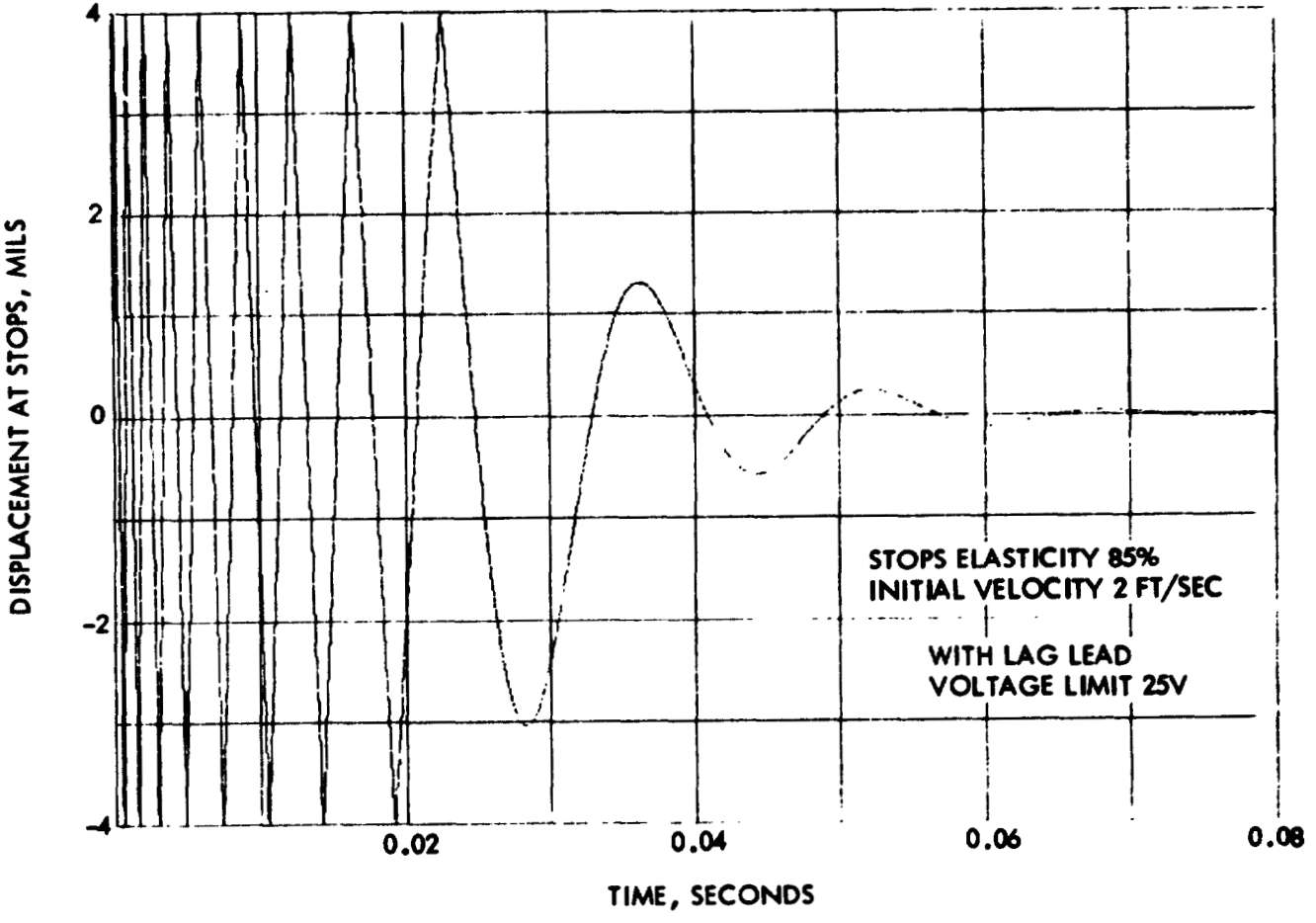

Figure 4-23. Limit Cycle Damping, 85 Percent Stops

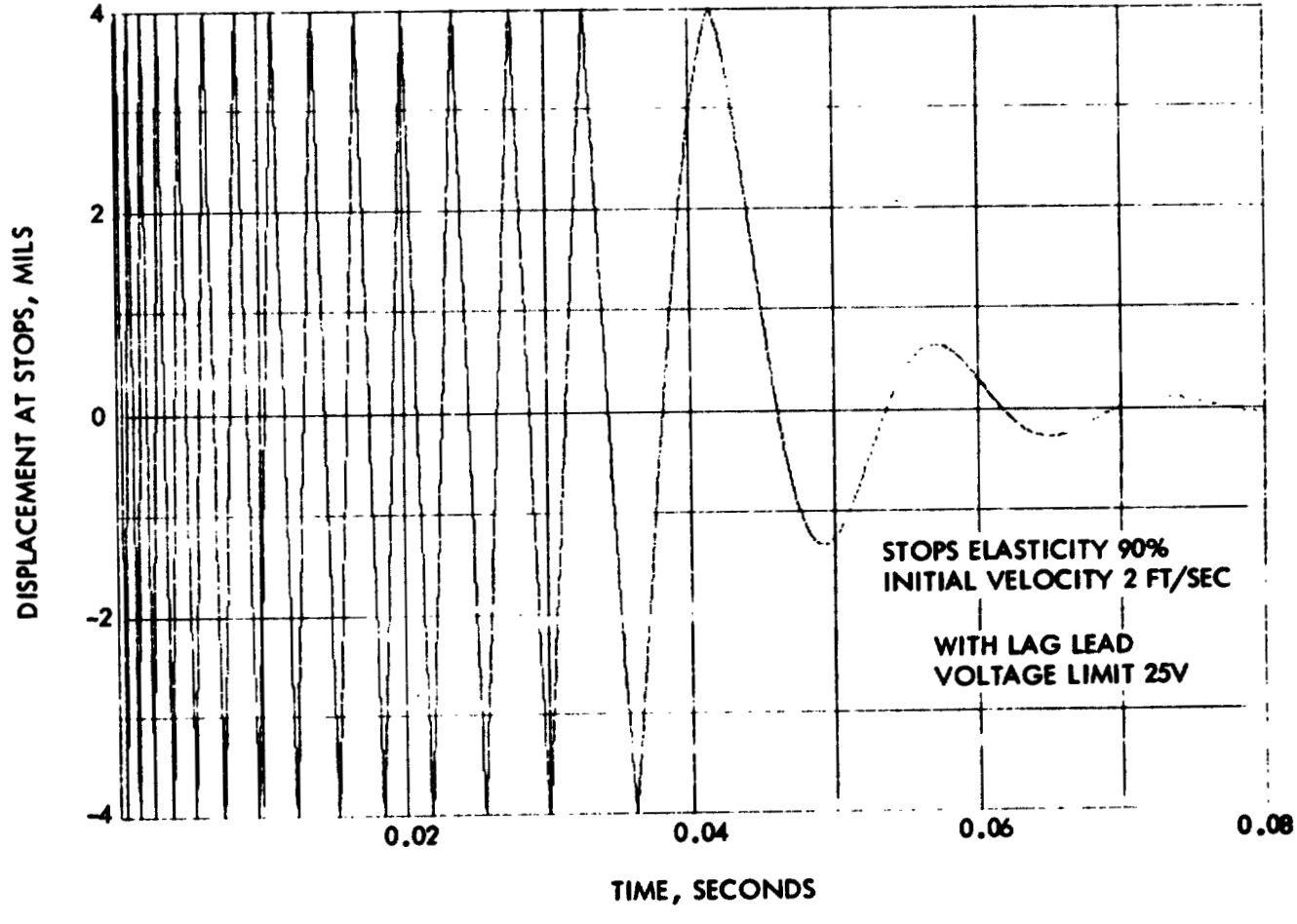

Figure 4-24. Limit Cycle Damping, 90 Percent Stops

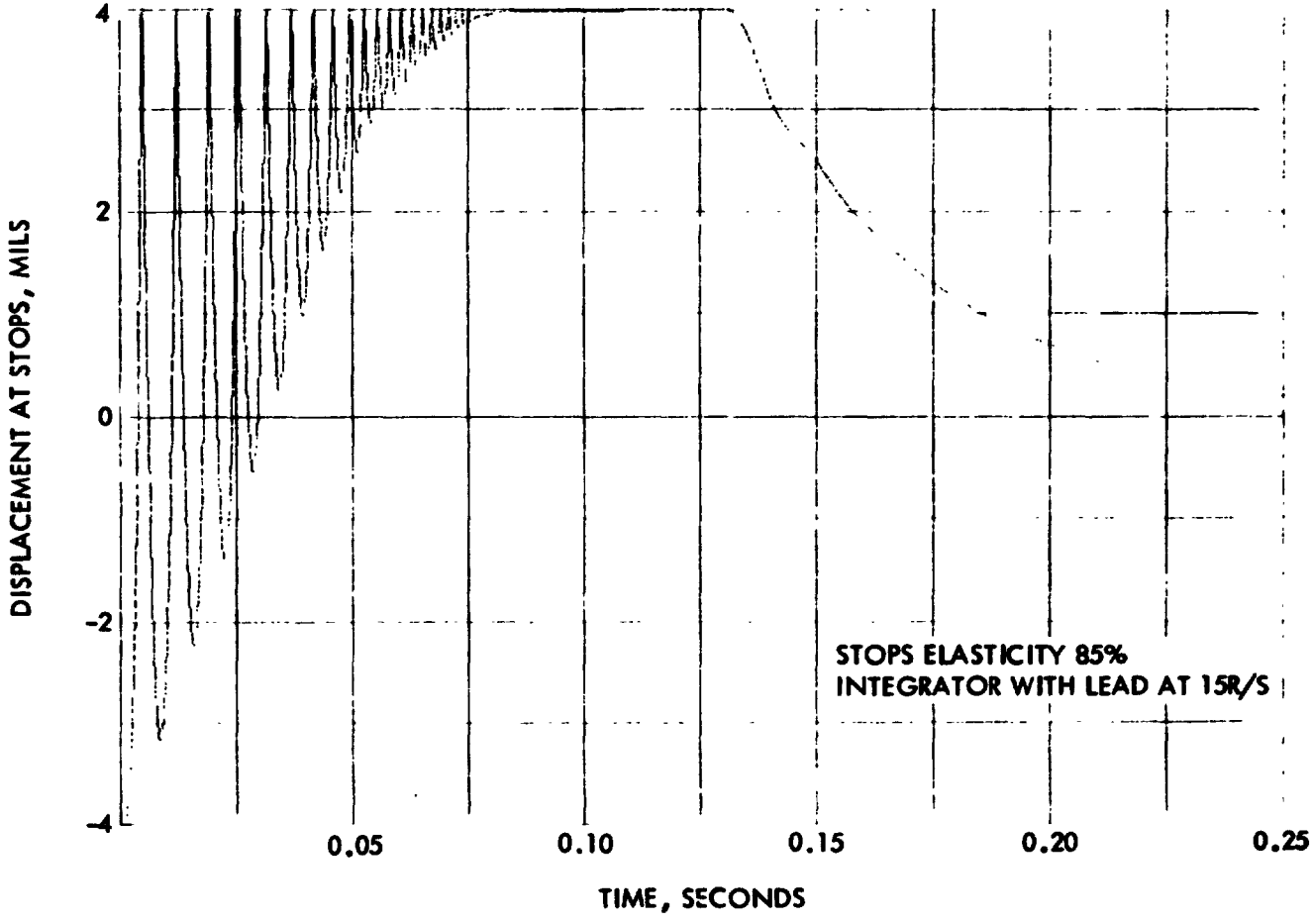

Figure 4-25. Pickup Response With Integrator

4.3 EFFECTS OF UNBALANCE AND ECCENTRICITY

The unbalance of the rotor assembly and the eccentricity of the magnetic pole pieces at the magnetic bearings and sensors can result in variations of the gaps at the back-up bearings which change as a function of spin speed. Thus if contact with the backup bearing is to be avoided the unbalance and eccentricity must be controlled. To determine the sensitivity of backup bearing gap to such characteristics the digital simulation was run with small input values and plots of error gradient versus spin speed obtained.

In an unbalanced rotor assembly there exists an axis about which there is perfect balance. Thus, unbalance can be described in terms of the displacement and angular orientation of the balance axis with respect to some reference axis. Likewise, eccentricities of the bearing, sensor, or backup bearing elements on the shaft can be thought of as establishing axes which are displaced and/or tilted with respect to a reference axis. The bearing dynamics can be described in terms of angular motions about the cg and independent linear motions of the cg, hence it is logical to study separately the effects of angular disturbances and linear disturbances. It must be realized that the results of the two types of disturbances must be combined vectorially, depending on the phase orientation of the disturbance in the cg relative to the plane of the angular disturbance.

The choice of reference axis is arbitrary. The assumption made here is that the backup bearing axis is the axis of perfect balance and zero eccentricities. If, for example, the reference axis were chosen otherwise, the results given here would have to have added the wobble of the backup bearing shaft with respect to the chosen axis.

The bearing servo loops attempt to control the position of the sensor rotor in its gap. If this should require that the balance axis be moved or the bearing rotor gap varied then for all but zero spin speeds the servo loop will have errors. The resulting errors in gap at the backup bearing vary with spin speed since the inertia forces and servo gains vary with frequency.

The variation in the gap at the backup bearing with an angular unbalance of the rotor is shown in Figure 4-26. If, for example, an unbalance of the rotor assembly existed such that the true balance axis at rest passed through the backup bearing one mil up at one end and one mil down at the other then that would be the reference or uncontrolled motion due to unbalance. The plot shows how the bearing servos attenuate this disturbance. The simulation used includes the gyroscopic coupling between axes.

Figure 4-27 shows the attenuation of linear unbalance motions. Again, if the unbalance of the rotor assembly was such that the true balance axis were linearily displaced from the backup bearing axis by one mil then the reference motion or zero db would be one mil variation at the backup bearing gap. As can be seen there is considerable attenuation of unbalance motions at low frequencies, but some actual amplification at higher speeds.

Eccentricities are described, for the reasons previously discussed, as either pure angular deviations of the effective axis or pure displacements. Thus the eccentricity described as an angular type would have matching but out of phase eccentricities on each end of the shaft, while linear motion eccentricities would have matching, in-phase eccentricities on both ends of the shaft. All eccentricities can be described by combinations of these two types, with the proper phase relationships.

Figure 4-28 shows the gradients in mils/mil of maximum excursion at the magnetic bearing pole and the backup bearing shaft for a given eccentricity at the bearing poles of the type where they are π radians (180 degrees) out of phase. Note as the frequency gets higher the motion at the backup bearing decreases and the motion at the suspension bearing approaches eccentricity. At very low frequencies the servo error integrator centers the sensor and hence the backup bearing; but at mid-frequencies the positive feedback forces in the bearing pull the eccentric bearing pole rotor even farther off, causing backup bearing motions.

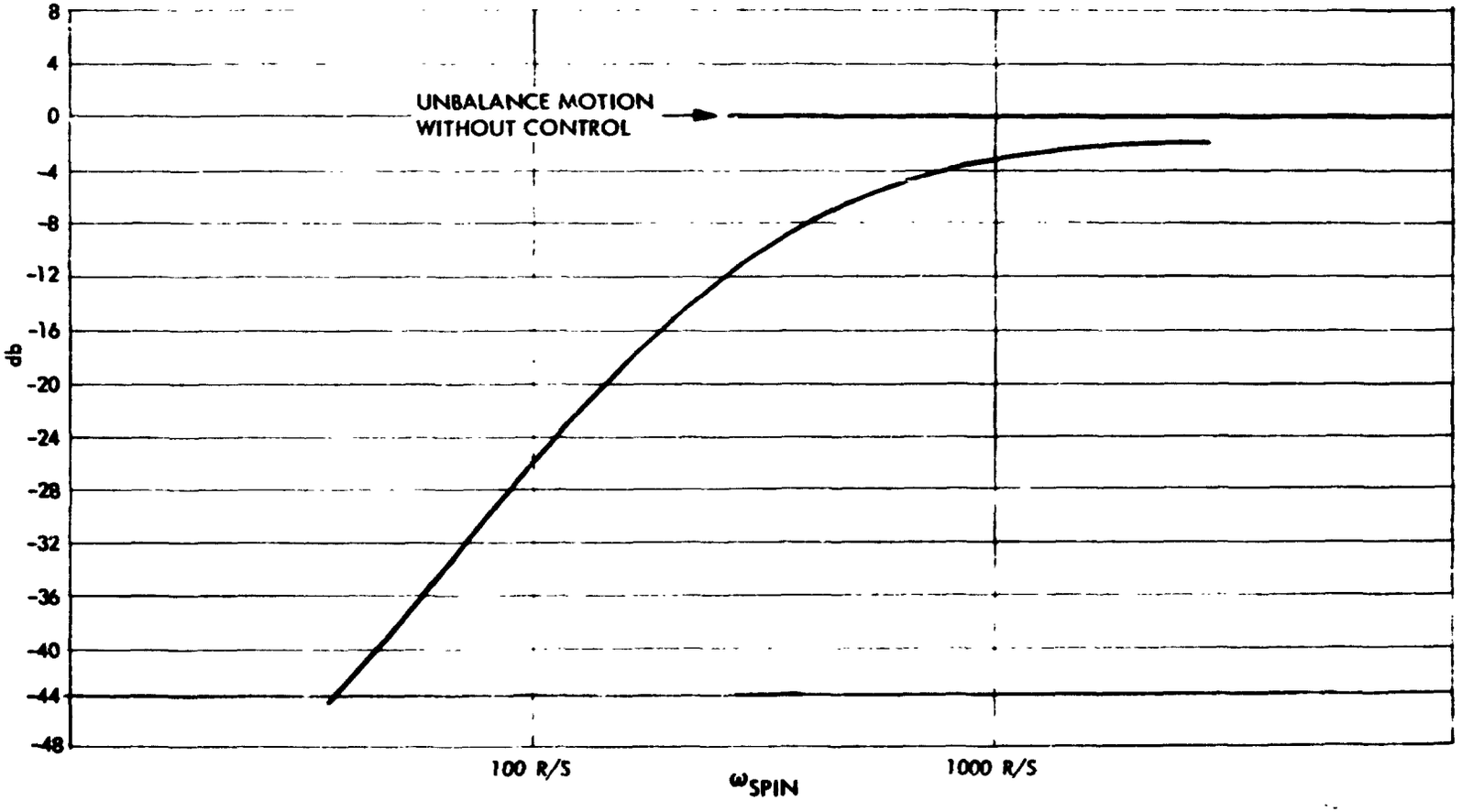

Figure 4-26. Attenuation of Angular Unbalance Motions by Bearing Servos

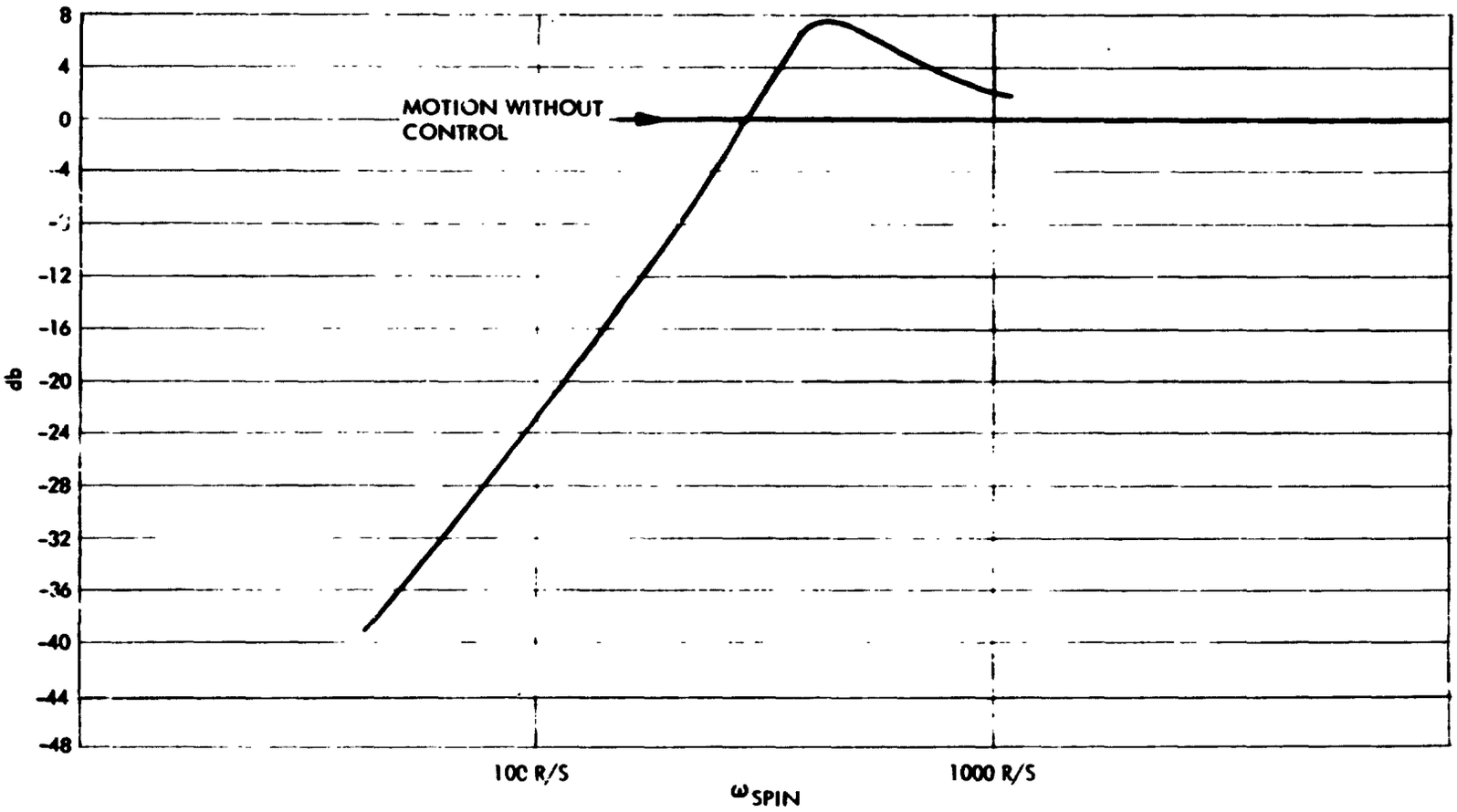

Figure 4-27. Attenuation of Linear Unbalance by the Bearing Servos

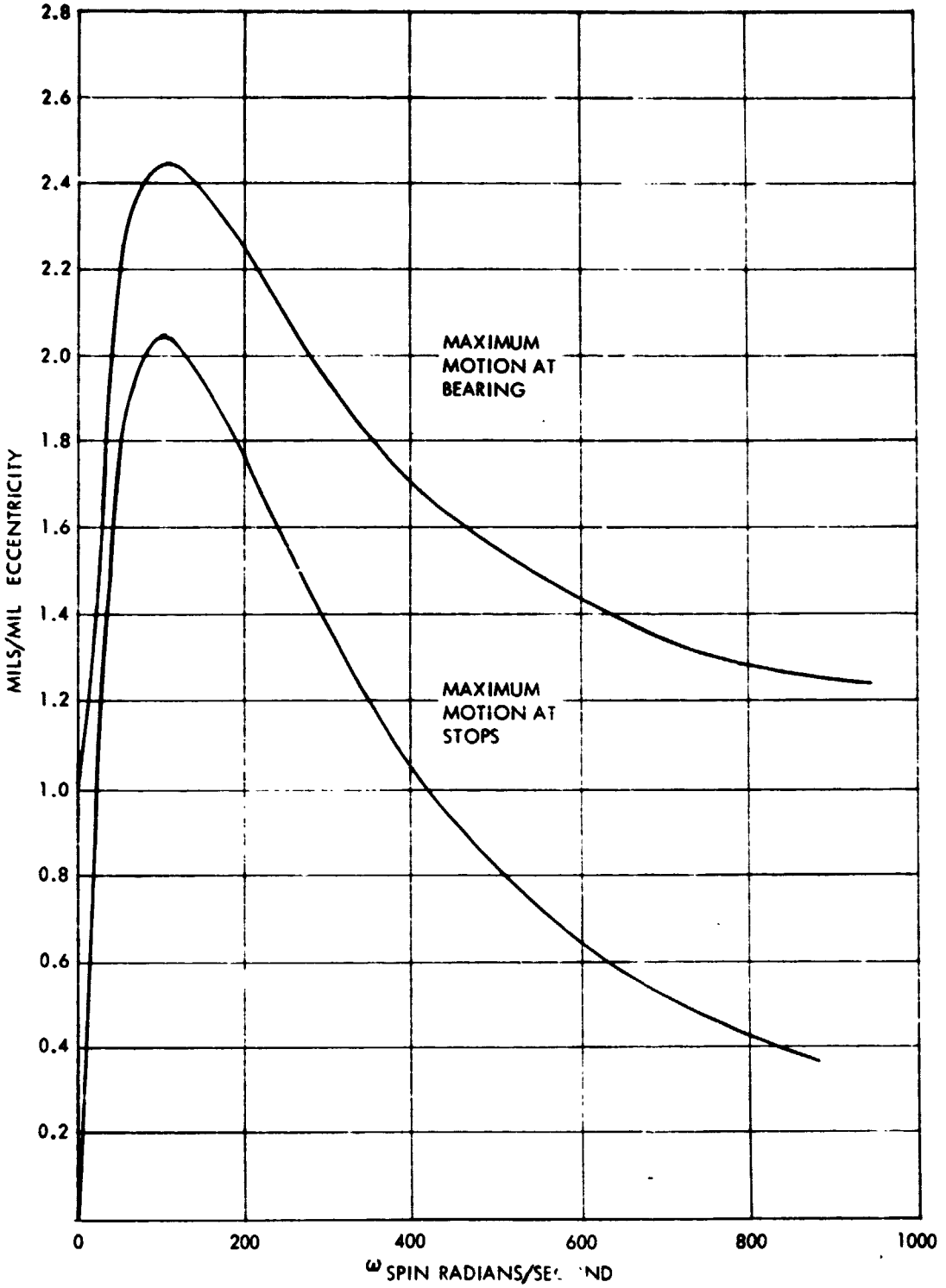

Figure 4-28. Bearing and Stops Displacements due to Out of Phase Eccentricity at the Bearing Rotor

In a similar manner angular type eccentricities at the sensor rotors cause variations at the backup bearing gap (Figure 4-29). In this case the sensor is trying to control the rotor about an axis which is not the balance axis and at high speeds the rotor tends to return to its balance axis and cause sensor errors. The error multiplication from the sensor indication to the backup bearing variation is due to the facts that the sensor error is actually opposite the eccentricity (due to suspension bearing positive feedback forces), and there is a lever arm effect between the inboard sensors and the outboard backup bearing.

In-phase eccentricities result in linear motions of the cg. Figure 4-30 shows the results of eccentricities at the suspension bearing. Note that at mid-frequencies the bearing positive feedback forces cause errors at the sensor and backup bearing which are not exactly one unit different from those of the eccentric bearing. This is due to a phase shift between the various peaks relative to the input eccentricity.

Figure 4-31 shows the results of in-phase eccentricities of the sensor rotors relative to the reference axis through the backup bearing. Again, there are phase differences between the various peak displacements.

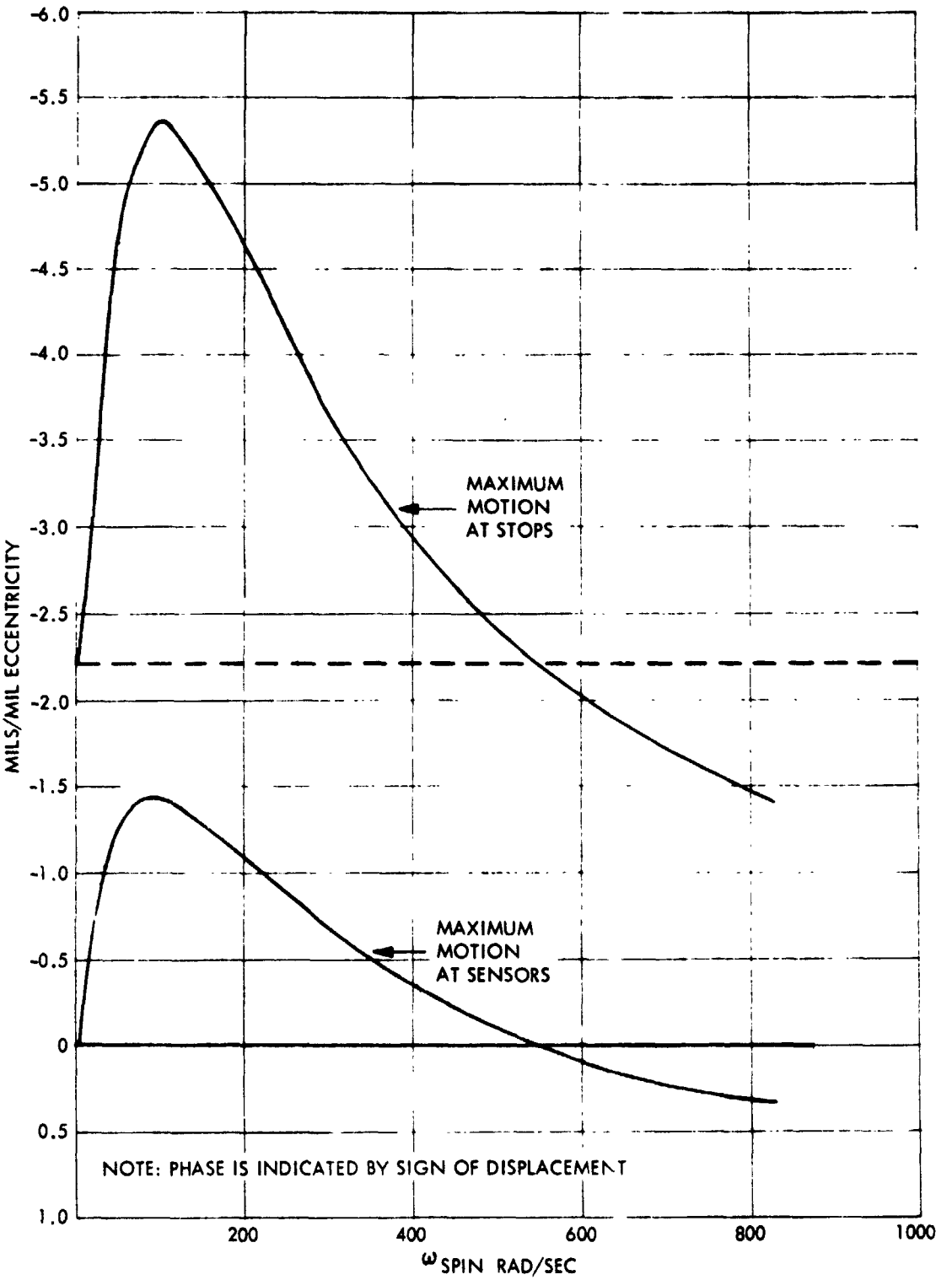

Figure 4-29. Sensor and Stops Displacements due to Out of Phase Eccentricity at the Sensor Rotor

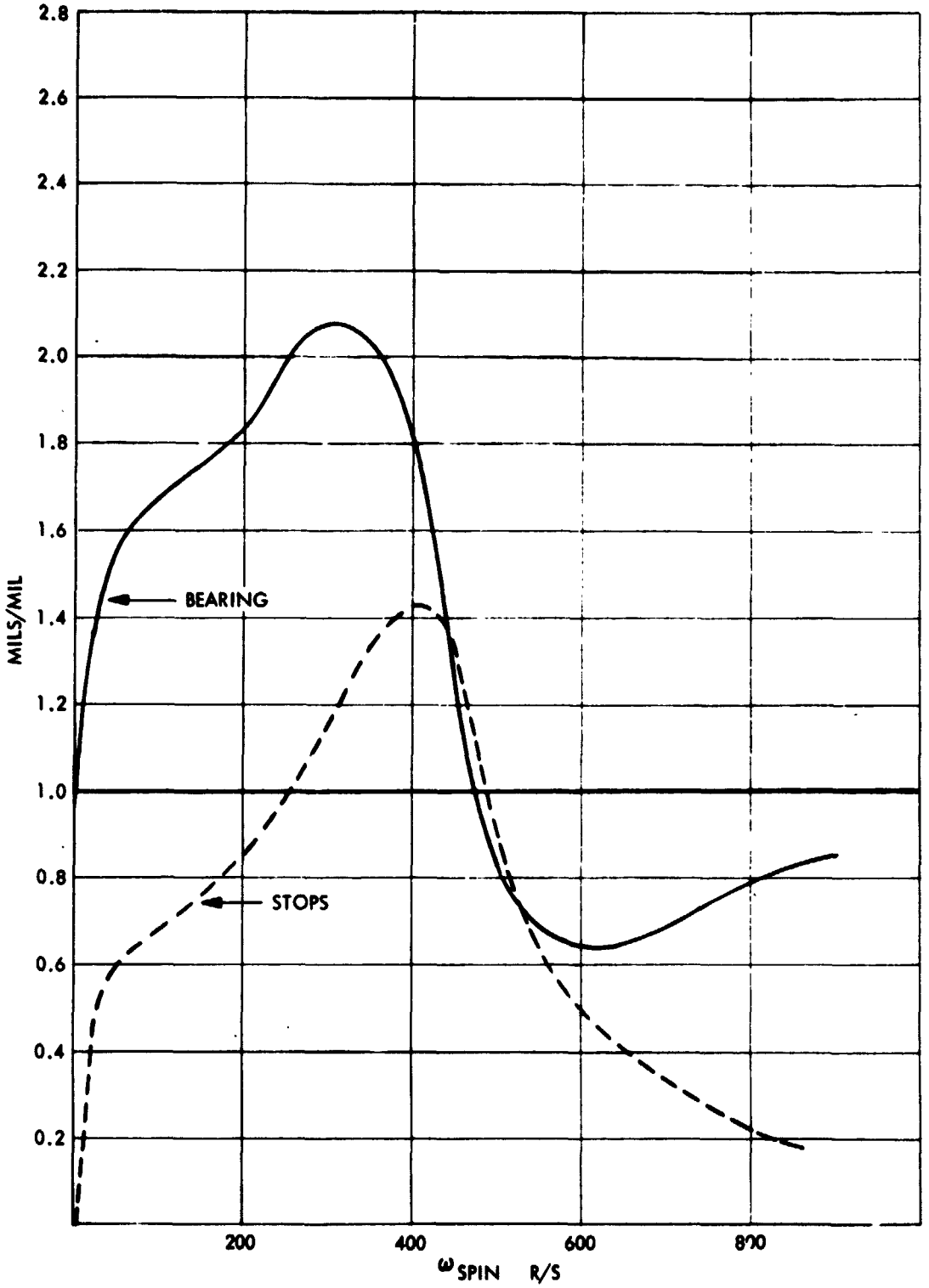

Figure 4-30. Bearing and Stop Displacements due to In-phase Eccentricity at the Suspension Bearing Rotor

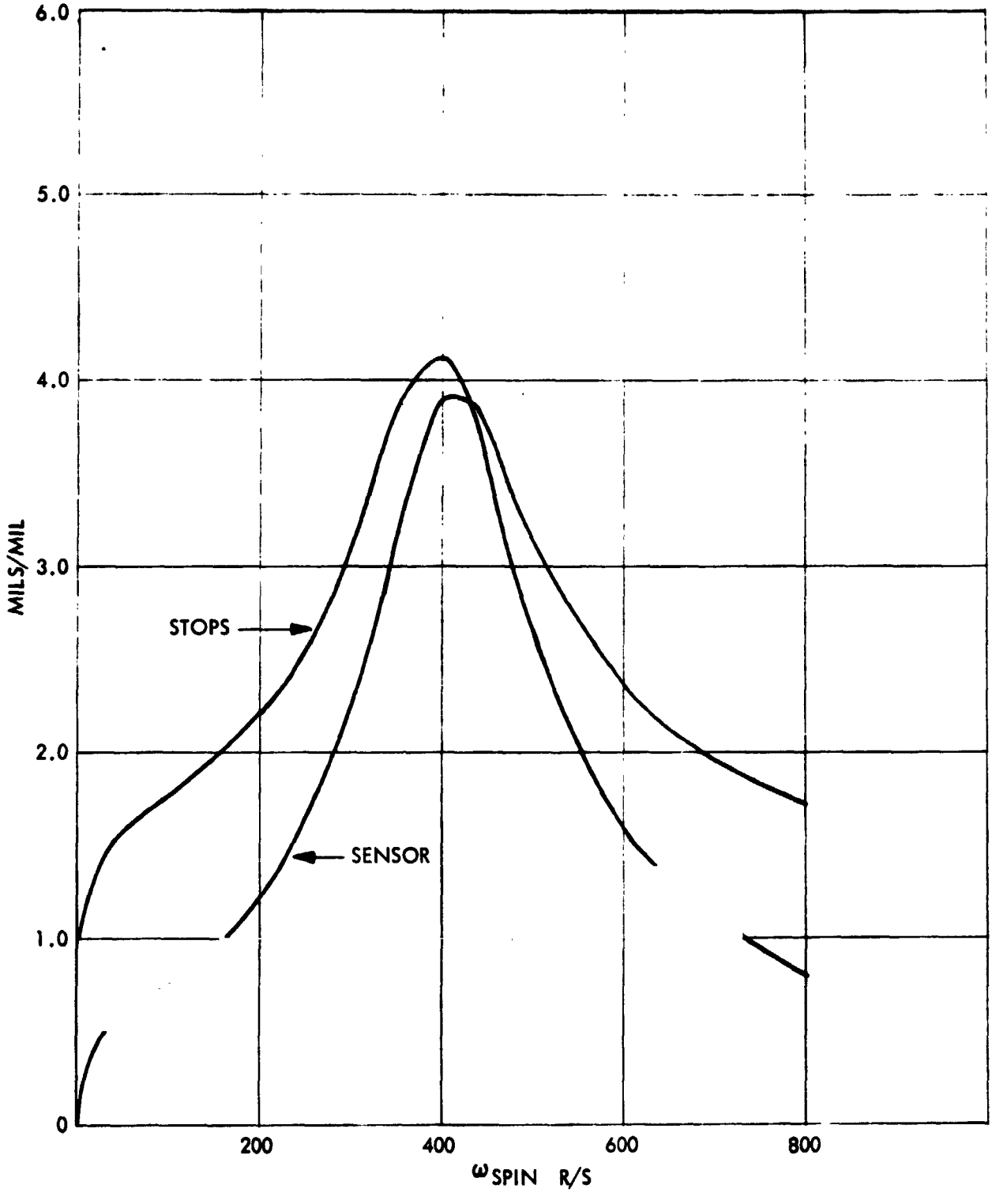

Figure 4-3. Sensor and Stops Displacements due to In-phase Eccentricity at the Sensor Rotor

Section 5
ELECTRONICS/MOTOR DESIGN AND MAGNETO RESISTOR DESCRIPTION

The electronics design for the magnetically suspended momentum wheel consists of the following blocks or parts:

1. Bearing servo electronics
2. Spin motor drive electronics
3. Control or switching electronics

The following discussion further defines the above as to function and characteristics.

5.1 BRUSHLESS DC MOTOR DESIGN

An existing General Electric brushless dc motor was used as the spin motor for the magnetically suspended momentum wheel. Although the motor does not have an ironless armature construction,* it appears ideally suited for this application, having the following features:

- High efficiency at the torque levels required
- Proper size for this application
- Exhibits true permanent magnet dc operation
- Completely proven design

* An ironless armature construction, using the basic General Electric brushless dc motor principal, has been designed. The advantages of this motor would be the elimination of magnetic losses and side forces, but with an increase in weight and I^2R losses.

The motor is one of several brushless dc motors developed by General Electric that operate on the "sine-cosine resolver" principle - no full off to full on current switching as a function of angle is employed - and smooth, precision torque and speed control is obtained.

The required maximum motor torque is determined by the specified spin-up time of 1.2 hours:

$$T = \frac{H}{t} = \frac{101.69}{1.2 \times 3600} \text{ N-m}$$

$$= 0.02354 \text{ N-m } (3.33 \text{ in-oz})$$

To assure adequate torque to allow for bearing and windage drag, the motor torque has been set at

$$T_m = 0.02824 \text{ N-m } (4.0 \text{ in-oz})$$

This assumes, of course, a constant torque during spin-up. All General Electric spin motor systems have been developed for constant spin-up torque, as this results in the minimum input energy (from the 28 vdc supply) to achieve spin-up; however, other torque-speed characteristics can easily be generated if required.

The motor running torque requirement is based on the expected drag torque due to the magnetic bearing, windage, and motor core losses. This is about 0.0028 N-m (0.4 in-oz).

Based on the above torque requirements, an existing General Electric brushless dc motor was used. The characteristics of this motor, with motor winding constants adjusted for this application, are given in Table 5-1. An outline sketch of the motor is shown in Figure 5-1.

This motor was originally developed as a torque motor on NASA/MSFC contracts NAS8-11658 and NAS8-20591. In this application it was rated at 0.1412 N-m (20 in-oz) but was capable of delivering 0.2118 N-m (30 in-oz) without demagnetization. This same motor was later used (with different winding constants) as a spin motor for the 27.11 N-m-sec (20 ft-lb-sec) CMG's built by GE/ACS for NASA/MSC. Eight CMG's were delivered on contract NAS9-8181. In this application the motors operated at 0.02118 N-m (3 in-oz) torque and 75,400 rad/sed (12,000 rpm), values similar to those required in this momentum wheel application.

TABLE 5-1

BRUSHLESS DC MOTOR CHARACTERISTICS

Motor Size		
Outside Diameter	6.985 cm	(2.75 inches)
Axial Length (stator)	1.524 cm	(0.60 inches)
Weight (with Hall resolver)	0.272 kg	(0.6 lbs)
Performance Data		
Rated Torque	0.02824 N-m	(4 in-oz)
Peak Torque Capability	0.21185 N-m	(30 in-oz)
I^2R Losses at Rated Torque	2.25 watts	
Core losses at 628 rad/sec (6000 rpm)	0.035 watts	
Winding Constants:		
Torque Constant	0.02824 N-m	(4 in-oz/amp)
Current for Rated Torque	1.0 amps	
Resistance, Each Phase	2.25 ohms	
Generator Constant	0.00047V pk/ rad/sec	(0.00296V pk/rpm)
Back EMF, 628 rad/sec (6000 rpm)	17.75V pk	
Inductance, Each Phase	1.4 mh	
Radial Unbalance Force	≈ 47,280 N/m	(270 lb/in)
Motor Construction		
Type	Two Phase	
Number of Poles	6	
Rotor Magnet	Alnico 6	

Motor History

Fully Developed
Used as both a torque motor and spin motor
Employed as spin motor in eight 27.11 N-m-sec (20 ft-lb-sec) CMG's (1,256 rad/sec) (12,000 rpm) delivered to NASA/MSC

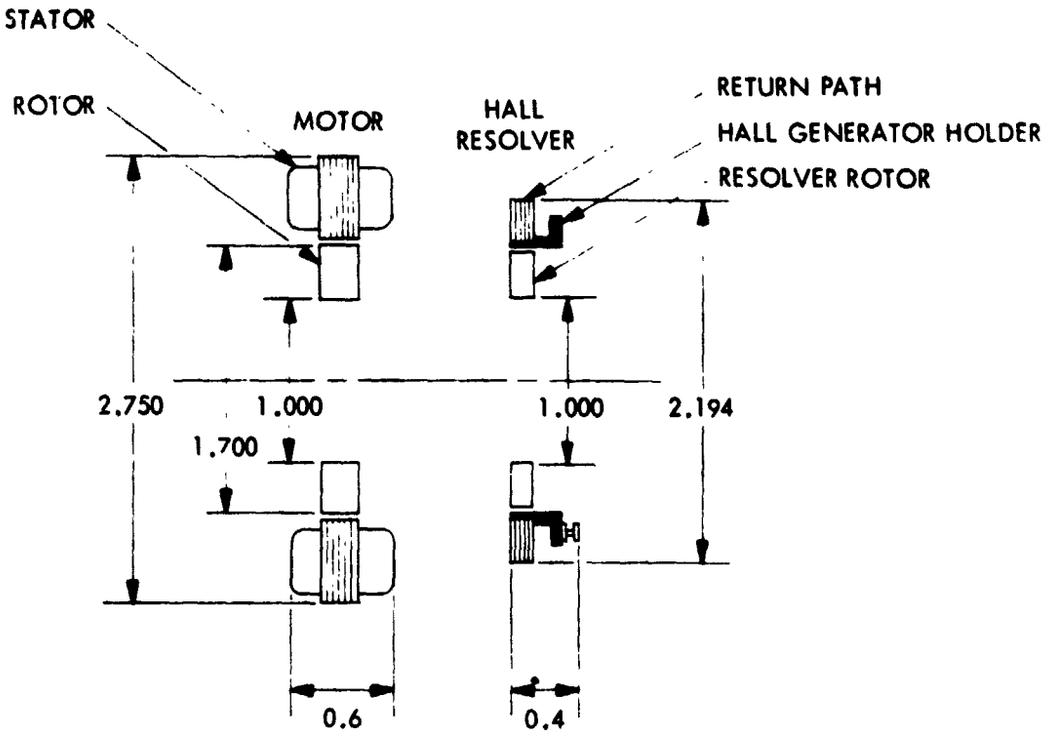

NOTE 1. ALL DIMENSIONS IN INCHES.

NOTE 2. FOR REFERENCE ONLY. SEE APPLICABLE DRAWINGS FOR ALL DIMENSIONS AND TOLERANCES.

Figure 5-1. Brushless DC Motor Outline

This motor meets the specified NASA/GSFC requirements for torque capability, efficiency, etc. Two motor characteristics particularly important to this application were especially reviewed - the motor magnetic core losses and the destabilizing radial magnetic force. These will be briefly discussed.

- Motor Core Losses

  The brushless dc motor uses 6 mil nickel-steel stator laminations to minimize core losses due to the rotating magnetic field from the rotor. These losses have been carefully calculated, and are given approximately by:

$$P_C = [0.01+0.037\ (\frac{rpm}{10,000})^{0.8}\ \text{in-oz}]x(0.0070615)\ \text{N-m}$$

  over the speed range of 104-2,094 rad/sec (1,000-20,000 rpm). The core losses are seen to be very low - only 0.00029 N-m (0.041 in-oz) at 838 rad/sec (8000 rpm) for instance. This is only one-tenth of the assumed magnetic bearing losses of 0.0029 N-m (0.41 in-oz), at 838 rad/sec (8000 rpm). Hence, the motor contribution to the overall spinning losses is quite minor, as desired.

- Motor Radial Magnetic Force

  If the motor rotor is not centered in the stator, there is a radial magnetic force pulling the rotor to one side. It is important that this force be minimized, since it could destabilize the magnetic bearing support, if sufficiently large.

  This destabilizing force has been measured on this motor, and is only about 3.559 N (0.8 lb) at a 0.0762 mm (3 mil) rotor displacement from center. This is equivalent to a 46,700 N/m (0.27 lb/mil) destabilizing force gradient. This is essentially insignificant compared to the magnetic bearing force gradients, and hence should have negligible effect on the magnetic bearing operation.

5.2 ELECTRONICS DESIGN

This subsection describes the design of the electronics for the magnetically suspended momentum wheel, and consists of discussions in the following areas.

- General Discussion - configuration, power leads, status monitoring.
- Electronics Design - motor and bearing control.
- Packaging Design
- Power Calculations

The electronics make full use of General Electric's wide past experience with circuits for brushless motors, reaction wheels and CMGs. The electronics for the magnetically suspended momentum wheel use fully developed circuits as the basic building blocks, allowing the main emphasis to be placed on optimizing the overall bearing and spin motor control to achieve minimum power and high reliability.

5.2.1 GENERAL DISCUSSION

A block diagram of the brushless dc spin motor electronic module is shown in Figure 5-2. It consists of the following:

1. Power Amplifier
2. Speed Control Circuit
3. Status Monitoring and Redundancy Switching Circuit

The power amplifier provides the essential commutation function of the brushless dc motor, amplifying the Hall generator voltage to drive the motor winding. The amplifier operates in a switching mode (class D) using pulse width modulation. The same basic amplifier circuit is used in both the spin motor electronics and the bearing servo electronics.

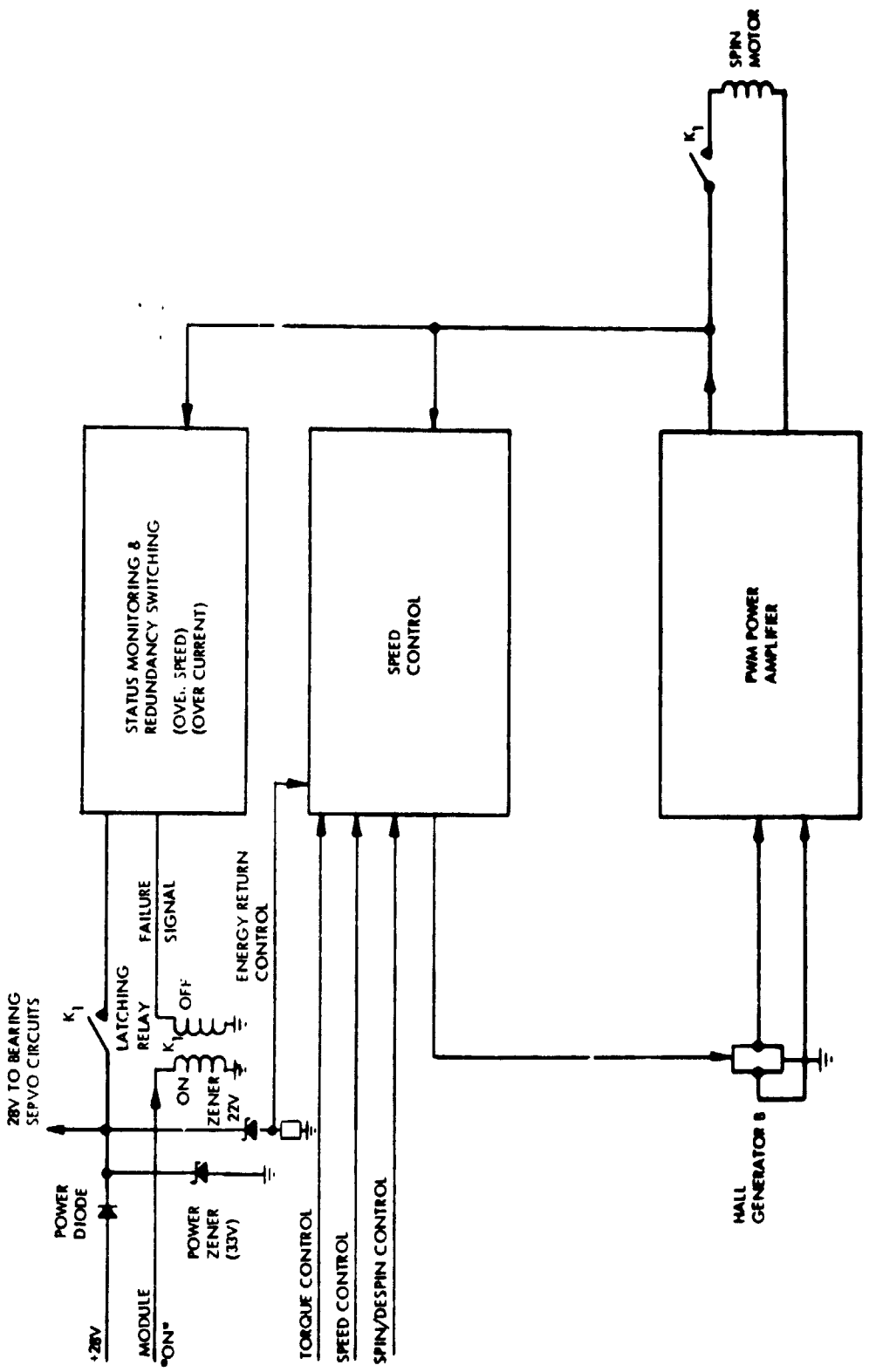

Figure 5-2. Spin Motor Module

The entire electronics consist basically of a combination of power amplifiers and operational amplifiers. Redundancy is needed in each of the three groups of electronics to achieve the desired reliability.

Pulse width modulated amplifiers achieve very high efficiency since transistors are used as switches. This high efficiency is obtained at all output voltage levels. PWM amplifiers have been in development at General Electric for over four years. In conjunction with NASA/MSFC and USAF contracts, PWM power amplifiers with output capabilities from 10 to 500 watts have been developed and fabricated. Current feedback has been employed in nearly all these amplifiers. This type of amplifier generally requires no more components than linear (class B) amplifiers, and are considerably easier to package because of the much lower power losses.

The PWM power amplifier also has the unique capability, if properly designed, to provide regenerative "braking". Thus, it is used to despin the momentum rotor, and also to use the energy stored in the rotor to power the bearing servos in case power is lost. The capability of General Electric designed brushless dc spin motor system to effectively utilize rotor energy has been demonstrated in several cases (References 6, 7).

The speed control circuit provides the overall control of the spin motor system. The basic speed control operates from the frequency determined from the motor back-emf. This frequency is converted to dc by a single-shot, and then compared to the input speed command signal to generate an error signal that controls motor torque, resulting in the desired closed loop control of the rotor speed. This type of speed control has been employed in several CMG's with excellent results. The speed control characteristics are further illustrated in Figure 5-3.

This speed control module provides for motor torque command control and for rotor spin or despin. A simple control circuit to utilize the rotor stored energy to supply bearing power in case of power disruption is incorporated. This is achieved by sensing when the power line has dropped below 23 volts and commanding rotor despin in a closed loop manner to supply 23 volts to the bearing (see Figure 5-2). It is

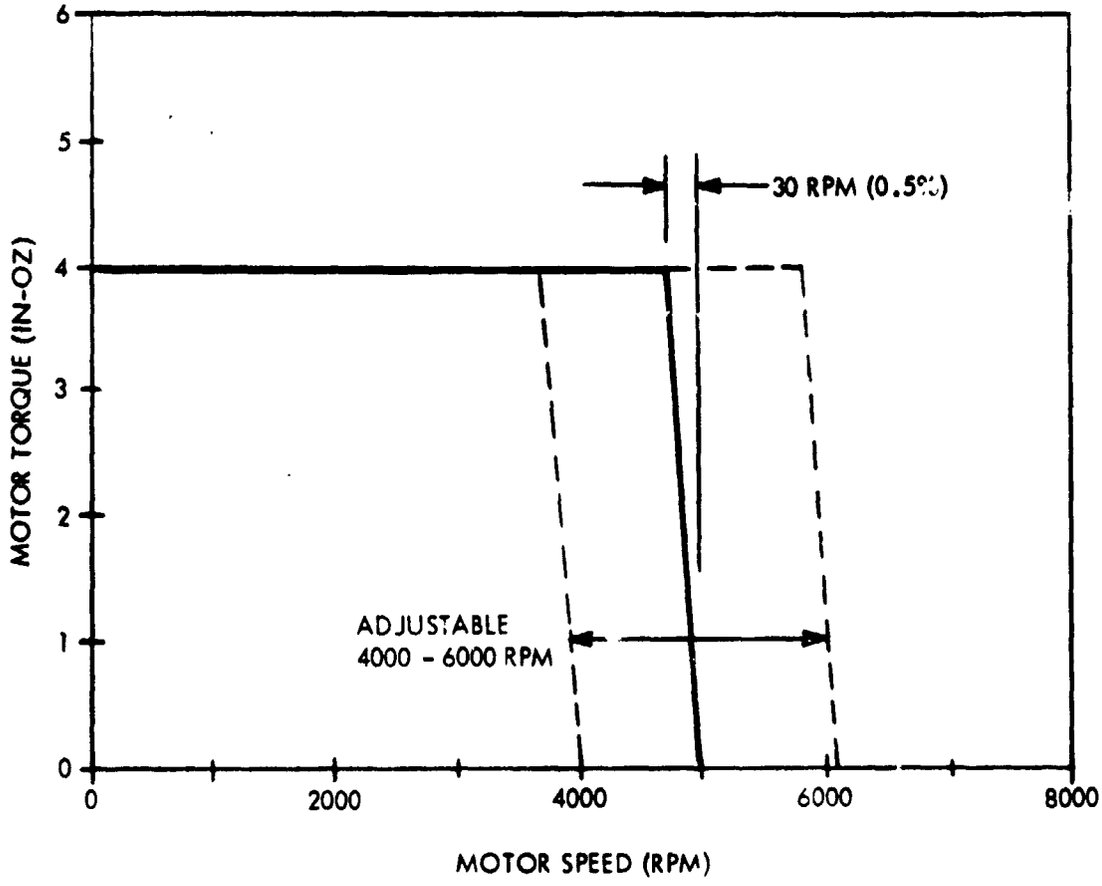

Figure 5-3. Torque-Speed Curve for Brushless DC Spin Motor System

estimated that about one-half of the stored energy of 8.9 watt-hours, or about 4.5 watt-hours may be efficiently utilized, allowing roughly 1 hour of operation without input power.

The spin motor module also contains a status monitors/redundancy switching circuit to provide automatic shutdown of the spin motor module in case the module is not operating properly. This is done by sensing an overspeed or overcurrent signal, with simple circuits, and providing a failure signal that turns off the latching relay that supplies module power. This same relay disconnects the spin motor from the circuit to assure that an undesirable drag torque is not produced. This circuit has been successfully employed by General Electric in the 881 N-m-s (650 ft-lb-sec) CMG spin motor electronics. The overspeed circuit is easily adjustable; it has been set at 125% of the nominal rotor speed.

5.2.2 ELECTRONICS DESIGN - BEARING SERVO POWER AMPLIFIERS

The bearing servo power amplifiers, as shown as a block in Figure 4-3, are also pulse width modulated to maximize efficiency and minimize bearing power under high load conditions. The two electromagnets in each axis are driven by one PWM power amplifier so as to decrease the net flux in one gap and increase it in the other, as shown in Figure 5-4, as a function of the shaft position sensor in that axis.

5.3 MAGNETO-RESISTOR DESCRIPTION

In order to mechanize the radial bearing servos, magnetic resistors at each bearing were used to measure shaft position at each location. These resistors arranged in a fashion similar to Figure 5-5, sense changes in the permanent magnet bias field due to a shift of the shaft by changing resistance. The gain characteristic of a single magneto-resistor is shown in Figure 5-6 as a function of flux density. When used in a bridge arrangement with a reference voltage, V_r, the position sensor output is a voltage proportional to the location of the shaft with respect to the center of the bearing.

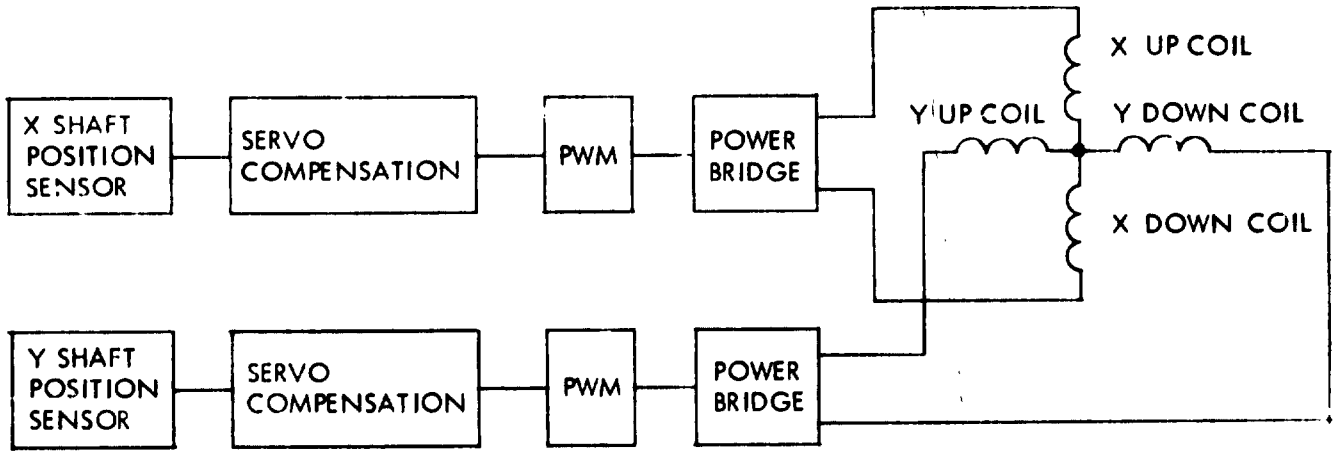

Figure 5-4. Bearing Servo Electronics Block Diagram

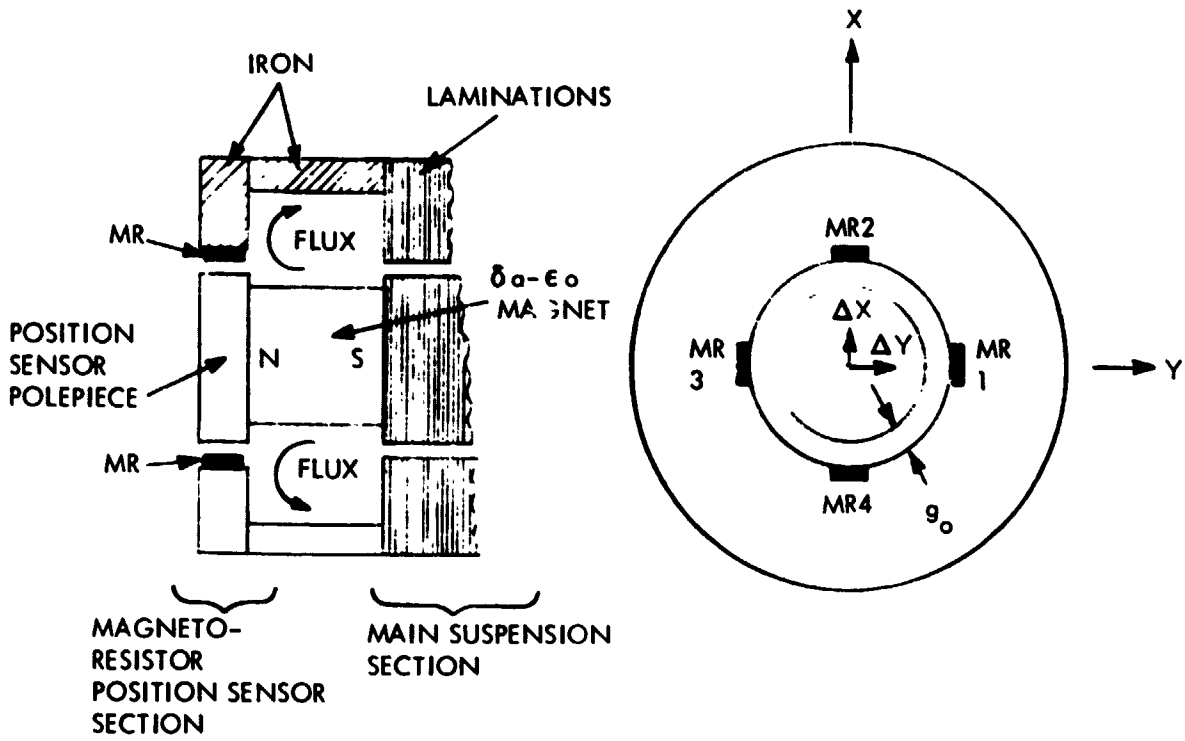

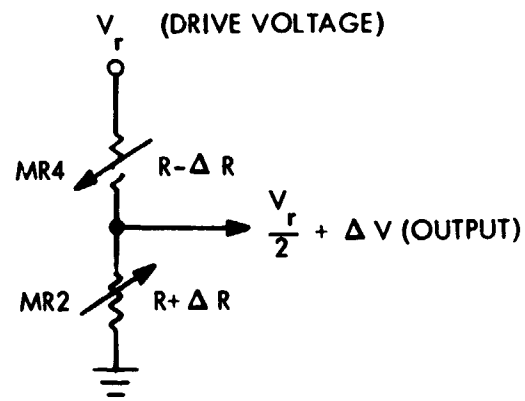

Figure 5-5. Magneto Resistor Arrangement

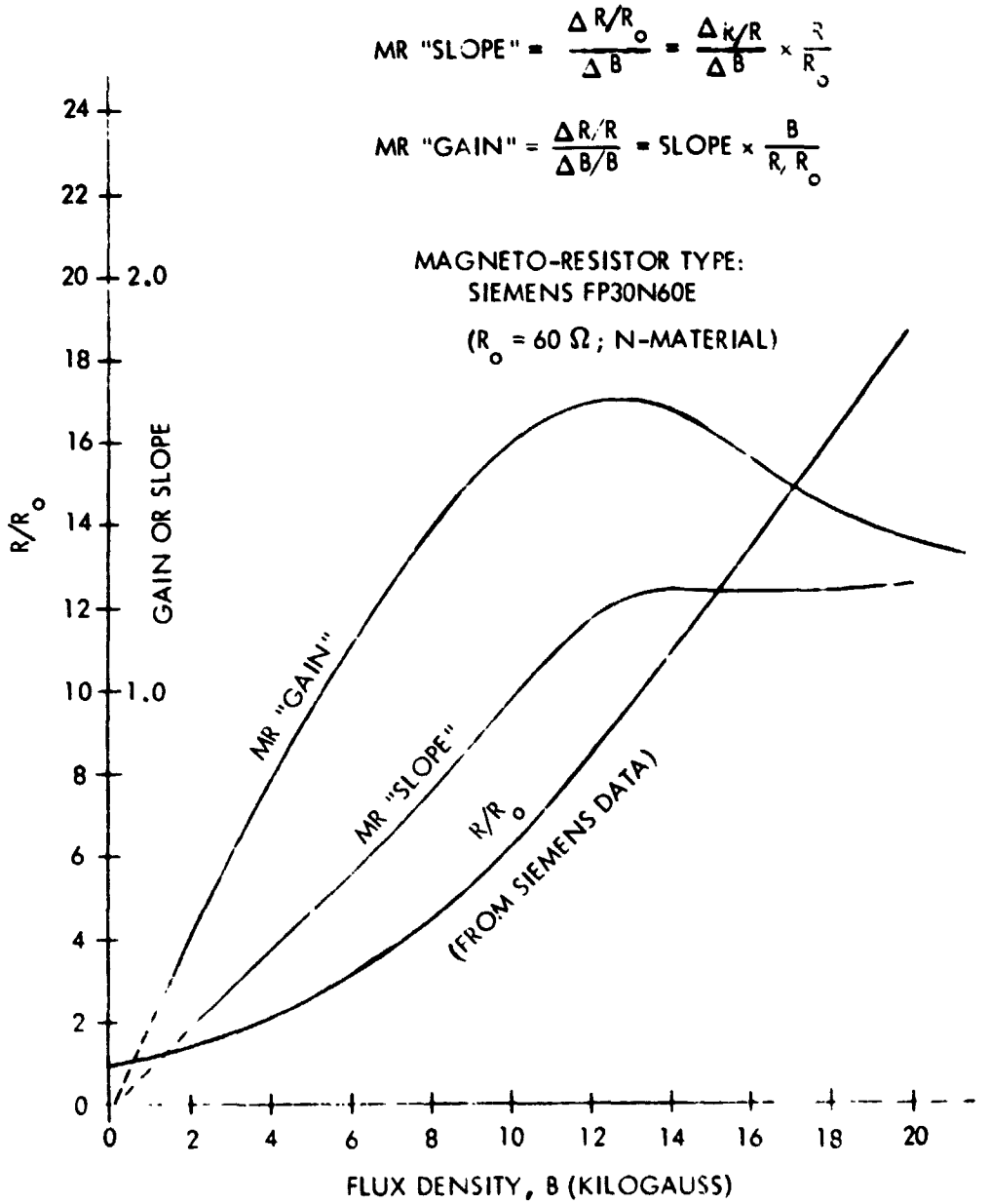

Figure 5-6. Magneto Resistor Characteristics

Section 6
TEST RESULTS

6.1 SUMMARY

The tests of the engineering model of the magnetically suspended momentum wheel were conducted to determine its operating characteristics, and to confirm and refine the design analyses. The tests consisted of the following:

1. Measurement of the magnetic bearing characteristics.
2. Measurement of the bearing suspension servo responses.
3. Measurement of the engineering model performance at various rotor speeds.

Test results showed the actual bearing characteristics such as stiffness, load capacity, power, etc., to be essentially the design values, thus verifying the basic magnetic design. The bearing servo response tests, including the actual rotor and shaft, indicated the importance of the frequency location of the structural modes of the rotor/shaft in determining the maximum bearing servo bandwidth, and thus indirectly the maximum rotor speed and the response to base vibration. The spin-up tests revealed bearing drag characteristics and developed design criteria for the back-up bearing.

In general, the results verified the basic magnetic design, showed the feasibility of this technique for suspending momentum wheels, and developed data and criteria for future designs.

6.2 MAGNETIC BEARING CHARACTERISTICS

The magnetic bearing characteristics of interest are the radial load capacity, axial load capacity, bearing stiffness in both axes and bearing power. Tests were conducted

with the momentum wheel suspended on both bearings; loads were applied to the rotor radially and axially, and bearing suspension currents and rotor displacements were measured. Figures 6-1 through 6-4 present the data.

Figure 6-1 shows the radial load capacity of each bearing and the linearity of the lectromagnets. With a current capability of approximately 2.0 amperes in each coil and power amplifier, the two bearings can support at least 36.3 kg (80 lbs). There is approximately a 15% difference between the gains of the two bearings, which can be largely attributed to differences in the cobalt-samarium magnet strengths. The average strength of a bearing is 8.16 kg/amp (18 lbs/amp). Figure 6-2 shows the corresponding input power to both bearings under the same loads and indicates that 36.3 kg (80 lbs) can be supported by supplying approximately 19 watts. For small loads, the slope is approximately 0.44 watts/kg (0.2 watts/lb).

Figure 6-3 shows the characteristics of the passive axial support of the two bearings. Loads were applied axially with the rotor suspended and the displacement was measured. The curve shows a total capacity of at least 18.1 kg (40 lbs) for two bearings and a linear displacement versus load relationship up to 13.6 kg (30 lbs) with a gain of approximately 0.0658 mm/kg (0.6 mils/lb).

The radial stiffness of the bearing pair, which depends upon the electronic servo gains, was also measured with the rotor suspended and weight applied to it. The results are shown in Figure 6-4 and indicate displacements of less than 0.0127 mm (0.5 mils) for loads up to 36.3 kg (80 lbs).

6.3 MAGNETIC BEARING SERVO RESPONSES

Frequency responses of a single electronics channel such as that shown in Figure 4-3 as well as closed loop frequency responses of the suspended rotor translationally and torsionally were run and are depicted in Figures 6-5 through 6-7.

The total electronics frequency response, as shown in Figure 6-5, shows the lead-lag network from approximately 408 to 3141 rad/sec (65 to 500 Hz) needed for stabilization as well as the notch filter at approximately 3204 rad/sec (510 Hz) to reduce the amplitude of the rotor/shaft structural resonance.

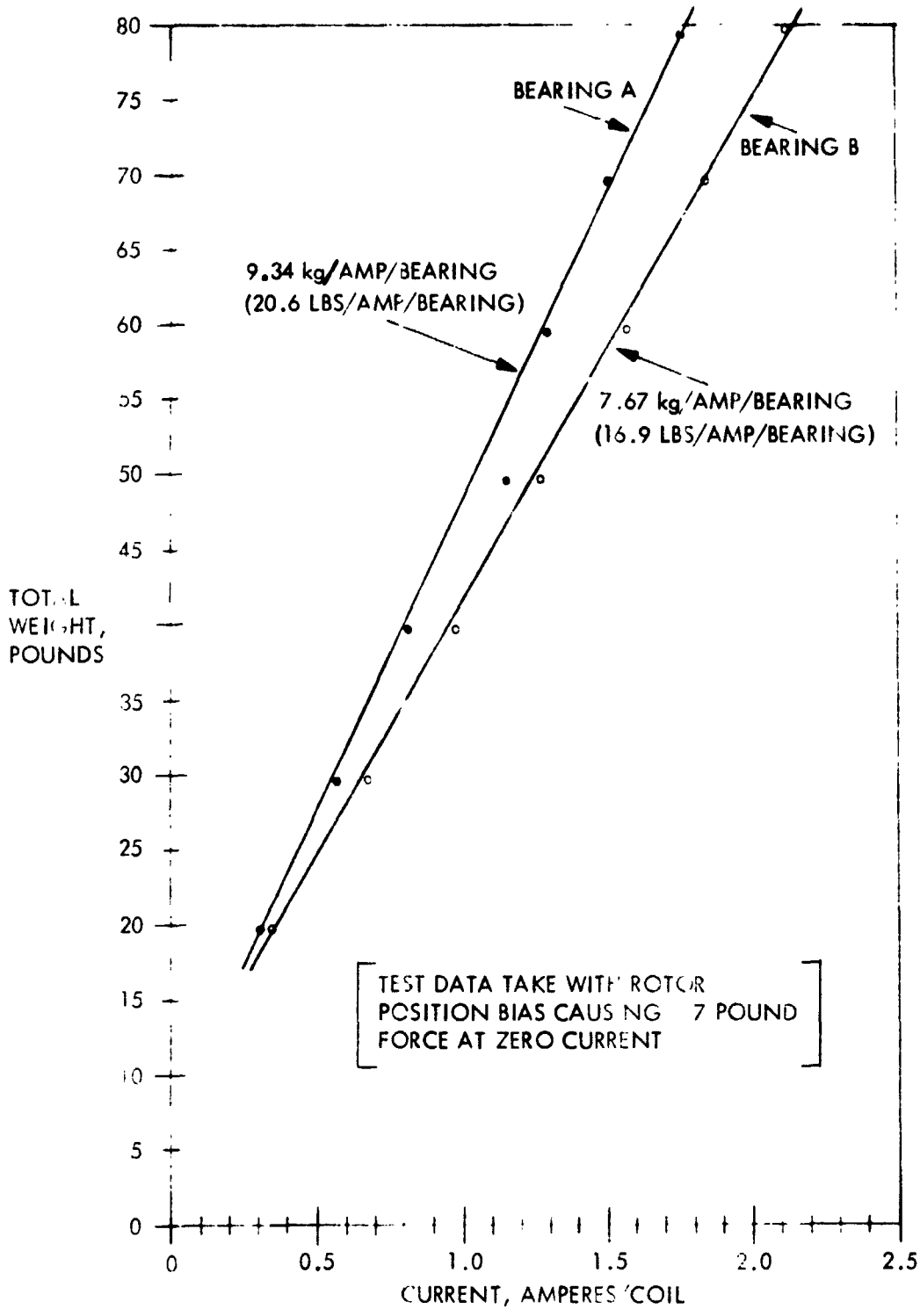

Figure 6-1. Magnetic Bearing Radial Load versus Current

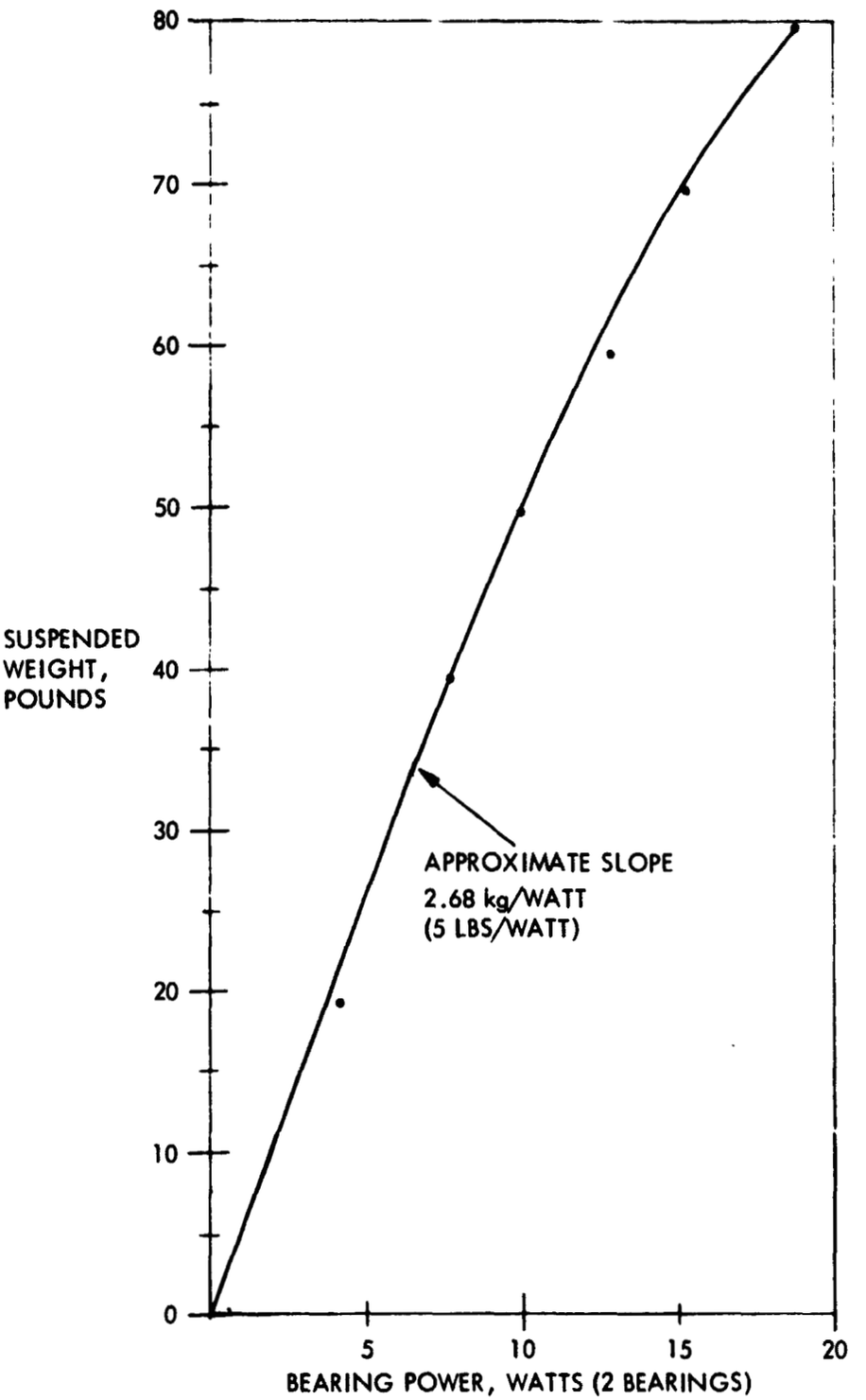

Figure 6-2. Magnetic Bearing Radial Load versus Input Power

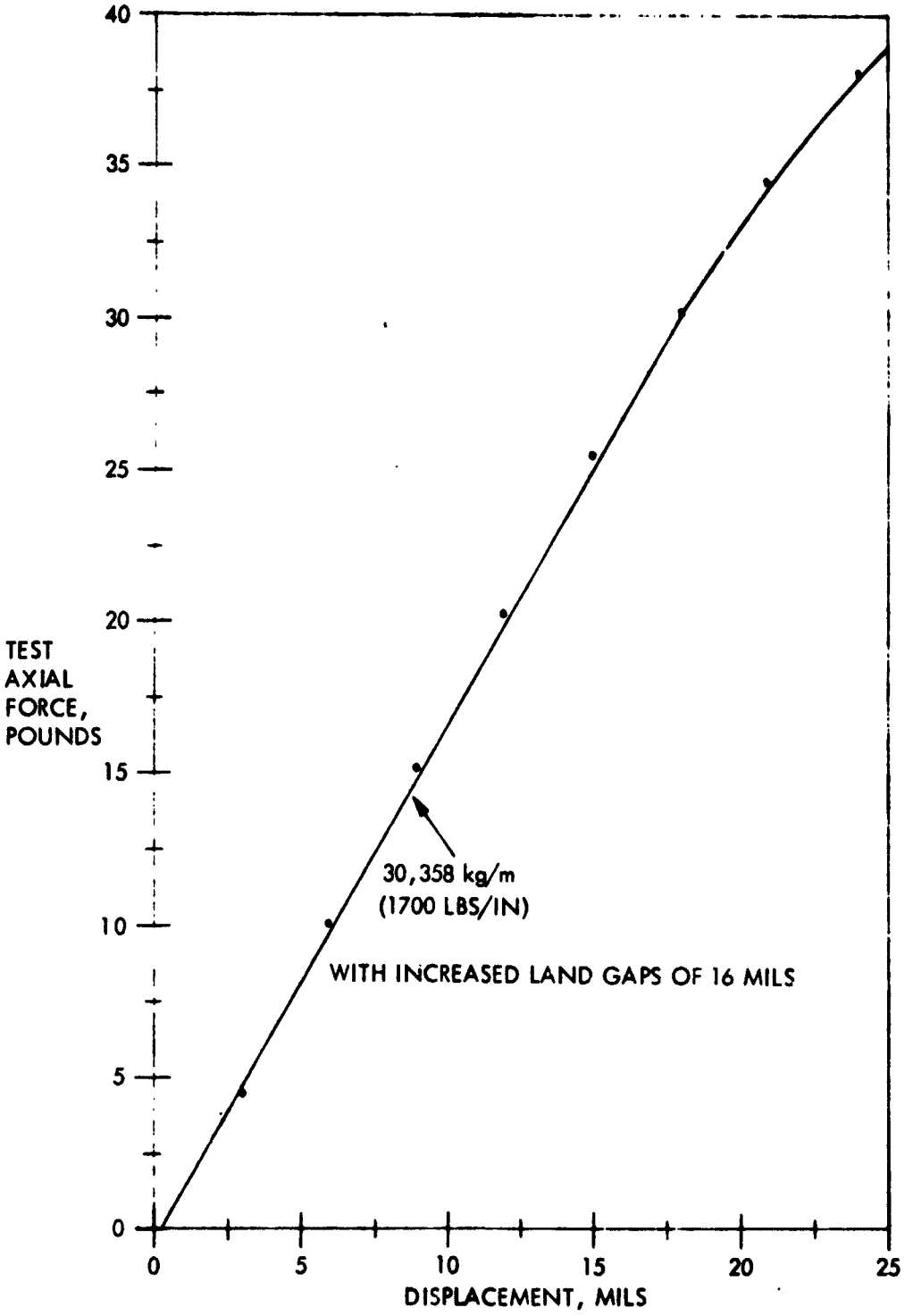

Figure 6-3. Magnetic Bearing Axial Displacement versus Axial Force

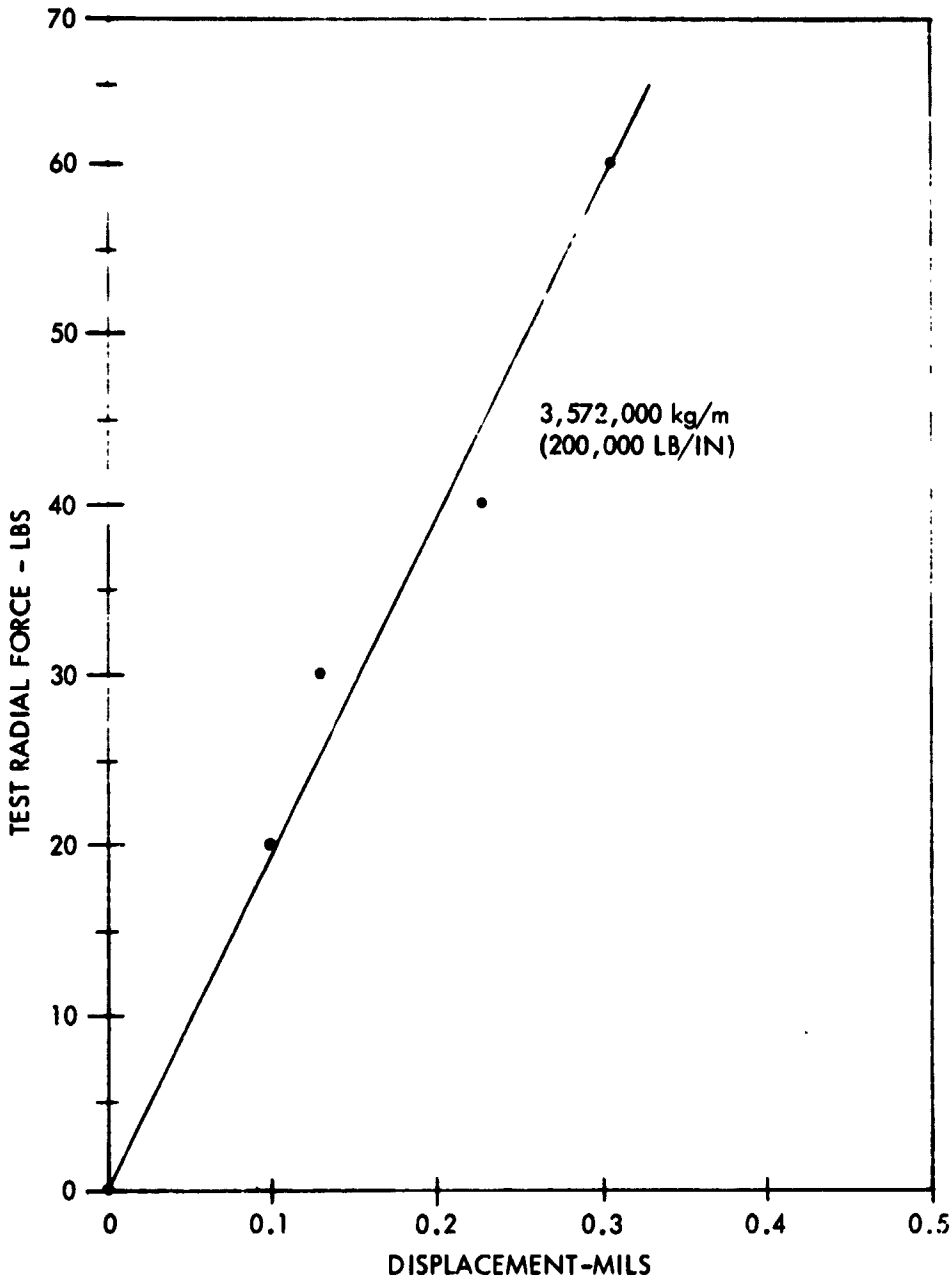

Figure 6-4. Magnetic Bearing (Pair) - Radial Stiffness

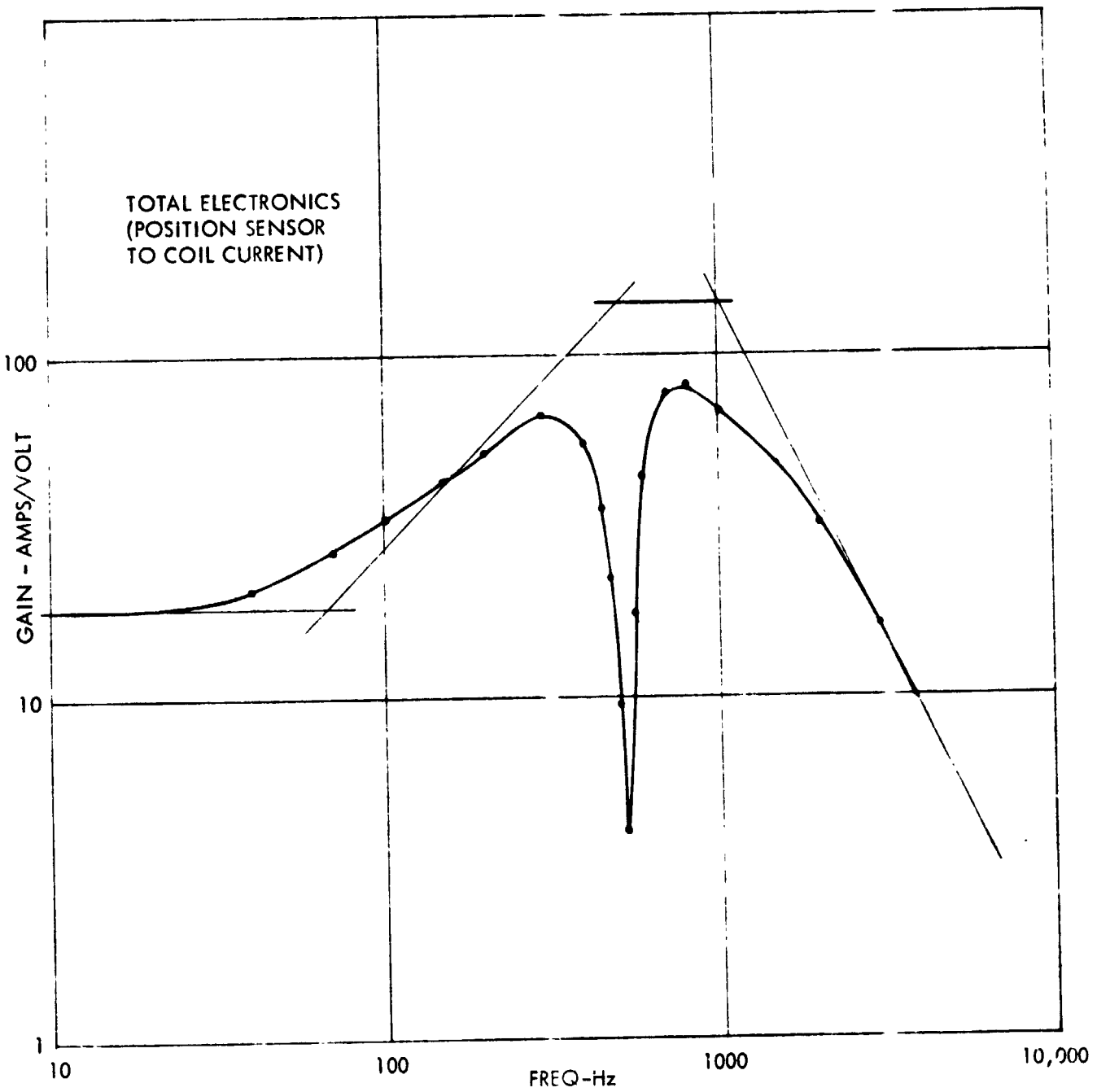

Figure 6-5. Electronics Frequency Response

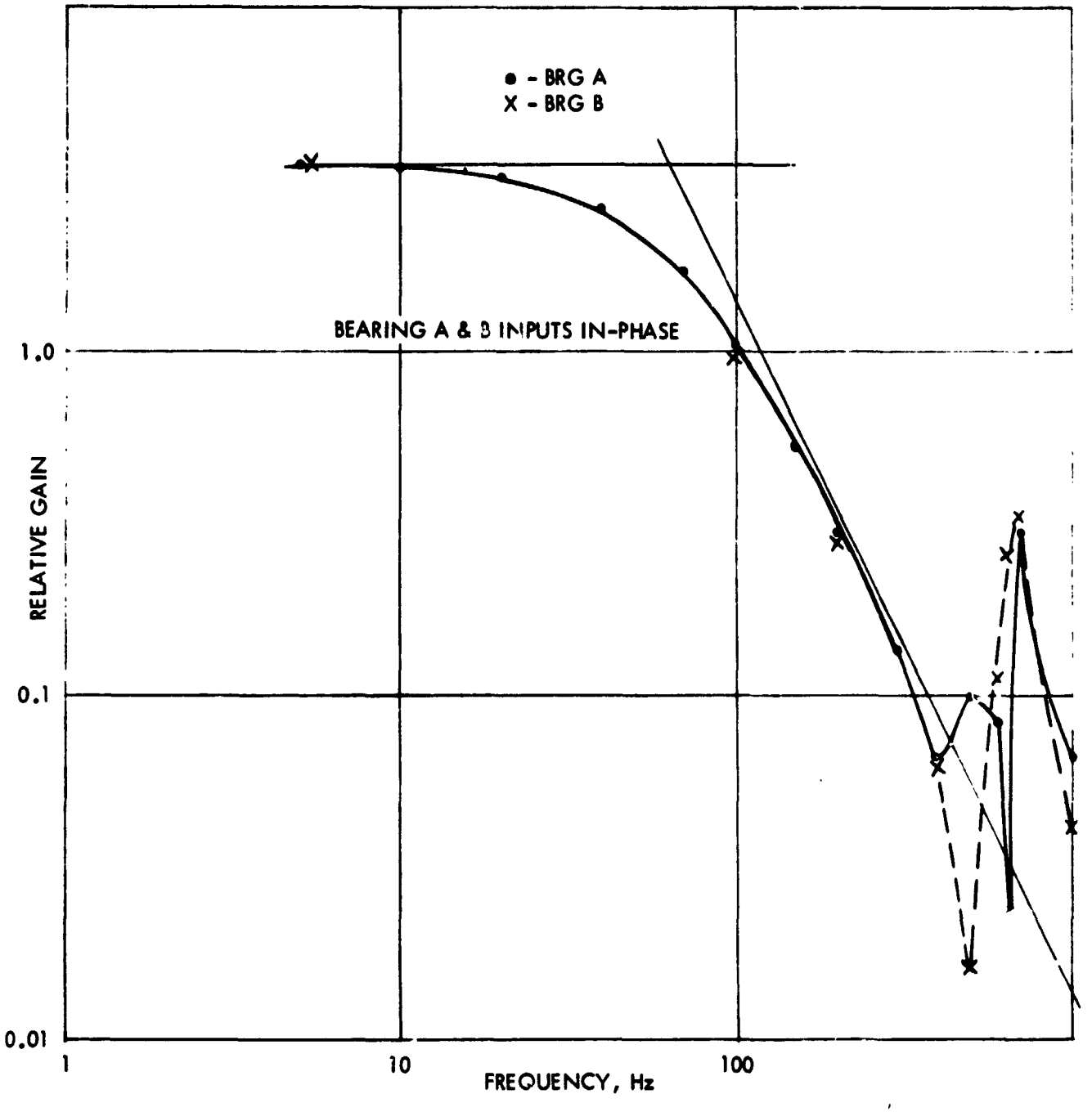

Figure 6-6. Closed Loop Frequency Response, Radial Translation

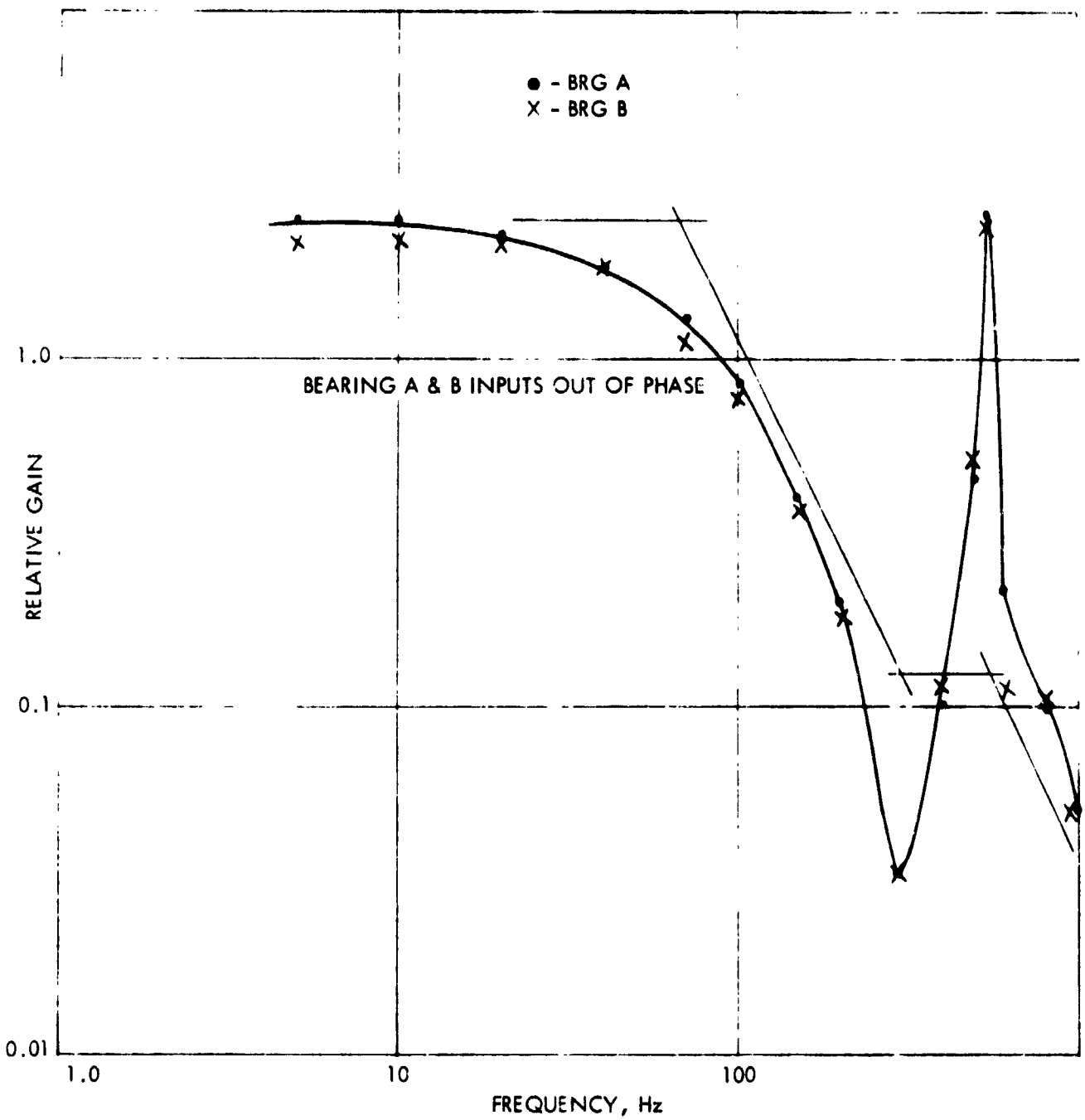

Figure 6-7. Closed Loop Frequency Response, Torsional

The closed loop responses, shown in Figures 6-5 and 6-7, were obtained by summing voltages with the magneto-resistor network voltage outputs in one axis for both bearings simultaneously. They indicate a bandwidth of approximately 408 rad/sec (65 Hz). In particular, the torsional response, Figure 6-7, where the bearings are driven out of phase, the structural resonance at ~3204 rad/sec (510 Hz) is clearly evident.

6.4 ENGINEERING MODEL SPIN-UP TESTS

The spin-up tests, conducted with the brushless dc spin motor with a maximum torque of approximately 0.0353 N-m (5 in-oz), determined the basic drag characteristic of the magnetic bearing, the effects of the type of back-up bearing used, and the limitations that determine the maximum operating speed of the rotor due to the magnetic bearings. Before the tests, the rotor/shaft were balanced to within 0.0051 mm (200 microinches) on ball bearings.

Figure 6-8 shows the low speed magnetic bearing drag data and indicates an almost constant drag torque of 0.000706 N-m (0.1 in-oz). This drag is due mainly to magnetic hysteresis in the motor and bearings. But analysis also indicates that if there was a difference between the center of the shaft rotating under the bearing poles and the center of mass of the entire rotating assembly that the bearing forces necessary to compensate for this could cause a torque of this magnitude. This premise is strengthened further by the fact that drag torque was measured at various speeds and found to be approximately the same (between 0.1 and 0.2 in-oz). Measurements made on the shaft, rotor, and magnets at this time indicated differences of up to 1.0 mil from location to location.

Initial high speed tests showed that a back-up ball bearing was needed to absorb the rotor energy instead of the original sleeve bearing. With the sleeve bearing initially used, the rotor/shaft would nutate violently upon impact and generate a considerable amount of heat in the sleeve.

With the ball bearing back-up bearing high speed testing reached a maximum speed of 523 rad/sec (5000 rpm) or 73.5% of the design speed of 712 rad/sec (6800 rpm) before contact was made with

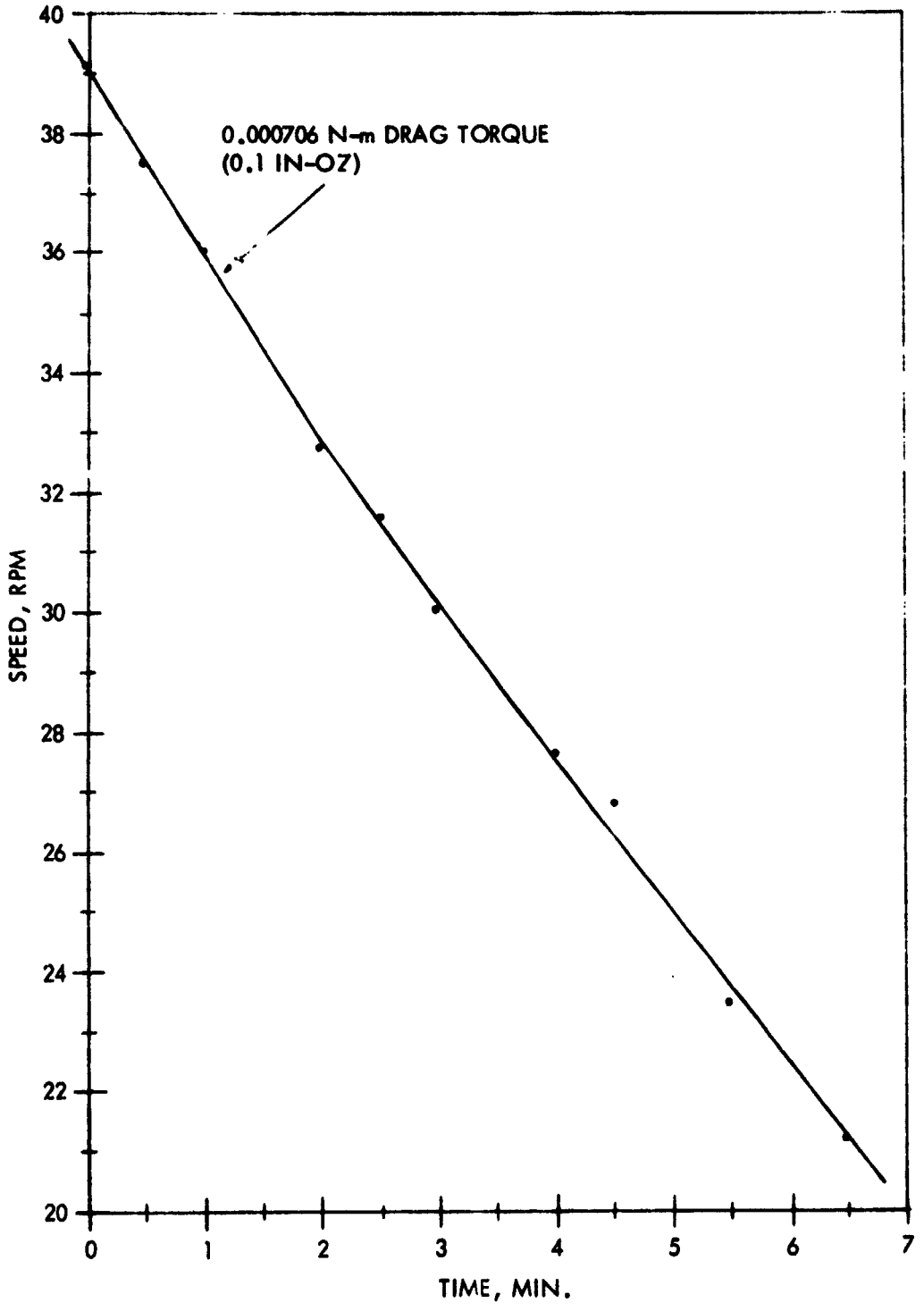

Figure 6-8. Low Speed Rotational Drag

the back-up bearing. The maximum momentum achieved was 74.57 N-m-s (55 ft-lb-sec). At this point, the rotor and shaft wobble was increasing due to the limited bandwidth of the bearing servos, as described in Section 4.3. The bandwidth limitation is due to the structural mode characteristics of the rotor and shaft of this particular design. These characteristics can be modified in future designs to permit higher servo bandwidth and thus higher spin speeds without excessive bearing displacements.

Section 7
REFERENCES

1. "Final Report, Electrostatic Gyro Evaluation Program", Volume II, Contract AF33(616)8350, General Electric Report No. 9500, February, 1964, SECRET

2. Boyajian, C.L., "Superconducting Bodybound Gyro-Development of an Experimental Model", General Electric Company, Final Report AFAL-TR-64-285, February, 1965, SECRET

3. McHugh, J.D., "Magnetic Bearings for Aerospace Applications", General Electric Company Report No. 63GL130, September, 1963

4. "Investigation of Magnetic and Electric Forces for Rotating Shaft Suspension", University of Virginia, Technical Documentary Report ASD-TDR-62-441, May 1962

5. Sixsmith, H., "Electromagnetic Bearing", the Rev. of Sci. Instr., Vol. 32, No. 11, November 1961, pp. 1196-1197

6. Auclair, G.F., "Advanced Reaction Wheel Controller for Spacecraft Attitude Control", AIAA Paper No. 69-855, August, 1969

7. Hertzendorf, B.H., and Manteuffel, E.W., "Final Report - Brushless DC Motor and Controller", Contract NAS8-25085, March, 1970 (ACD 9854)

8. Auclair, G.F., Manteuffel, E.W., and Rosenlieb, J.W., "Final Report - Brushless DC Motor for Momentum Exchange Attitude Control", Contract NAS8-20591 (A1), December 1967 (ACD 8765)

9. Auclair, G.F., Manteuffel, E.W., and Seminski, R.B., "Final Report - Brushless DC Torquer for Pendulous Integrating Gyro Accelerometer", Contract NAS8-20591, January, 1967 (LMEJ 8175)

APPENDIX A

COMPUTER PROGRAM
MAGNETIC BEARING - GAIN/PHASE

INPUTS	Figure 4-3 Name	Program Name
K_n/K_p mid band gain	K_n/K_p	G1
Notch Filter - frequency, R/S	ω_1	W1
- pole ζ	ζ_1	Z1
- Zero ζ	ζ_2	Z2
Integrator	ω_2	W2
Lead-Lag - lag	ω_4	W4
- lead	ω_5	W5
Power Amplifier - frequency, R S	ω'_7	W7
- ζ	ζ_7	Z7

OUTPUTS

Gain/Phase versus Frequency 1 - 100,000 R/S of:

K_n/K_p

$K_n/K_p - 1$

$\frac{K_n d}{K_n d'} - 1$

PRECEDING PAGE BLANK NOT FILMED

```
PAGE   1

// JOB     0004

LOG DRIVE    CART SPEC    CART AVAIL   PHY DRIVE
  0000         0004         0004         0000

V2 M10   ACTUAL  8K  CONFIG  8K

// FOR
*LIST SOURCE PROGRAM
*IOCS (CARD, TYPEWRITER, KEYBOARD, 1132 PRINTER, DISK, PLOTTER)
*ARITHMETIC TRACE
*TRANSFER TRACE
C       MAG BEARING - GAIN / PHASE
        DIMENSION W(6),GS(2),AA(2)
        DATA W /1., 1.5, 2., 3., 4.5, 7. /
   99 FORMAT (9F10.2)
   98 FORMAT (F10.1, F12.3, F10.2, F12.3, F10.2, F12.3, F10.2)
   97 FORMAT (////)
   96 FORMAT (1H1)
   95 FORMAT (F10.2)
        READ (2,99) G1, W1, Z1, Z2, W2, W4, W5, W7
        READ (2,99) Z7
        WRITE (3,96)
        WRITE (3,99) G1, W1, Z1, Z2, W2, W4, W5, W7, Z7
        WRITE (3,97)
   10 L=1
        DO 15 I=1,5
        C=10.**(I-1)
        DO 15 J=1,6
        WF=W(J)*C
        GO TO 40
   15 CONTINUE
   16 L=2
        WF=100000.
        GO TO 40
   19 CONTINUE
   20 L=3
        DO 25 K=1,5
        WF=W1*(.85+.05*K)
        GO TO 40
   25 CONTINUE
        PAUSE
   26 L=4
   27 READ (2,95) WF
        GO TO 40
   28 CONTINUE
        GO TO 27
C
   40 WF1=WF/W1
        WS=1.-WF1**2
        GN=SQRT((WS**2 + 4.*(Z2**2)*(WF1**2))/(WS**2 + 4.*(Z1**2)*(WF1**2)
      + ))
        AN=ATAN(2.*Z2*WF1/WS) -ATAN(2.*Z1*WF1/WS)
   50 GI=SQRT((W2/WF)**2 + 1.)
        AI=ATAN(WF/W2) - 1.57080
   60 WF4=WF/W4
```

```
      WF5=WF/W5
      GLL=SQRT((1. + WF4**2)/(1. + WF5**2))
      ALL=ATAN(WF4) - ATAN(WF5)
   70 WF7=WF/W7
      GP=1./SQRT((1. - WF7**2)**2 + 4.*(Z7**2)*(WF7**2))
      AP= -ATAN(2.*Z7*WF7/(1.-WF7**2))
      IF (WF7-1.) 75,75,74
   74 AP=AP-3.14159
   75 CONTINUE
   80 GT=GN*GI*GLL*GP*G1
      AT=AN+AI+ALL+AP
   82 DO 87 N=1,2
      GN=GT*(.615**(N-1))
      GG(N)=SQRT((GN*COS(AT)-1.)**2 + (GN*SIN(AT))**2)
      B=GN*SIN(AT)/(GN*COS(AT)-1.)
      AA(N)=ATAN(B)
      IF (GN*COS(AT) - 1.)  84,84,87
   84 IF (SIN(AT))  85,86,86
   85 AA(N)=AA(N) - 3.14159
      GO TO 87
   86 AA(N)=AA(N) + 3.14159
   87 CONTINUE
   90 D=57.2957
      AT=AT*D
      AA(1)=AA(1)*D
      AA(2)=AA(2)*D
   92 WRITE (3,93) WF, GT, AT, GG(1), AA(1), GG(2), AA(2)
      GO TO (15,19,25,28), L
      END

UNREFERENCED STATEMENTS
 10       16       20       26       50       60       70       80       82       90

FEATURES SUPPORTED
 TRANSFER TRACE
 ARITHMETIC TRACE
 IOCS

CORE REQUIREMENTS FOR
 COMMON       0  VARIABLES     102  PROGRAM     704

END OF COMPILATION

// XEQ
```

APPENDIX B

MECHANICAL ASSEMBLY AND ELECTRICAL SCHEMATIC DRAWINGS

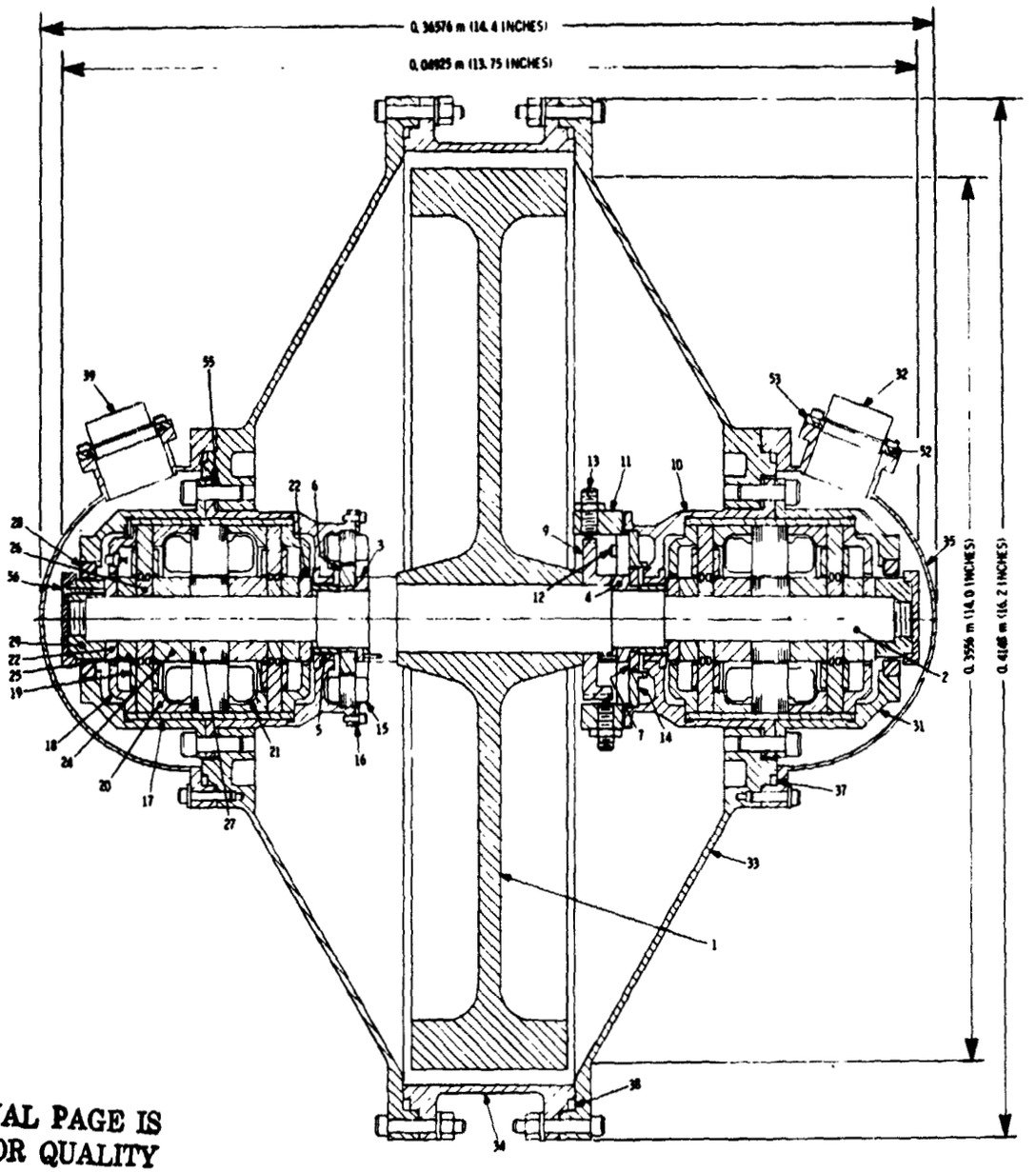

ORIGINAL PAGE IS
OF POOR QUALITY

1	WHEEL, MOMENTUM	22	POLE PIECE
2	SHAFT	24	MAGNET, PERMANENT
3	HUB	25	MAGNET, PERMANENT
4	HUB	26	CORE, THRUST BEARING
5	BEARING RACE	27	CORE, RADIAL BEARING
6	MAGNET, ROTOR	28	BALL BEARING
7	MAGNET, SENSING ROTOR	29	CLAMP RING
9	GEAR, PULSE GENERATOR	31	END CAP
10	HOUSING, BEARING	32	CONNECTOR
11	FRAME, SPEED SENSOR	33	BEARING SUPPORT
13	ELECTRO TECH SPEED DET.	34	CENTER FRAME
14	HALL ELEMENT ASSY	35	COVER
15	STATOR, MOTOR	37	"O" RING
16	CLAMP RING	38	"O" RING
17	SHELL	39	CONNECTOR
18	FRAME	52	O-RING
19	ASSY, THRUST BEARING	53	CONN. PLATE
20	SPACER RING	55	SHIM
21	STATOR RADIAL BEAR.	56	CAP

Figure B-1. Mechanical Assembly Drawing with Proposed Vacuum Enclosure

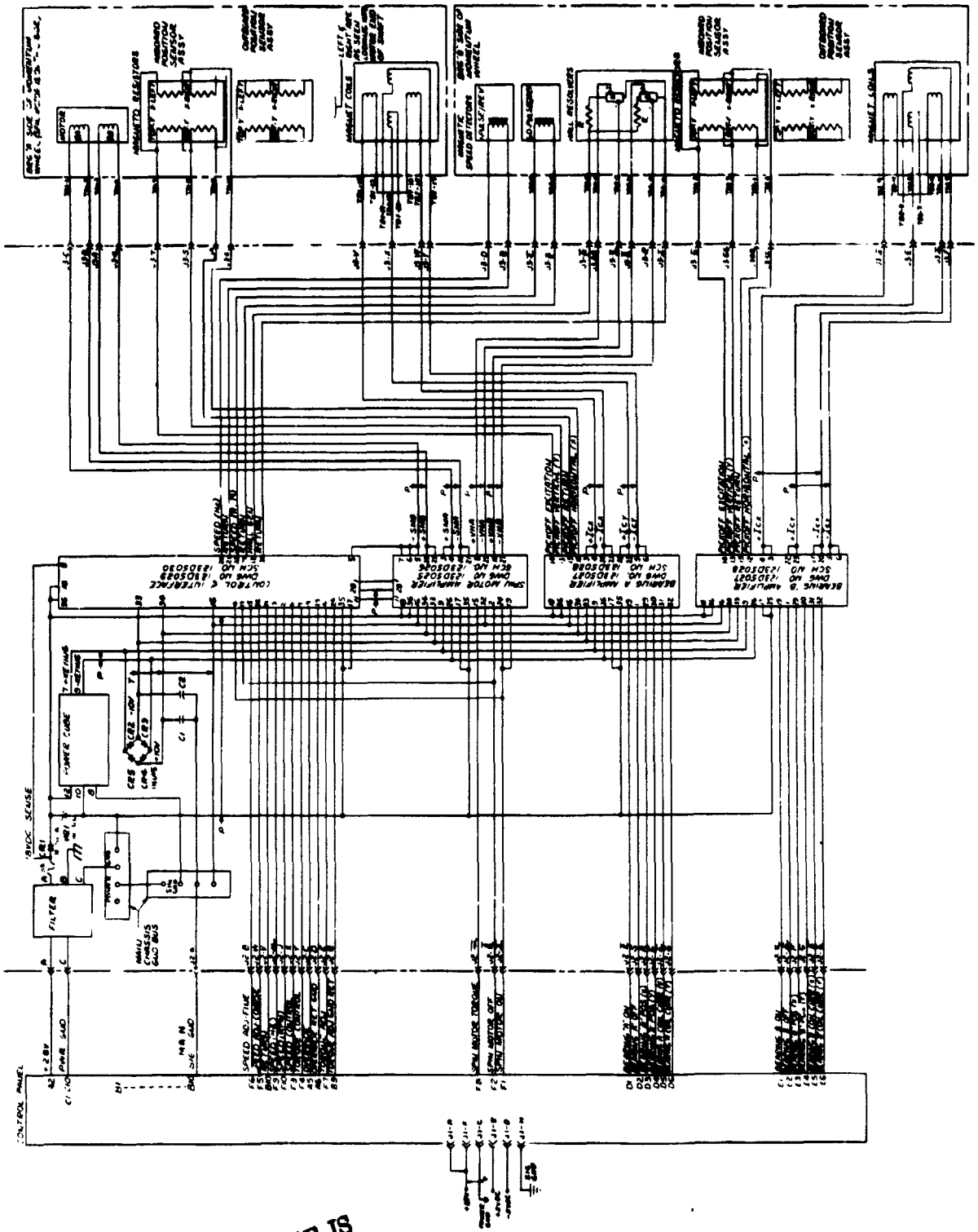

Figure B-2. System Electrical Schematic

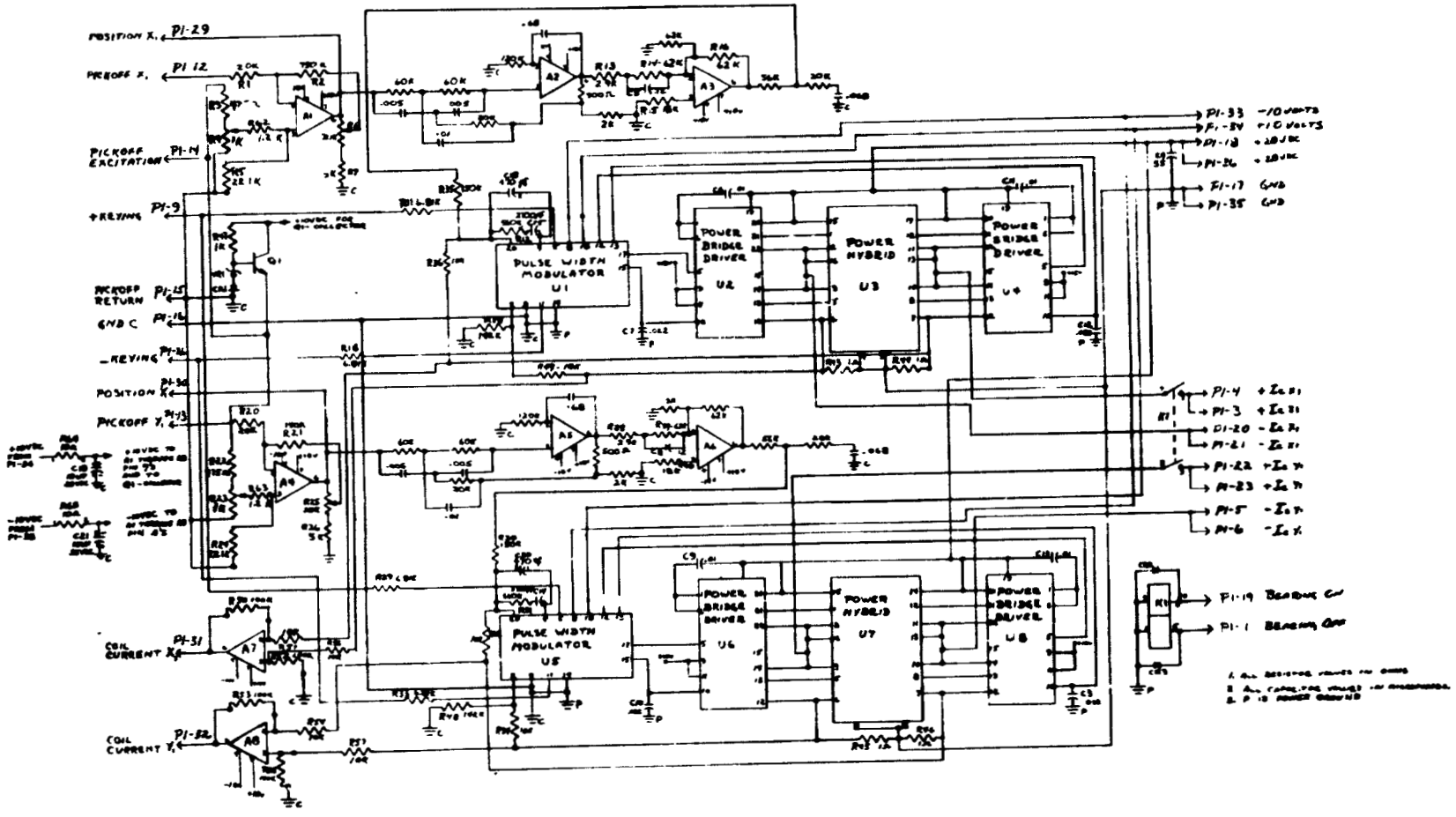

Figure B-3. Electrical Schematic - Bearing Amplifier

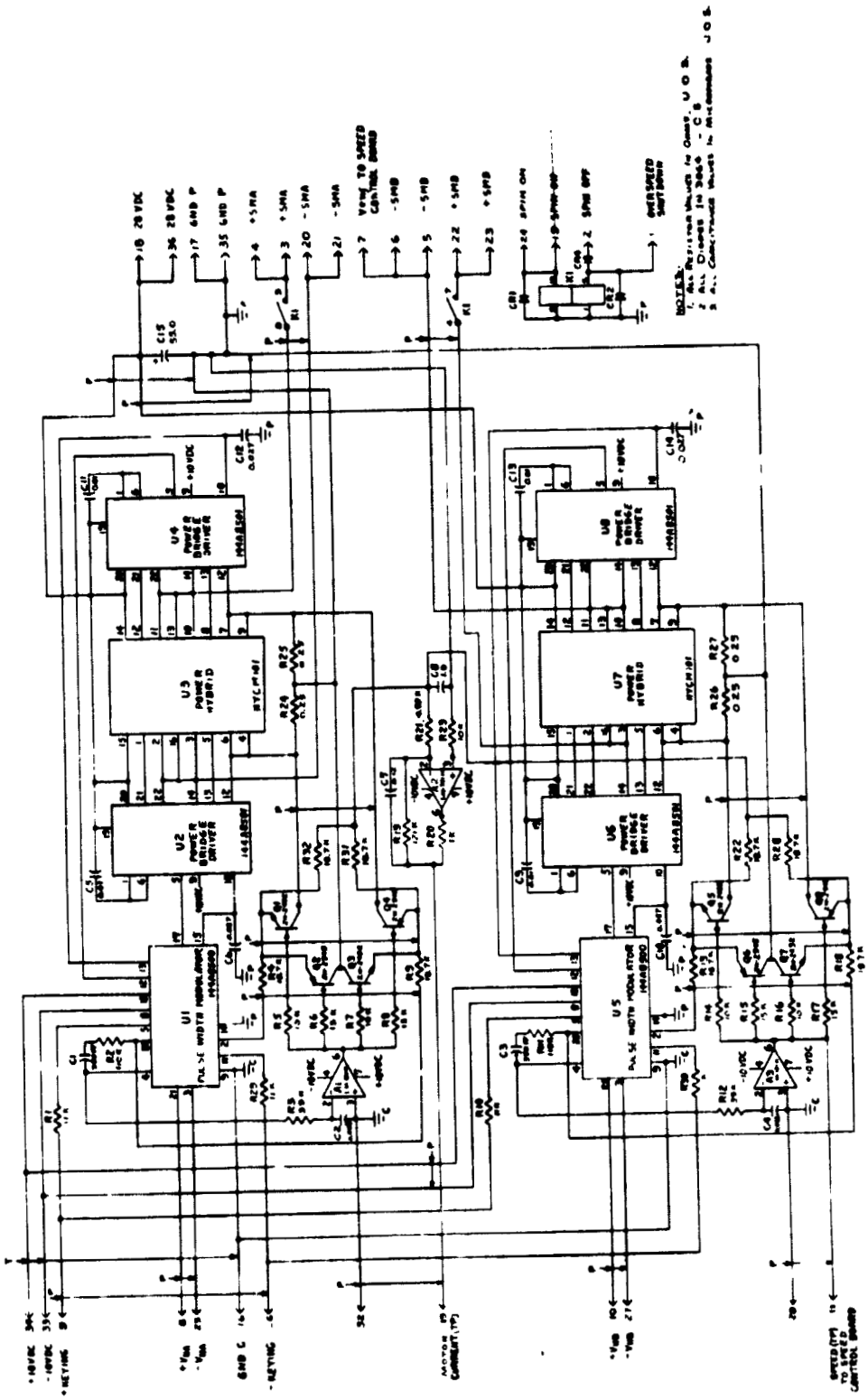

Figure B-4. Electrical Schematic - Spin Motor Amplifier

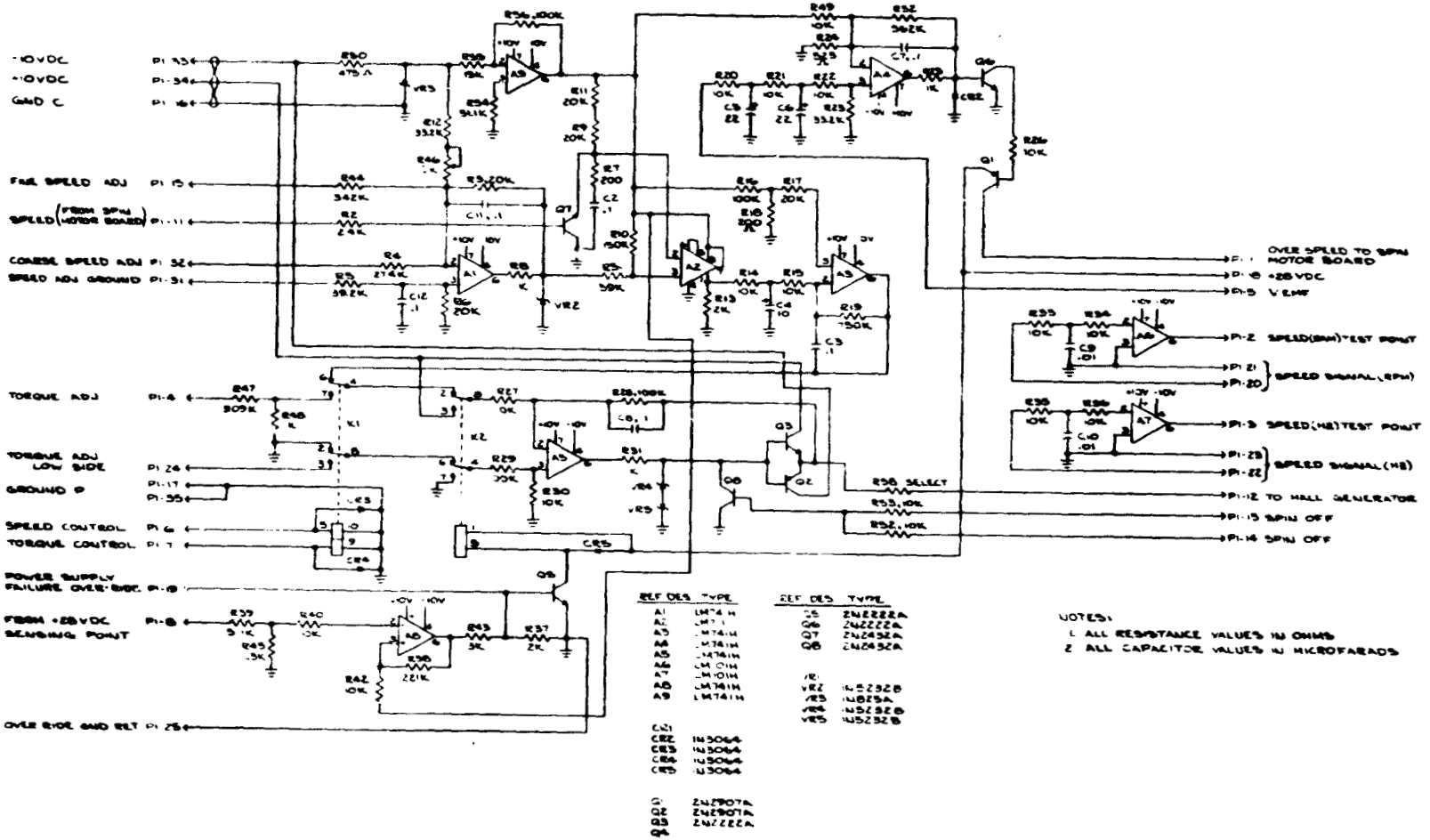

Figure B-5. Electrical Schematic - Control and Interface Board